ANALYSIS AND FABRICATION OF MEMS TUNABLE PIEZOELECTRIC RESONATORS

by

Amanda Allison Frederick

BS in Manufacturing Engineering, Miami University, 2004

BS in Mechanical Engineering, Miami University, 2004

Submitted to the Graduate Faculty of

School of Engineering in partial fulfillment

of the requirements for the degree of

Master of Science

University of Pittsburgh

2006

UNIVERSITY OF PITTSBURGH

SCHOOL OF ENGINEERING

This thesis was presented

by

Amanda Frederick

It was defended on

May 5, 2006

and approved by

Dr. Roy D. Marangoni, Associate Professor, Mechanical Engineering

Dr. Jeffery S. Vipperman, Associate Professor, Mechanical Engineering

Thesis Advisor: Dr. William W. Clark, Professor, Mechanical Engineering

ANALYSIS AND FABRICATION OF MEMS TUNABLE RESONATORS

Amanda Allison Frederick, M.S.

University of Pittsburgh, 2006

Piezoelectric MEMS resonators are being used with increased frequency for many applications, operating as frequency sources in sensors, actuators, clocks and filters. Compensation for the effects of manufacturing variation and a changeable environment, as well as a desire for frequency-hopping capabilities, have brought forth a need for post-process tuning of the resonant frequency of at these devices, in particular clocks and filters manufactured at the MEMS scale. This work applies a shunt capacitor tuning concept to three different types of piezoelectric MEMS resonators: bending beam devices, surface acoustic wave devices, and film bulk acoustic wave devices, in order to solve this tuning need across a wide range of the frequency spectrum (single Kilohertz to tens of Gigahertz). Questions about how the material and design parameters of these resonators affect the resonant frequencies and tunability of the devices are further discussed for each of the designs. In addition to the theoretical modeling, the fabrication steps necessary for processing the piezoelectric MEMS bending devices, specifically utilizing PZT thin films and an interdigitated design, are developed. Results of many fabrication trials are discussed, and finalized process plans for fabricating quality thin film PZT and PZT interdigitated devices are provided.

TABLE OF CONTENTS

LIST OF TABLES

LIST OF FIGURES

ACKNOWLEDGEMENTS

First and foremost, I would like to thank my advisor, Dr. William W. Clark. I could not have asked for an advisor who would be more helpful, understanding, and enjoyable to work with throughout my career as a master's student at University of Pittsburgh.

Secondly, I would like to thank Dr. Sandy Hu, who has given me much guidance on the MEMS fabrication necessary for this project, and done so with a great deal of patience and valuable insight. Additionally, I wish to recognize Dr. Jeffery S. Vipperman and Dr. Roy D. Marangoni who have aided me through their contributions as members of my thesis defense committee.

Next, I must acknowledge all of the help I received from collaborators at other Universities. Specifically, this would include Wonjae Choi, Robert Xie, and Dr. Sang-Gook Kim at the Massachusetts Institute of Technology, who helped me bring back the technology and understanding of PZT sol-gel fabrication to the University of Pittsburgh, in addition to providing continued help and feedback throughout the course of my research. Many other students and faculty at University of Pittsburgh, Carnegie Mellon University, and Penn State University also deserve credit for their roles in training me on equipment, allowing me use of their faculties, or teaching me the fundamentals behind their relevant processing specialties.

In addition, I must recognize the National Science Foundation for their financial support contributed to this work through grant CMSO324456. Without this funding, much of the processing materials needed for this project could not have been purchased.

Finally, but in no way the least important, I must thank my friends and family. The other students in the Vibration and Controls laboratory have made it a wonderful environment to work in these past two years. My roommate, Kathryn, has been a constant source of support from the first day I moved to Pittsburgh, and the friends I have made here in Pittsburgh have truly made it a fantastic place to study.

1.0 INTRODUCTION

From everyday appliances such as clocks, toasters, cell phones, and toys, to the most advanced government and military applications, such as radar, navigation, missile guidance and Identify Friend or Foe (IFF) systems, frequency sources are a key component of much of today's electronics. Frequency sources are used as sensors, clocks and filters, and the ability to control the accuracy and stability of these devices is vital to their performance characteristics and ability to bring forth advancements in technology.

Many specific needs exist for today's most capable frequency sources. Cost effectiveness, customer demand, and the electronics industry's desire for compatibility with current microelectronics, specifically complementary metal oxide semiconductor (CMOS), process techniques has enhanced the need for miniaturization and promoted research in the area of microelectromechanical resonators. Correspondingly, effort has been made to develop resonators made using the easiest, most-repeatable Micro-Electro-Mechanical-Systems (MEMS) processing with the least power expenditure. Good temperature stability, high quality factors and ability to cover a large frequency range are additional needs for resonator technology. Since smaller size inherently leads to faster speed, lower power consumption, higher complexity, and lower cost in both the electrical and mechanical domains (Nguyen, 2004), frequency source research has been naturally driven towards MEMS technology to fit the device's characteristic needs.

Many of the most common resonating devices use quartz resonators, and while these do offer high stiffness (high quality factor), a wide range of frequencies, and good stability with respect to aging and temperature variations, they are not compatible with micromachining processing and face issues with low power-handling ability (Park, 2003). Similarly, while many designs for silicon-based, electrostatically-driven MEMS resonators are CMOS compatible (Jeon, 2003 and Tang, 1990) and have high quality factors, they are limited in the frequency range of operation and have a high degree of variability in their fabrication processes. This work utilizes MEMS piezoelectric resonators, which offer a much wider frequency range and variety of structural modes available, as well as the potential for no steady-state power consumption, elimination of some difficult processing requirements and electronic processing compatibility.

Even in well-controlled microprocesses, structural deviations in devices occur both from wafer to wafer and across a single wafer's surface. For example, resonant frequencies of MEMS comb-drive resonators can vary by a few percentages across the same chip (Tang, 1989). Material imperfections and variations in processing (deposition, etching, etc.) can all lead to irregularities between devices. Consequently, although structures are designed to resonate at a particular frequency, or within a particular frequency range, often these desired results are not achieved and some sort of post-process tuning must be applied in order to attain the desired frequency response.

In addition, even if the manufactured resonator does oscillate at the frequency for which it was designed, changes can occur due to aging, thermal mismatch, contamination or other environmental conditions which alter the device's frequency over time (Adams, 1997). Similarly, if the temperature coefficient of frequency for the materials is large, then the frequency of the device can vary greatly over a range of operating temperatures (Yu, 2004). In these situations, it is desirable to have active tuning capability to change the properties of the resonator in real-time for frequency controlling purposes.

Finally, many high-security and communications systems require frequency sources that can rapidly, accurately switch between frequencies for purposes such as jamming resistance and hiding signals. One example of a multi-frequency application is the communications protocol 'Frequency Division Multiple Access (FDMA)' which makes use of eighty different frequencies spaced over a band of 80 kHz (with a nominal frequency of 2.4 GHz) for purposes of transmitting data. Increasing the number of frequencies used would allow for a greater variety of types and an increased amount of data to be transmitted; however, improvements in frequency resolution and switching ability are needed to make this advancement realistic.

Key technology users, such as the Department of Defense, have specifically recognized the severity of these needs, organizing special review into investigations of frequency control devices. They have stated that "frequency control device technology is of vital importance to the DOD since the accuracy and stability of frequency sources and clocks are key determinants of the performance, radar, C3I, navigation, surveillance, EW, missile guidance, and IFF systems." (Department of Defense, 1996).

All of these factors show the need for post-processing tunability of a resonator's natural frequency, ideally through a design with maximum versatility that puts limited additional requirements on the manufacturing and operation of the device. This work fills that need through the application of a shunt capacitor tuning concept, where the resonant frequency of the device has a maximum value (the open-circuit frequency), a minimum value (the short-circuit frequency) and can be varied between these two by inserting shunt capacitors in parallel with the piezoelectric element. The concept is applied to a variety of theoretical models for different types of piezoelectric resonators (bending devices, surface acoustic wave resonators, and film bulk acoustic resonators) whose resonant frequencies span over a wide operating range. The results that certain resonator design properties have on the overall tunability of the devices are investigated as well.

Finally, the main steps necessary for fabrication of these resonators, in particular the bending beam with interdigitated electrodes, are developed. The results of property testing and visual inspection are discussed throughout the iterations of the updated process plans. To conclude, finalized process plans are given for the interdigitated devices, and future work for the poling and testing of these resonators is suggested.

2.0 RESONATORS: LITERATURE REVIEW

2.1 RESONATOR TUNING

Generally, MEMS resonator tuning techniques can be classified into two major categories: those which tune the resonators frequency passively, making one-time, permanent changes in the device, and those which offer active tuning capabilities. To date, several techniques have been investigated for both major categories of tuning, each of which offer their own benefits and disadvantages.

2.1.1 Passive Tuning Techniques

For permanent-change tuning of a devices' frequency, techniques using selective removal of portions of the resonator have been shown to make significant changes in the resonant frequency of a structure. For macro-scale devices, this can be done using such techniques as sandblasting, drilling or grinding (Johnson, 1983). For the most accurate results, a feedback loop would be utilized, whereby the difference between the desired frequency and the actual frequency is measured, and decreasing amounts of material are eliminated from the device. Different tolerances are associated with each of the processes, as displayed in Table 1. The frequency adjustment tolerances are given from ten times the value shown, so, for example, if a resonator is measured to be 8000 parts per million away from the final resonance frequency, it can be ground on its major frequency control surface to a value within 800 parts per million of the frequency design goal.

Table 1. Frequency Adjustment Tolerances for Various Machining Processes

Process	Tolerances without Feedback (Noniterative) (ppm)	Tolerances with Feedback (ppm)
Grinding a major surface	+/-800	-
Grinding a minor surface	+/-400	-
Edge grinding	+/-250	+/-100
Sandblasting	+/-150	+/-75
Drilling	+/-100	+/-40
Laser trimming	-	+/-20

It can be seen that processes such as drilling or laser trimming produce more accurate results; however, these processes are also more time consuming, increasingly costly and can cause large distortions in the device being processed.

Laser trimming (Harvey, 1997) and reactive ion etching (RIE) (Lakdawala, 1998) have both been used as post-processing resonator tuning techniques in MEMS applications. In Lakdawala et al, RIE was shown to be able to change a Film Bulk Acoustic Resonator's (FBAR) resonant frequency by as much as 10%, with abilities to match a frequency within 0.01% of the desired value. Unfortunately, laser trimming is not effective for very small structures (<10 um wide) (Joachim, 2003) and reactive ion etching techniques face problems with decreased quality factors (Lakdawala, 1998). Alternatively, procedures have been described where material is added to the device, such as in Joachim's work of selective deposition of polysilicon (Joachim, 2003). Here, the effective mass and stiffness of the system are both increased, thereby altering the frequency and, theoretically, improving the quality factor simultaneously. Joachim's work showed an increase of 1.96% from an initial 86.6 kHz frequency.

Localized annealing presents yet another possible means of passive frequency tuning for MEMS resonators (Joachim, 2003 and Wang, 1997). In this application, voltage pulses are sent across the resonator from anchor to anchor, generating a corresponding current flowing through the resonator and producing heat, effectively annealing the associated area (Wang, 1997). This treatment has the result of altering the residual stresses in the resonator, thereby changing its resonant frequency. In addition, the length of the associated "hot spot" can be altered to vary the amount of tuning. It is important to note, however, that stringent limits exist on the pulse durations that can be applied at different annealing voltages before damage is done to the device. In Wang et. al's work, the pulse duration was required to be shorter than 3ms at an 8 volt annealing voltage to avoid destroying the device.

For resonators manufactured on substrates with a large temperature coefficients of frequency (TCF), success has been shown in integrating additional layers with opposing TCFs (Dewan, 2005, Pang, 2005 and Yu 2005) in order to eliminate the effects of temperature dependence. Silicon Dioxide, Aluminum Nitride, and Tellurium Dioxide all have negative TCFs and have been incorporated as frequency tuning layers in resonating devices with positive TCF substrates. In Yu et. al's work (Yu, 2005), TCFs of less than 1 ppm/degree C were achieved by incorporating a layer of silicon dioxide onto a zinc oxide film bulk acoustic resonator.

In piezoelectric resonators, it has been recognized that depolarization can provide a passive approach for adjusting the resonant frequency of the structure by means of altering the coupling coefficient of the piezoelectric (Johnson, 1983 and Kielczynski, 1989). The theory behind this technique is similar to that used in this paper in that the contribution from the electrical stiffness of the device is eliminated from the overall rigidity, thereby altering the device's natural frequency. However, the depolarization accounted for in the prior works results in a one-time change in the frequency of the device, whereas the technique utilized in this paper is an active approach used in adjusting the stiffness associated with the piezoelectric. In addition, further processing concerns are often present with the depolarization processes used to make property changes in the passive tuning approach.

2.1.2 Active Tuning Techniques

Although many of the previously mentioned techniques have proven successful in certain niche applications, an active tuning approach could be much more widely used across the spectrum of tuning needs, particularly for requirements like frequency hopping. These active-tuning approaches are also superior in that the changes made to the resonators in order to accomplish tuning are non-permanent: consequently, they are much more versatile for functions such as counteracting the effects of aging and environmental variation. Again, several techniques have been investigated by previous researchers: principle among these methods are approaches which use electrostatic stiffness adjustments, changes in internal stresses, and modification in the moduli of the resonating material (Adams, 1998, Lee, 2004, Remtema, 2001 and Ruby, 1994).

In electrostatic-actuating devices, tuning capability is often built into the designs of parallel-plate or comb-drive resonators. In Adams et. al's work (Adams, 1998), by increasing the voltage across a parallel-plate actuator, the effective stiffness of the resonator is altered so as to reduce the resonant frequency of the structure. Values of up to 70.3% reduction were demonstrated for such devices. Similarly, in Lee et. al's work (Lee, 2004), a resonator is designed so that the AC and DC voltages are used to actuate the comb-drive microactuator, and a separate control voltage is used to tune the frequency of the device. For Lee's design, the frequency response of the microactuator varies from 19.0 kHz to 8.45 kHz, or 55% reduction, as the control voltage is varied between 0 and 150V (Lee, 04). Unfortunately, the introduction of parasitic capacitance is associated with electronic tuning (Joachim, 2003), extremely small gaps sizes are necessary for transduction and fundamental limits exist before instability at the "pull-in" voltage occurs for electrostatic-actuating devices.

The tuning method developed by Remtema and Lin (Remtema, 2001) combines the advantages of thermally induced stress effects and temperature dependence of the modulus of elasticity to tune the resonant frequency. Compressive stresses, which can be generated in a resonator by localized heating, cause the structure to become more compliant: similarly, as a device heats up, the young's modulus of the material decreases. Consequently, by resistively heating a device, the benefits of these two phenomena can be combined to multiply the affect of lowering the stiffness, and in turn, the resonance of the device. In Remtema and Lin's work, devices were shown to be capable of up to 6.5% frequency adjustment with minimal power requirements. A similar approach was used by Ruby and Merchant (Ruby, 1994), in which microheaters were embedded into FBARS for frequency tuning and temperature stabilization purposes. Good results were shown, generating frequency shifts of 50-80 ppm per degree C at different material thicknesses. The drawback is that although the frequency shifts achieved in these works are substantial, a relatively large electrical power is needed to drive the heating necessary to make a substantial change in the resonators properties. Repeatability in the frequency control using this heating technique has been shown to be an issue as well (Pang, 2005).

In conclusion, it can be seen that although many different tuning techniques have been researched for use in resonator applications, none are without their drawbacks and additional techniques which overcome these limitations would clearly offer strong benefits to the MEMS resonator market. Furthermore, conclusions about the needs of an effective microelectromechancal resonator can be reiterated, including that the ideal tuning technique would use an active approach, require no power in a hold state, have a wide range of available tuning and be highly repeatable across trials.

2.2 RESONATORS: CLASSIFIED BY ACTUATION

A simple definition of a resonator is a device with a vibratory natural response (Senturia, 2001). Generally, MEMS resonators are classified by their type of oscillation actuation, the most common of which are electrostatic, magnetostatic, piezoelectric and thermal expansion (Ristic, 1994).

2.2.1 Electrostatic

The largest amount of research conducted in the area of MEMS resonators has been towards the development of electrostically-driven devices. Most commonly, electrostatic actuation is used on comb-driven resonant structures, or parallel plate devices, which make use of reverse-polarity capacitance. Works by Xie and Fedder (Xie, 2004), Selvakumar et. al (1995), Tang et. al (Tang, 1994), and Lee et. al (Lee, 2004 and Lee, 1996) all use electrostatic-comb drives to propel movement in resonant devices. In these devices, the electrostatic force is generated by the comb-drive voltage, which is a function of the DC bias voltage, the AC drive voltage, and other material properties of the beam. Beam structures are designed to supply coupling between input and output electrodes, and the resonant frequency of the structure is a function of design parameters such as the suspension structure, number of combs, spacing of the fingers, etc. Recently, new designs such as the wine-glass mode ring resonator by Xie (Xie, 2003) have been made to take advantage of higher modes of oscillation. Xie's design combines the extensional radial contour vibration mode with the wine-glass disk vibration mode to achieve frequencies as high as 1.2 GHz. Excitation is achieved by applying a DC-bias voltage to the conductive ring and an AC drive voltage to select electrodes to generate the necessary electrostatic force.

Although many electrostatically-driven MEMS resonators can be easily integrated into CMOS processing and are often capable of generating high Q values, their frequency ranges are more limited and there is a good deal of variability in the fabrication. Post-process tuning for varying their resonant frequency is often necessary, but can be difficult to perform. Consequently, the need for additional types of resonators remains.

2.2.2 Magnetostatic

Magnetostatic actuation has also been used in MEMS resonators. In design, magnetostatic wave (MSW) resonators are structurally similar to surface acoustic wave (SAW) devices, using parallel finger electrodes placed between reflecting edges for exciting wave propagation. Magnetostatic surface waves (MSSW), magnetostatic forward volume waves (MSFVW) and magnetostatic backward volume waves (MSBVW) can all be produced depending on the direction which the bias magnetic filed is applied with respect to the traveling wave (Kinoshita, 1990). Generally these devices operate in the GHz frequency range, and they are particularly applicable to tuning applications. Devices fabricated by Ishak et. al (Ishak, 1988) and Kinoshita et. al. (Kinoshita, 1990) are two examples of magnetostatic wave resonators.

2.2.3 Thermal Expansion

Some work in designing resonators has been done using thermally-actuated cantilever beams, where resistive heating is used to generate movement by means of thermal expansion (Kolesar, 1999). In Kolesar et. al.'s thermal resonator, the applied voltage produces a current which is passed through the device from anchor to anchor, generating a current density variation between the two arms of the resonator. As the heat causes one arm to heat and expand more than the other, the beams (which are joined at their released ends) are arced upward until the current is removed, at which point they return to the equilibrium position. In the thermally-excited beam resonator designed by Moser et. al. (Moser, 1991) heating power is generated by a harmonic voltage superimposed on a D.C. voltage applied across the device. By sandwiching device layers with different thermal expansion coefficients, dynamic heating causes resonance in the structure.

2.2.4 Piezoelectric

The most widely used class of materials in resonator fabrication are crystals; most specifically, quartz. When used as resonators, crystals are excited into vibration of their modes by means of electromechanical coupling using the piezoelectric effect. Quartz has been widely used for its beneficial properties of high stiffness (high quality value) and excellent stability in withstanding temperature and aging variation. The largest downside of quartz is that it is not compatible with current CMOS micromachining, and consequently cannot be used in many MEMS resonator applications.

Other piezoelectric materials, namely piezoceramics, are finding many applications in the MEMS field. Devices by Beeby and White (Beeby, 2000), Lee and White (Lee, 1995) and Soderkvist and Hjort (Soderkvist, 1994) are just three examples of the many MEMS piezoelectric resonating devices that have been researched. Lead Zirconate Titanate (PZT), Zinc Oxide (ZnO), and Gallium Arsenide (GaAs) were the piezoelectric materials used in these studies, respectively. Processing considerations, resonator characteristics, and electromechanical coupling all have a significant impact on material choice for resonator applications.

Piezoelectric resonators are usually classified according to their mode of vibration. They offer a wide range of modes that cover a vast frequency range from single kilohertz to tens of gigahertz. A chart describing the typical frequency ranges associated with different piezoelectric vibration modes is given in Figure 1. Devices have been fabricated by various researchers in all of these modes of oscillation from bending cantilever beams and resonating plates (Lee, 1995) to surface acoustic wave (Ippolito, 2003) and bulk acoustic wave devices (Su, 2001).

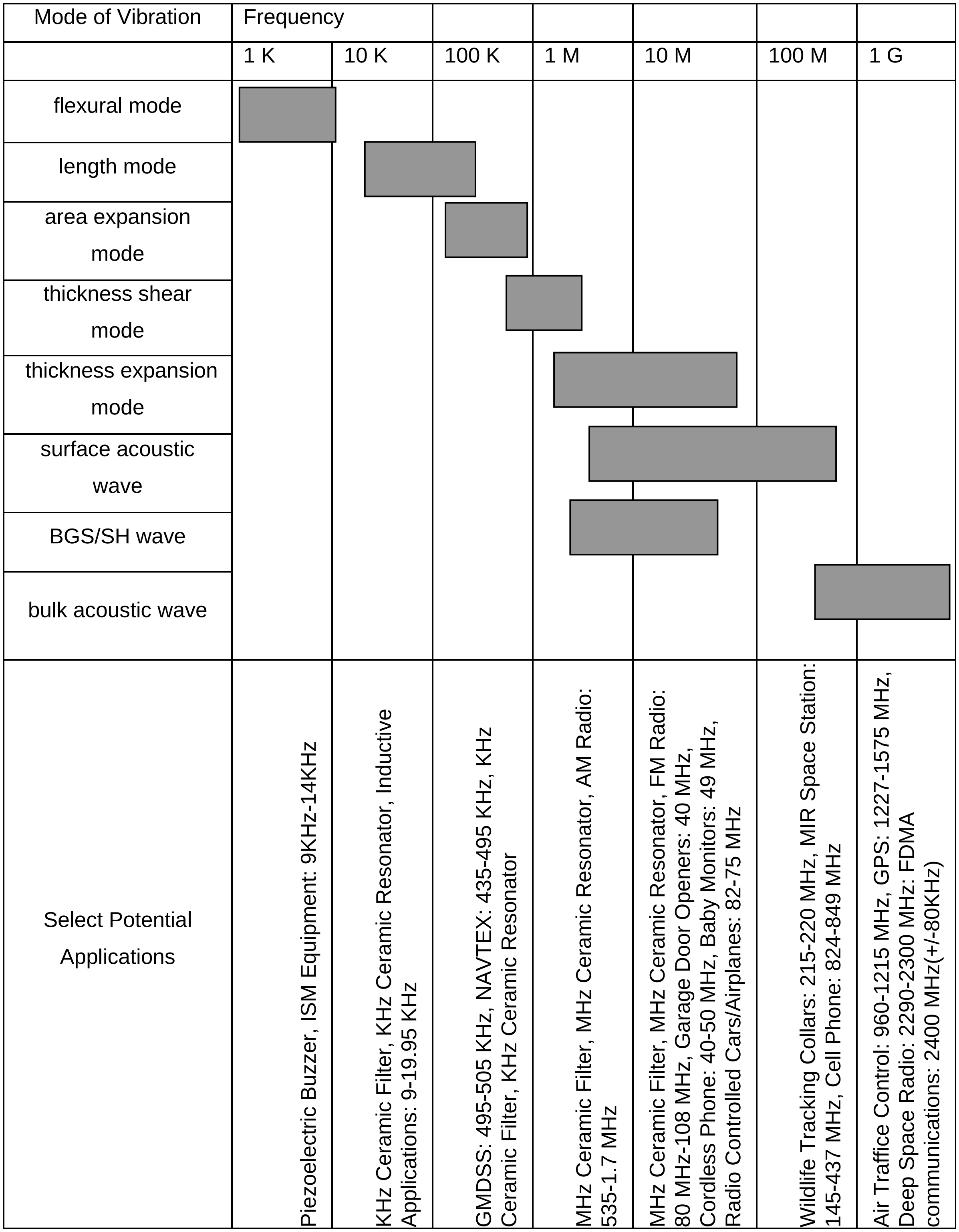

Mode of Vibration	Frequency					
	1 K	10 K	100 K	1 M	10 M	100 M	1 G
flexural mode	▨						
length mode		▨	▨				
area expansion mode			▨				
thickness shear mode			▨	▨			
thickness expansion mode				▨	▨		
surface acoustic wave				▨	▨	▨	
BGS/SH wave				▨	▨		
bulk acoustic wave						▨	▨
Select Potential Applications	Piezoelectric Buzzer, ISM Equipment: 9KHz-14KHz	KHz Ceramic Filter, KHz Ceramic Resonator, Inductive Applications: 9-19.95 KHz	GMDSS: 495-505 KHz, NAVTEX: 435-495 KHz, KHz Ceramic Filter, KHz Ceramic Resonator	MHz Ceramic Filter, MHz Ceramic Resonator, AM Radio: 535-1.7 MHz	MHz Ceramic Filter, MHz Ceramic Resonator, FM Radio: 80 MHz-108 MHz, Garage Door Openers: 40 MHz, Cordless Phone: 40-50 MHz, Baby Monitors: 49 MHz, Radio Controlled Cars/Airplanes: 82-75 MHz	Wildlife Tracking Collars: 215-220 MHz, MIR Space Station: 145-437 MHz, Cell Phone: 824-849 MHz	Air Traffice Control: 960-1215 MHz, GPS: 1227-1575 MHz, Deep Space Radio: 2290-2300 MHz: FDMA communications: 2400 MHz(+/-80KHz)

Figure 1. Piezoelectric Resonator Modes, Associated Frequencies and Applications

(Compiled from Murata Manufacturing Co, 2006, Marshall, 2006, ERO Frequency Information Source, 2006 and Yu, 2005)

In this work, special attention is paid to flexural bending mode, surface acoustic wave, and bulk acoustic wave devices for application of the resonator tuning concept. The following section describes devices oscillating in each of these modes in greater detail. As can be seen in the charts, by applying the concept to these three modes of resonance, nearly the entire frequency spectrum from single kilohertz to tens of gigahertz is accounted for.

2.3 PIEZOELECTRIC RESONATORS: CLASSIFIED BY MODE

2.3.1 Bending Mode

Flexural vibration, or bending mode vibration, occurs in the lower frequency range for resonators (KHz). In a two-layer structure, a simplified version of that used in this work (substrate layer, piezoelectric layer), curvature is produced in the beam when one layer expands and the other layer contracts; for a piezoelectric unimorph, this occurs when the applied voltage creates a strain in the piezoelectric material. An example of a piezoelectric cantilever beam undergoing bending vibration is shown in Figure 2.

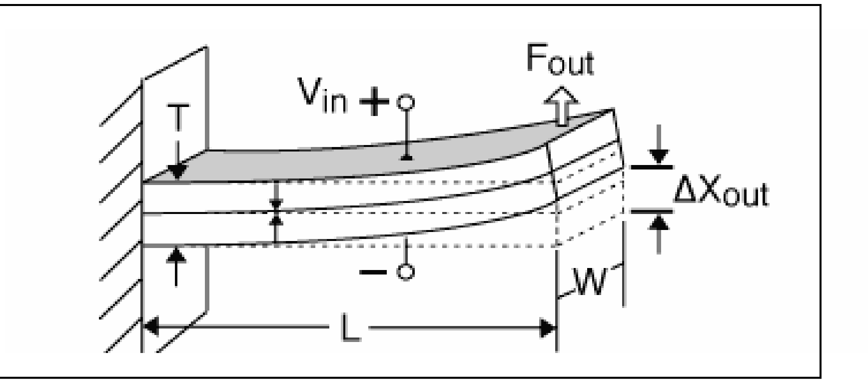

Figure 2. Cantilever Beam Undergoing Bending Vibration

It is widely known that the fundamental natural frequency of vibration for a beam is estimated by

$$\omega = \sqrt{\frac{k_{eff}}{m_{eff}}} \tag{1}$$

where k_{eff} is the effective stiffness of the beam, a function of both the mechanical and electrical properties in the case of a piezoelectric bender, and m_{eff} is the effective mass. A more detailed discussion of how the stiffness is determined for a piezoelectric, including an explanation of how it is varied between its open circuit and short circuit conditions, is to follow in later sections.

By using a portion of the beam for sensing and actuating, the cantilever can be made to self-oscillate by feeding the sensor signal through an amplifier and back to the actuator (Lee, 1995). The correct phase and gain, such that the loop contains 360 degrees of phase and enough gain to overcome losses, must be incorporated into the system for self-oscillation to occur.

2.3.2 Surface Acoustic Wave

Surface acoustic waves are acoustic waves propagating along the surface of an elastic substrate, their amplitudes decaying exponentially with the substrate depth. Most often, piezoelectric materials are used as the medium for wave propagation, as the piezoelectric helps initiate the transmission across the resonator (Royer, 2000). Piezoelectric SAW devices are most commonly generated and detected by interdigitated electrodes. Energy is trapped by equipping the device with reflectors on each side of electrodes, and just as in the case of the bending vibrator, the SAW can be made to self-oscillate by incorporating a feedback loop with a single-stage amplifier. SAW devices can be fabricated in non-piezoelectric plates as well, although direct coupling using interdigital electrodes is not applicable in these cases (Rouvaen, 2002).

A basic configuration of a SAW resonator, shown from the top view, is given in Figure 3. Generally, the optimum frequency range for a SAW resonator is between 10MHz and 2GHz. The upper and lower limits of the available frequencies are determined by the device design parameters and the material properties.

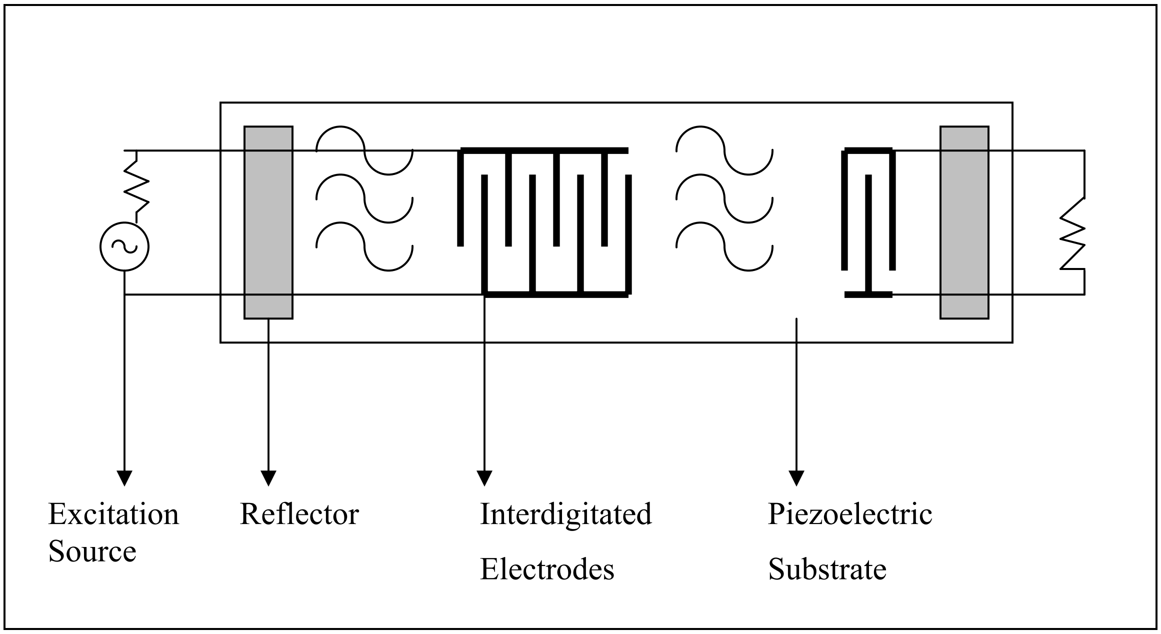

Figure 3. A Surface Acoustic Wave Resonator

The frequency of a basic, single-layer SAW can be found by the formula

$$f = \frac{V_s}{\lambda} \tag{2}$$

where λ is the spacing of the interdigitated electrodes and V_s is the shear acoustic velocity of the wave. Generally, the interdigitated electrodes are spaced at half or fourth wavelengths of the operating frequency of the resonator, and the crystal thickness is twice the wavelength. The acoustic velocity can be equated to

$$V = \sqrt{\frac{\mu}{\rho}} \tag{3}$$

where, again, similar to the bending beam model, μ is the Shear Modulus (a measure of stiffness) of the material, which is a function of both the mechanical and electrical contributions to the system's stiffness, and ρ is the density (a quantity relative to the mass).

When an additional piezoelectric layer (in our case, a tuning layer) is incorporated into the SAW resonator, the resonant frequency of the device is altered. Previously, this change in frequency has been modeled as:

$$\Delta f = -f_o * \frac{V_p}{4} \rho d \left[1 - \left(\frac{V_m}{V_p} \right)^2 \right] [\hat{\mu}]^2_{z=0} \tag{4}$$

for a Love-Wave device (a surface wave propagating in a film on a substrate, where the acoustic velocity in the film is higher than that in the substrate), where f_o is the original frequency, $[\hat{\mu}]^2_{z=0}$ is the particle velocity at the surface of the guiding layer, d is the thickness of the guiding layer, and V_m and V_p are the acoustic velocities of the original piezoelectric layer and the tuning layer, respectively (Du, 1998).

2.3.3 Bulk Acoustic Wave

A film bulk acoustic wave resonator is composed of a piezoelectric layer sandwiched between two metal electrode layers. This configuration must be enclosed by acoustically insulating boundaries, such that energy trapping will occur in the device. Typically, these boundaries are manufactured by an air interface or an acoustic reflector. Acoustic reflectors are formed by alternating materials of high and low acoustic impedance materials on the outside of the FBAR (Salgar, 2002).

A basic configuration of a single layer FBAR resonator with air boundaries, shown from a side view, is displayed in Figure 4.

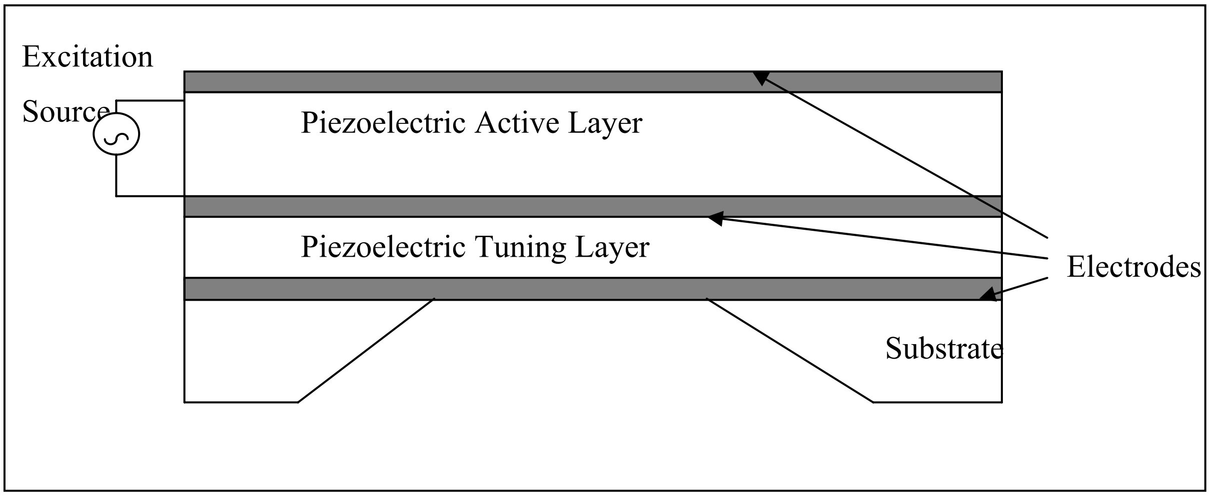

Figure 4. A Film Bulk Acoustic Wave Resonator

FBARs generally oscillate at the upper range of the frequency spectrum, most typically in the area from 1-10 GHz (Yu, 2005). Such high frequency capabilities are becoming increasingly important in many of today's resonator applications, particularly for wireless communications applications.

Mechanical motion is created in the piezoelectric when an RF signal is applied across the device. Resonance occurs when the thickness of the film is equivalent to a multiple of half the wavelength of the input signal, or

$$F_{res} = \frac{1}{\lambda_{res}} = \frac{V_a}{2d} \tag{5}$$

where

$$V_a = \sqrt{\frac{E}{\rho}} \tag{6}$$

F_{res} is the resonant frequency of the device, λ_{res} is the wavelength, and d is the thickness of the film (Norton, 1989).

This formula can be expanded for a multi-layer FBAR, where an additional piezoelectric layer is incorporated for purposes such as temperature compensation. In this case, for a four-layer FBAR (a substrate layer, a piezoelectric layer and 2 electrode layers), the resonant frequency, as given by Zhang, (Zhang, 2003) is equal to:

$$f_p(m_n Z_{sb} + 1) = \frac{m_n z_{sb} + 1}{2(\frac{z_{e1} l_{e1}}{V_{e1}} + \frac{z_{sb} l_{sb}}{V_{sb}} + \frac{z_{e2} l_{e2}}{V_{e2}} + \frac{l}{V})} \tag{7}$$

where $f_p(m_n Z_{sb} + 1)$ is the $(m_n \; + 1)$-order parallel resonant frequency of the FBAR and z, l and V are the acoustic impedance, thickness and acoustic velocity of the FBAR layers, respectively, and the subscripts sb, $e1$, and $e2$ denote the substrate layer, and the first and second electrode layers.

3.0 PIEZOELECTRIC MATERIALS: LITERATURE REVIEW

The piezoelectric effect is a phenomenon describing the direct conversion of electrical energy to mechanical energy, or vice versa, which is characteristic of some materials. Generally, the electrical signal is produced in the form of a voltage, and electrodes are used to facilitate coupling between the electrical and mechanical effects.

The first experiment demonstrating the piezoelectric effect was demonstrated by Pierre and Jacques Curie in 1880. The brothers showed a measurement of electrical charge appearing on the surface of specially prepared crystals that were subjected to a mechanical stress. Proof of the reverse effect (stress in response to an electric field) was not obtained until 1881 when the property was derived by Lippmann using thermodynamic principles and was subsequently experimentally validated by the Curie brothers (Piezo Systems Inc., 2006).

Non-crystalline piezoelectric materials are most commonly ceramics and require poling in order to exhibit their piezoelectric properties. Inherently, this presents a disadvantage of non-crystalline materials with respect to their crystalline counterparts, since the poling can present an additional difficulty in manufacturing, and de-poling can occur at certain voltage and temperature thresholds. Lower resistivity (causing charge leakage at low strains) and temperature-dependence of the material properties are additional problems associated with non-crystalline materials. However, despite these shortcomings, non-piezoelectrics offer advantages in lower processing and manufacturing costs, higher piezoelectric sensitivity and availability of material, which often make them a valuable material choice (Muriuki, 2004).

For piezoelectric MEMS sensors (including resonators), there are many important properties and process considerations that are valuable to evaluate when selecting a material. Foremost is the value of electromechanical coupling, which describes the effectiveness of energy transformation between electrical and mechanical states. In addition, resistance to environmental effects (e.g. temperature, humidity) and aging, semiconductor process compatibility, and good adhesion to substrate materials are all important material properties to consider. Cost effectiveness and ease of processing (including time, repeatability, expense, etc.) are manufacturing concerns that should be accounted for as well.

It is important to note that piezoelectric material properties are highly dependant on orientation. To account for this, standard definitions of the axes in piezoceramics have been identified. The axes termed 1, 2 and 3, are analogous to the traditional three dimensional orthogonal axes X, Y and Z. The polar (3) direction is assumed as parallel to the direction of polarization in the ceramic and is defined during the polarization step of the manufacturing process. When the mechanical stress or strain is shear, the subscript 5 is used in the second place.

For piezoelectric constants relating electrical and mechanical states, double subscripts are necessary. In these cases, the first subscript denotes the direction of the electric field associated with the applied voltage (or the resulting charge produced), and the second subscript describes the direction of the mechanical stress or strain. Electromechanical coupling constants use this double-subscript notation, and for this work, the d_{31} and d_{33} constants are of particular importance. For resonators, in poling a piezoelectric film across the thickness of the device, the applied stress and poling directions are perpendicular, and thus the d_{31} response is elicited. An example of a beam under this type of poling is shown in case A. of Figure 5. If, however, the piezoelectric poling direction is in-plane with the applied stress, the d_{33} response results, as is the case in an interdigitated electrode configuration like that shown in case B. of Figure 5.

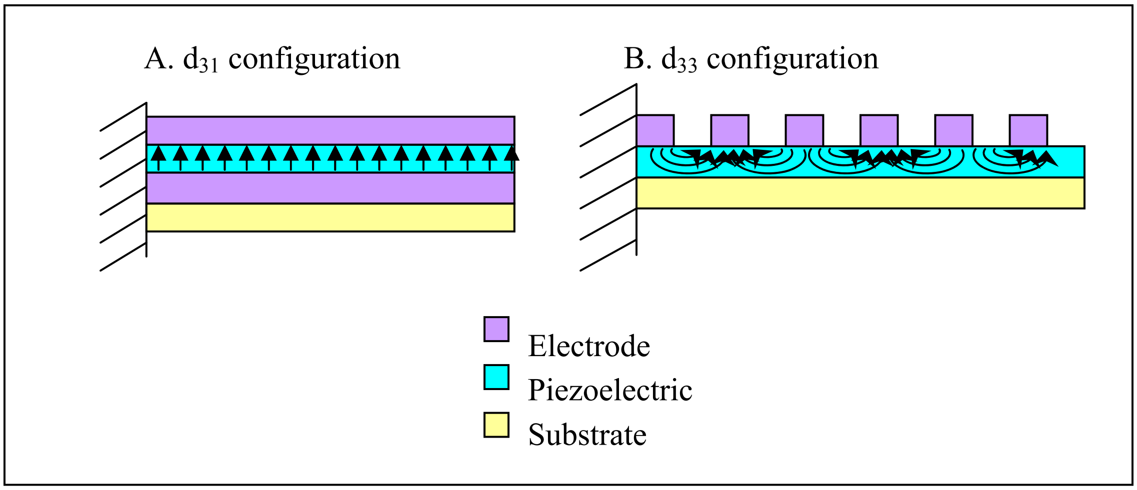

Figure 5. Schematic of d_{31} and d_{33} (interdigitated) piezoelectric beams

Since, for many piezoelectric materials the d_{33} piezoelectric coefficients are twice as large as their d_{31} counterparts, the use of interdigitated electrodes can enable a greater amount of electrical to mechanical conversion (Zhang, 2003). D_{33} devices can also have advantages in terms of simplified, more cost-efficient processing, since one less lithography, deposition, and etching process are inherent in the design.

For microelectromechanical systems, Zinc Oxide (ZnO), Aluminum Nitride (AlN) and Lead Zirconate Titanate (PZT) are the most commonly used materials for the sensor industry (Sze, 1994). While the pros and cons of each of these materials with respect to tunable MEMS resonators will be discussed here briefly, and theoretical simulations will be run for resonators of each of these materials in both the bending beam and FBAR models, the focus of the processing discussion will be on PZT, since this was the material used in this project's experimental fabrication portion.

Zinc Oxide was the first piezoelectric material to be used for commercial applications (Sze, 1994) and, consequently, is the most widely researched when it comes to MEMS fabrication studies (McKinstry, 2004). In addition, ZnO is widely available and has shown a large degree of success in fabrication. Less demanding vacuum conditions, high sputtering rates, good film quality, and ease of chemical etching are all processing benefits characteristic of ZnO (McKinstry, 2004 and Francombe, 1990). Furthermore, ZnO has a relatively high piezoelectric coupling factor (Sze, 1994).

Despite these advantages, ZnO is not perfectly compatible with semiconductor technology, has problems with increased conductivity, and is subject to issues of temperature dependence of resonator properties (McKinstry 2004 and Yu, 2005). Aluminum Nitride, on the other hand, offers distinct advantages in many of these areas. It displays good endurance under humidity and temperature variations, has a large resistivity, and is perfectly compatible with CMOS processing. Additionally, its high acoustic velocity makes it distinctly advantageous for high-frequency applications like film bulk acoustic resonators (Su, 2001), and its high quality factor (also a trait of ZnO devices) is beneficial in all resonator applications. Unfortunately, it too has its drawbacks, in particular a lower electromechanical coupling value than the others addressed here (although still high in comparison to many thin-film piezoelectrics). Since, in this work, electromechanical coupling is directly related to the tunability of the device, this is a strong disadvantage for this application.

Correspondingly, PZT is most widely recognized among piezoelectric thin-film alternatives for its extremely high piezoelectric coupling. Often, the electromechanical coupling of PZT is more than an order of magnitude larger than ZnO or AlN (Sze, 1994), and thus is an excellent material for such applications as this tunable resonator, or other applications utilizing electromechanical coupling, such as energy harvesting devices (Jeon, 2005).

PZT's potential as a highly coupled piezoelectric has attracted many researchers to the search for an effective thin-film processing technique. Electron-beam evaporation, RF sputtering, ion-beam deposition, epitaxial growth by RF sputtering, magnetron sputtering, MOCVD, laser ablation, screen printing, jet deposition and sol gel methods have all been investigated, with RF sputtering and sol-gel deposition drawing the largest amount of attention (Kim, 2004 and Sze, 1994). Each of these processes differs in their processing requirements and applicability, particularly with respect to such parameters as required annealing temperatures or desired film thicknesses. This can be important since many applications put strict limitations on these parameters, since certain film thicknesses may be necessary for particular devices (Jeon, 2005) and semiconductor-compatibility puts restrictions on annealing temperatures.

For smaller film thicknesses, RF sputtering is usually the fabrication process of choice. Advantages include good step coverage (particularly in patterns with features having high aspect-ratios between their depths) (Jeon, 2005F), high-quality surface topologies with good grain boundaries (Sze, 1994), and the general familiarity with sputtering within the MEMS processing community. Works by Abe et. al (Abe, 1994 and 1995) and Sakata et. al (Sakata, 1996) have shown some promising results of high-quality, sputtered PZT films.

There are, however, a good many problems associated with the PZT sputtering technique. Generally, the high temperatures associated with the required annealing, particularly with respect to the fast changes in wafer temperature characteristic of the rapid thermal annealing technique, have been shown to cause cracking in the PZT film (Abe, 1995). This is particularly problematic for smaller-featured devices. Processing trials by the author using this technique have supported this finding, as will be discussed in later notes. Also, the quality of the results and properties of sputtered films are highly dependant on many process conditions, such as substrate temperature, gas combination, pressure inside the chamber, RF power, deposition time and geometry between the substrate and target (Sze, 1994 and Abe, 1995). These stringent processing constraints make it undesirable to many applications, particularly for industrial uses.

The sol-gel technique has been the most widely employed fabrication method for PZT films, showing high-quality results of good surface topology and good performance. (Sakata, 1996, Abe, 1994, Hendrickson, 1996, and Jeon, 2005). As compared to the sputtering approach, the vacuum chamber is not necessary and composition is much more easily controlled. Deposition over large, flat surfaces is much easier with the sol-gel technique (Jeon, 2005) and better results are found in terms of film homogeneity (Sze, 1994) Finally, sol-gel processing results in easier integration with CMOS processes. For the most reliable results, sol-gel deposited films are usually kept below a couple of microns in thickness.

Sol gel deposition is a basic spin coating technique for applying thin film materials. In sol gel processing, a small puddle of fluid (sol) is squeezed from a dropper onto the center of a substrate. Different sols have different spin coating recipes where the time and speed of the spin cycle is correlated to obtain a quality, uniform film across the surface of the wafer. Spin recipes are a function of the properties of the sol (viscosity, drying rate, percent solids, surface tension, etc.) (Cost Effective Equipment, 2006).

For the ZrO_2 and PZT sols used in this fabrication, the spin coating steps are followed by a pyrolysis (drying) step and an annealing step. These serve to dry the sol gel solution and to alter the crystal structure of the piezoelectric material for proper alignment, respectively.

4.0 THEORETICAL MODELING OF TUNABLE RESONATORS

4.1 GENERAL TUNING CIRCUIT CONDITIONS

The basic premise for the tuning concept applied in this work is the idea of a variable stiffness, whereby the modulus of a piezoelectric element is adjusted through varying shunt capacitance conditions. Since, as will be shown later in detail, the elastic modulus of piezoelectric materials is often a parameter in determining the resonant frequency of an oscillator, a change in this modulus will result in a change in the frequency of the device. Furthermore, a ratio of the open circuit to closed circuit stiffness or frequency can provide a quantitative measure of the degree of tunability of the device.

Figure 6 shows the three basic possibilities for circuit conditions applied to a piezoelectric element of a resonator. The total capacitance is equal to the sum of the contributions from the piezoelectric layer and the shunt capacitance.

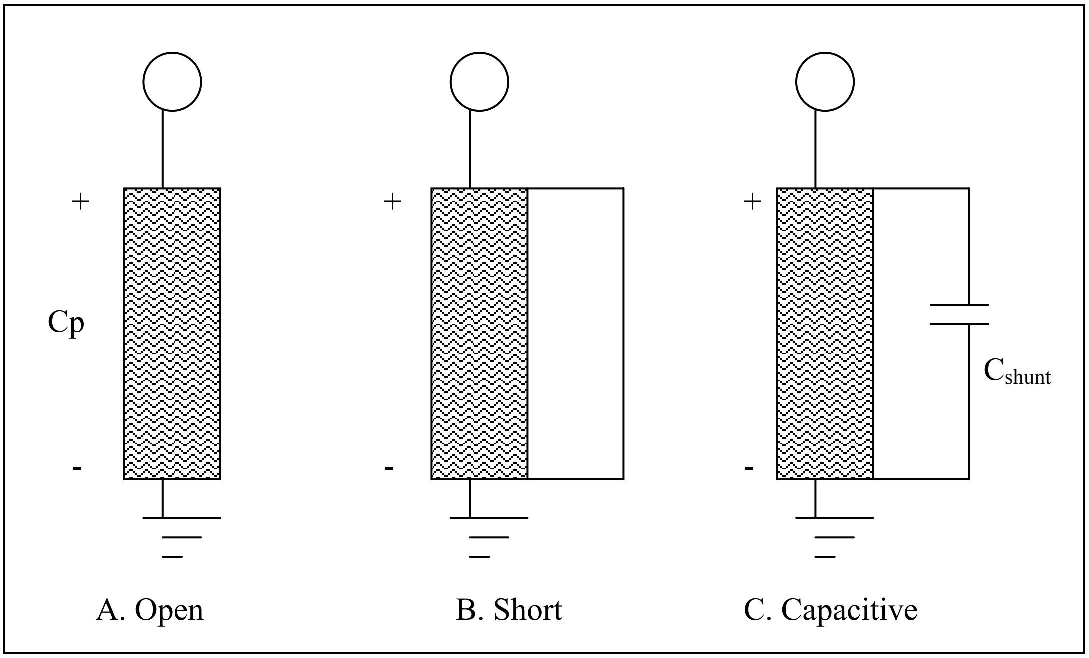

Figure 6. Shunt Capacitor Tuning Applied to Basic Piezoelectric Element

In case A, the piezoelectric is left open circuited; hence, the capacitance is equal to that of the piezoelectric layer. In this situation, the effective modulus of the piezoelectric layer is a function of both this capacitance, and the material compliance of the layer, given by:

$$E_p = E_{oc} = (S^E - \frac{d^2}{\varepsilon_p})^{-1} \tag{8}$$

This is the maximum stiffness condition of the resonator, and hence is the stiffness term used in evaluating upper frequency limits of the tunable resonators.

If the electrodes surrounding the tuning piezoelectric are short circuited, as in case B, then the capacitance of the piezoelectric element is equal to zero and the electromechanical coupling does not affect the stiffness. Consequently, the Young's Modulus of the piezoelectric layer is simply equal to the inverse of the compliance for the piezoelectric material, or:

$$E_p = E_{sc} = (S^E)^{-1} \tag{9}$$

This results in the minimum stiffness condition for the piezoelectric layer, which is analogous to the lower frequency limit of resonators.

Since these two conditions define the upper and lower limits on the variable stiffness of the system, they are also the stiffness terms used to calculate the limits on the range of tunable frequencies. A capacitance can also be added in parallel with the piezoelectric layer to vary the stiffness between its two extreme conditions (case C), in which case the modulus is equal to:

$$E_p = E_{oc} = (S^E - \frac{d^2}{\varepsilon_p} + Z_{sh})^{-1} \tag{10}$$

where Z_{sh} is the impedance of the shunt capacitor. Consequently, the frequency can be adjusted to any value between its upper and lower limits by selecting the appropriate capacitive shunt.

In the following sections, the variable stiffness concept just described is applied to three different types of resonators: a bending beam resonator, a surface acoustic wave resonator, and a film bulk acoustic wave resonator. Models are developed for each of the resonators which incorporate the modulus of the piezoelectric layer as one of the variables impacting the resonant frequency of the device. A focus is put on the interdigitated design, since these are the devices to be fabricated. Parameter studies are conducted on the resonators to see the effects which varying different device properties (thicknesses, materials, electrode placement, etc.) have on the important resonator parameters (namely, the degree of tunability, as well as the resonant frequency).

4.2 BENDING BEAM MODEL

4.2.1 Background/Derivation

For this model, the resonator is treated as a cantilever beam undergoing bending vibrations, so in this section, a simplified model of the cantilever beam is developed to provide an expression for a bending beam's resonant frequency (fundamental mode) in terms of the beam's parameters. Both the d_{31} and d_{33} bending beam configurations described previously are studied, although special attention is paid to the parameter investigation of the interdigitated design since this device has not been previously investigated and has significant advantages in MEMS resonator applications, as discussed in earlier sections. When used as a self-oscillating device, it would be necessary to segment the beam into sensing, actuating and tuning sections, where the signal was fed from the sensor through an amplifier and back to the actuator; however, for purposes of the parameter study, the entire beam is assumed to be a passive, tuning portion.

For a flexible beam subject to a load P at the end (Figure 7), which causes deflection y in the beam, the effective stiffness (K_{eff}) can be found from the equation for spring stiffness:

$$P = K_{eff}\, y \tag{11}$$

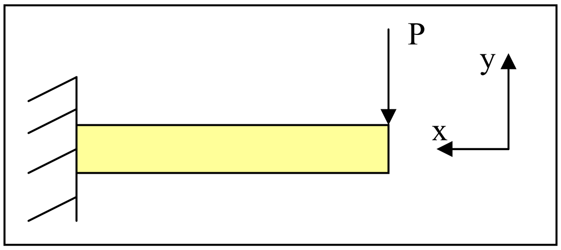

Figure 7. Basic Cantilever Beam Subject to a Loading at its End

From mechanics, the differential equation governing the deflection of this beam is:

$$\frac{d^2y}{dx^2} = \frac{M(x)}{EI} \tag{12}$$

where M is the moment of inertia, E is the modulus of elasticity and I is the moment of inertia.

First, the assumptions are made that the beam is subject to the constraints of deflection and angle equal to zero at its clamped end. In the d_{31} case of the beam (Figure 8), where electrode layers cover the entire beam both above and below the piezoelectric layer, the deflection equation for the beam subject to a load at the end can then be written as:

$$y = \frac{P}{6EI}(-x^3 + 3L^2x - 2L^3) \tag{13}$$

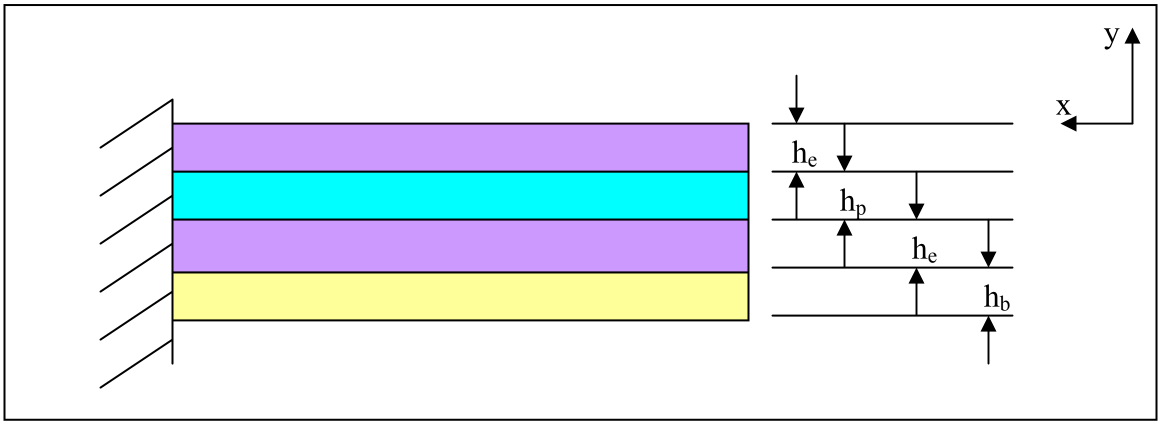

Figure 8. D_{31} Cantilever Beam with Multiple Layers Subject to a Loading at its End

where L is the length of the beam and x is the relative position across the length. The maximum deflection occurs at the end of the beam (x=0). Here, the equation is equal to:

$$y = \frac{-PL^3}{3EI} \tag{14}$$

making the effective stiffness:

$$K_{eff} = \frac{3EI_{eff}}{L^3} \tag{15}$$

where EI_{eff} is the flexural rigidity of the beam.

Since the beam has multiple layers as shown in Figure 9 A. (2 electrode layers, a substrate layer, and a piezoelectric layer), the modulus of elasticity is not constant through the depth, meaning that the flexural rigidity must be derived. To account for this, an effective rigidity is calculated for an equivalent beam made entirely of the modulus of the substrate material, but whose electrode and piezoelectric layers have a different width as shown in Figure 9 B. Here, the original widths of the PZT and electrode layers are multiplied by the ratios of the Young's modulus of their respective materials to that of the substrate (n and m), where the subscripts p, b and e represent the piezoelectric, substrate and electrode layers, respectively.

$$n = \frac{E_p}{E_b} \quad m = \frac{E_e}{E_b} \tag{16}$$

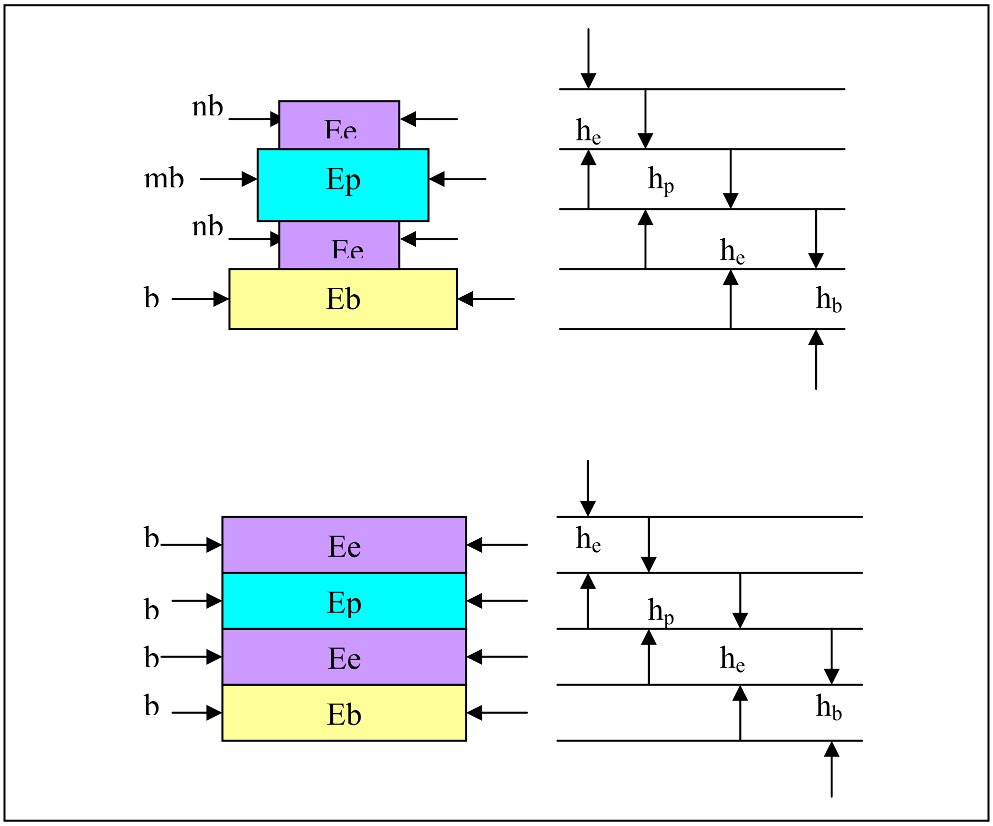

Figure 9. Unimorph Cantilever Beam with Multiple Layers of Different Moduli

A corresponding centroid and moment of inertia can then be calculated for this multilayer beam, equal to:

$$\overline{Y} = \frac{\sum A\overline{y}}{\sum A} = \frac{\begin{matrix}[(bh_b)(h_b/2)] + [(mbh_{e1})(h_b + h_{e1}/2)] + \\ [(nbh_p)(h_{e1} + h_b + h_p/2)] + \\ (mbh_{e2})(h_{e1} + h_b + h_p + h_{e2}/2)]\end{matrix}}{[(bh_b) + (mbh_{e1}) + (nbh_p) + (mbh_{e2})]} \tag{17}$$

and

$$
\begin{aligned}
I_{eff} &= \frac{1}{12} b h_b{}^3 + b h_b (\overline{Y} - h_b/2)^2 + \\
&\frac{1}{12} m b h_{e1}{}^3 + m b h_{e1} (\overline{Y} - (h_b + h_{e1}/2))^2 + \\
&\frac{1}{12} n b h_p{}^3 + n b h_p (\overline{Y} - (h_{e1} + h_b + h_p/2))^2 + \\
&\frac{1}{12} m b h_{e2}{}^3 + m b h_{e2} (\overline{Y} - (h_{e1} + h_b + h_p + h_{e2}/2))^2
\end{aligned}
\qquad (18)
$$

respectively, where h is the layer height, b is the layer width and the subscripts 1 and 2 designate properties of the first (top) and second (bottom) electrodes, respectively.

In the interdigitated d_{33} case shown in Figure 10, the flexural rigidity is not constant throughout the length of the beam and, consequently, must be expressed as a piecewise function of x before Equation. 12 can be integrated to find a deflection equation for the beam.

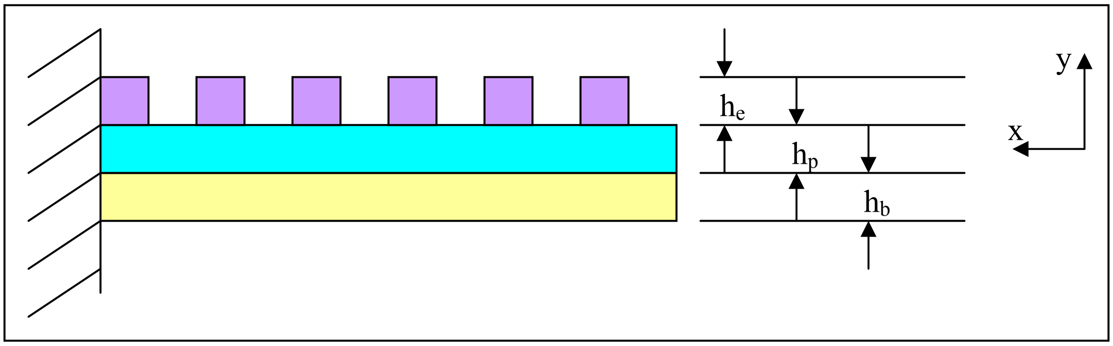

Figure 10. D_{33} (Interdigitated) Cantilever Beam with Multiple Layers Subject to a Loading at its End

For any electrode or spacing segment, the deflection at any point along the beam can then be found as:

$$y = \frac{1}{EI_{eff}}(-\frac{1}{6}Px_{end2}^{\ 3} + (EI_{eff}\theta_{end1} + \frac{1}{2}Px_{end1}^{\ 2})x_{end2} + \\ EI_{eff}y_{end1} + \frac{1}{6}Px_{end1}^{\ 3} - \frac{1}{2}Px_{end1}^{\ 3}) \qquad (19)$$

where x_{end1} is the length along the beam at the beginning of the segment, x_{end2} is the length at the end of the segment, y_{end1} is the deflection at the beginning of the segment and θ_{end1} is the angle at the beginning of the segment.

This equation can be used to find the maximum deflection at the end of the beam by beginning with the initial conditions of zero deflection and zero angle at the clamped end, where h_{e1} equals 0 and h_{e2} is the height of the interdigitated electrode in Equations 17 and 18, solving for the deflection and angle at the end of the first electrode, using these solutions as the initial conditions for the deflection in the spacing segment, where both h_{e1} and h_{e2} equal zero in Equations 17 and 18, and continuing this process along the length of the beam.

In both the d_{31} and d_{33} cases the material modulus can be changed by short or open-circuiting the piezoelectric portion of the beam as described previously (general tuning circuit conditions section). In doing so, the ratios of elasticity in the beam (Equation 15) are changed, affecting the values of the beam centroid and the moment of inertia (Equations 16 and 17), resulting in an alteration of the displacement of the beam. Equation 11 ($P = K_{eff}y$) can then be used to find the stiffness value corresponding with this value of deflection. Since the equation for the fundamental frequency of a single mode of vibration associated with a one degree of freedom system is given by:

$$\omega = \sqrt{\frac{K_{eff}}{m_{eff}}} \tag{20}$$

it becomes evident that a stiffness change achieved via the shunt capacitor tuning presents a means for varying the resonator's frequency. Thus a frequency ratio, equal to the open circuit frequency divided by the short circuit frequency, or:

$$\frac{\varpi_{oc}}{\omega_{sc}} = \sqrt{\frac{K_{eff\,(oc)}}{K_{eff\,(sc)}}} \tag{21}$$

can provide a quantitative measure of a bending beam resonator's tunability.

4.2.2 Simulation Results

Table 2 gives the parameters used in the modeling of the system. In all of the analyses except for the ones specifically varying a layer's material, aluminum was used as the substrate, platinum was used as the electrode and PZT was used for the piezoelectric.

Table 2. Estimated Thin Film Material Properties for Beam Layers: Bending Beam Simulations

Parameter	Variable	Value	Units
AlN piezoelectric strain constant 31	d_{31}	2.60E-12	m/V
AlN piezoelectric strain constant 33	d_{33}	5.10E-12	m/V
ZnO piezoelectric strain constant 31	d_{31}	5.43E-12	m/V
ZnO piezoelectric strain constant 33	d_{33}	1.17E-11	m/V
PZT piezoelectric strain constant 31	d_{31}	1.90E-10	m/V
PZT piezoelectric strain constant 33	d_{33}	3.90E-10	m/V
AlN relative permittivity	ε	9	
ZnO relative permittivity	ε	9.16	
PZT relative permittivity	ε	1.80E+03	
AlN young's modulus	E_p	3.31E+11	Pa
ZnO young's modulus	E_p	1.96E+11	Pa
PZT young's modulus 31	E_{p1}	6.60E+10	Pa
PZT young's modulus 33	E_{p3}	5.20E+10	Pa
Al young's modulus	E_s	7.00E+10	Pa
Steel young's modulus	E_s	2.00E+11	Pa
SiNx young's modulus	E_s	2.00E+11	Pa
*for all but comparison, Al used			
Pt young's modulus	E_e	1.70E+11	Pa
Au young's modulus	E_e	8.00E+10	Pa
*for all but comparison, Pt used			

A ratio of the thickness of the substrate layer to the piezoelectric layer is used as a baseline parameter for measuring the change in frequency available for different electrode configurations. In this section, this beam thickness ratio will be used to optimize the electrode conditions of the beam. It has been previously demonstrated by Clark (Clark, 2000) that as the ratio of substrate thickness to piezoelectric thickness decreases, the available change in stiffness (and therefore, frequency) decreases as well. Some variations exist in this result for smaller thickness ratios, a result which can be attributed to the fact that the beam's centroid is actually inside the piezoelectric layer. When this is the case, some cancellation will occur in the available tunability, since a portion of the beam is in tension and a portion is in compression. Thus to really maximize the piezoelectric tuning, the beam must be designed so that the centroid occurs below the piezoelectric layer. For this work, this usually occurs at thickness ratios greater than 1, and thus these results should be used as a more accurate judgment of a beam's tunability.

Figure 11 shows the ratio of substrate thickness to piezoelectric thickness plotted against the frequency ratio for conditions of the basic d_{31} case, and the extreme conditions of the d_{33} case (the entire top layer covered by the electrode or the entire top layer being "spacing" between interdigitated electrodes). Although neither of these two extreme conditions is realistic in practice, they represent the theoretical boundaries of the maximum and minimum frequency change available for the d_{33} configuration.

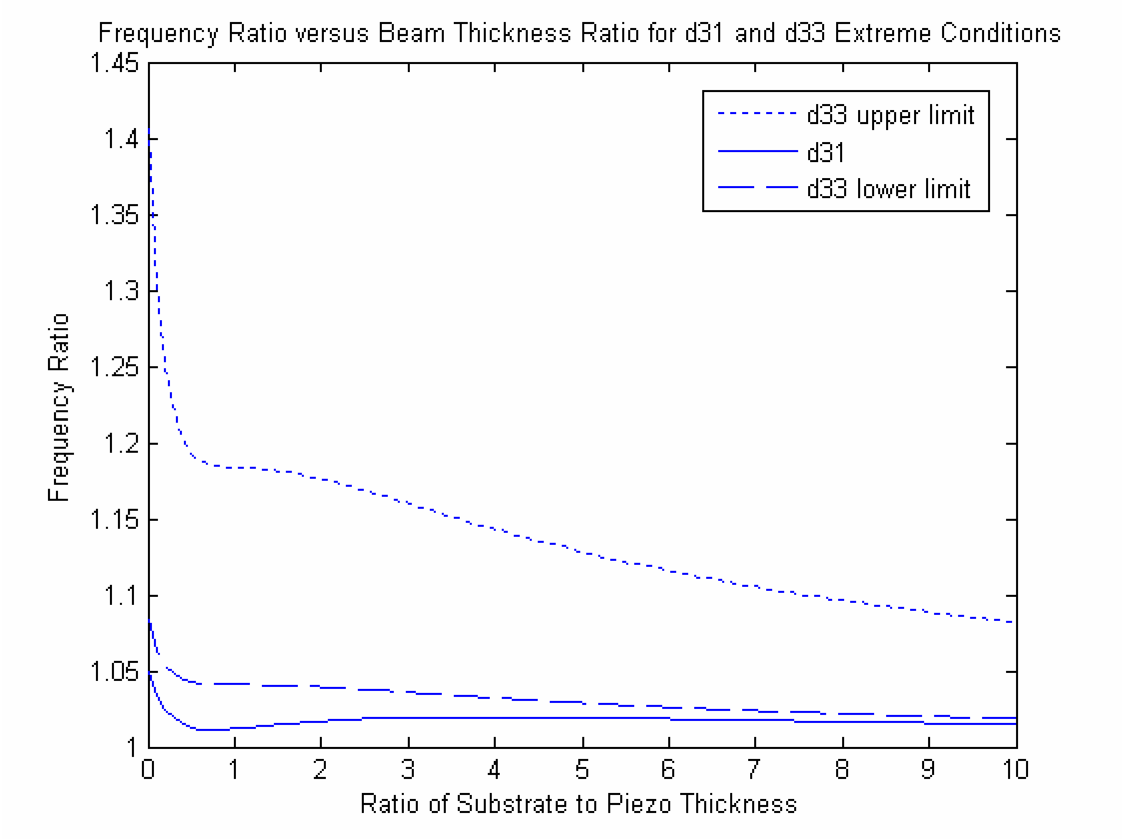

Figure 11. Frequency Ratio Versus Beam Thickness Ratio for d_{31} and d_{33} Extreme Conditions

Figure 11 demonstrates that the difference in available tunability between the d_{31} case and the d_{33} minimum is negligible: what difference does exist can be attributed to the additional stiffness present due to the additional electrode layer in the beam, since the d constant remains the same for both cases. For zero substrate thickness, the frequency ratio in the d_{33} case varies from 1.085-1.4 at its extreme conditions, meaning that the stiffness value can be adjusted 8.5% at the lowest extreme and 40% at the theoretical upper limit. At a more realistic 1.5 ratio between the substrate and the piezoelectric thickness, the frequency ratio in the d_{33} case varies from 1.041-1.184 (4.1-18.4% change in stiffness value), with a value of 1.012 (1.2% change) for the d_{31} case. It is important to note that these values represent dramatic changes in stiffness for a resonating device, both generally, in terms of need, and as compared to previous methods (see resonator tuning literature review).

Optimizing the d_{31} case is a relatively straightforward problem since there are very few design parameters that affect the stiffness of the beam. In addition, most of the parameters (such as material selection) which do have effects in the d_{31} instance apply to the d_{33} case as well. For the interdigitated case, there are many parameters to vary. The following paragraphs will discuss the effects which changing these parameters have on the amount of frequency tunability.

For interdigitated beams, such as those shown in Figure 10, it is important to note that the assumption made about the state of the electric field under the electrode does make some difference on the resulting frequency tuning. For a most conservative case, the d constant can be set equal to zero, resulting in no difference between the open circuit and short circuit cases for the stiffness of the beam in those areas. For the liberal case, the constant can be taken as the d_{31} constant. The effect which the assumption has on the frequency change varies with the number of electrodes, electrode length and electrode spacing; however, Figure 12 shows one example of how the more conservative estimate offers a lower amount of tunability.

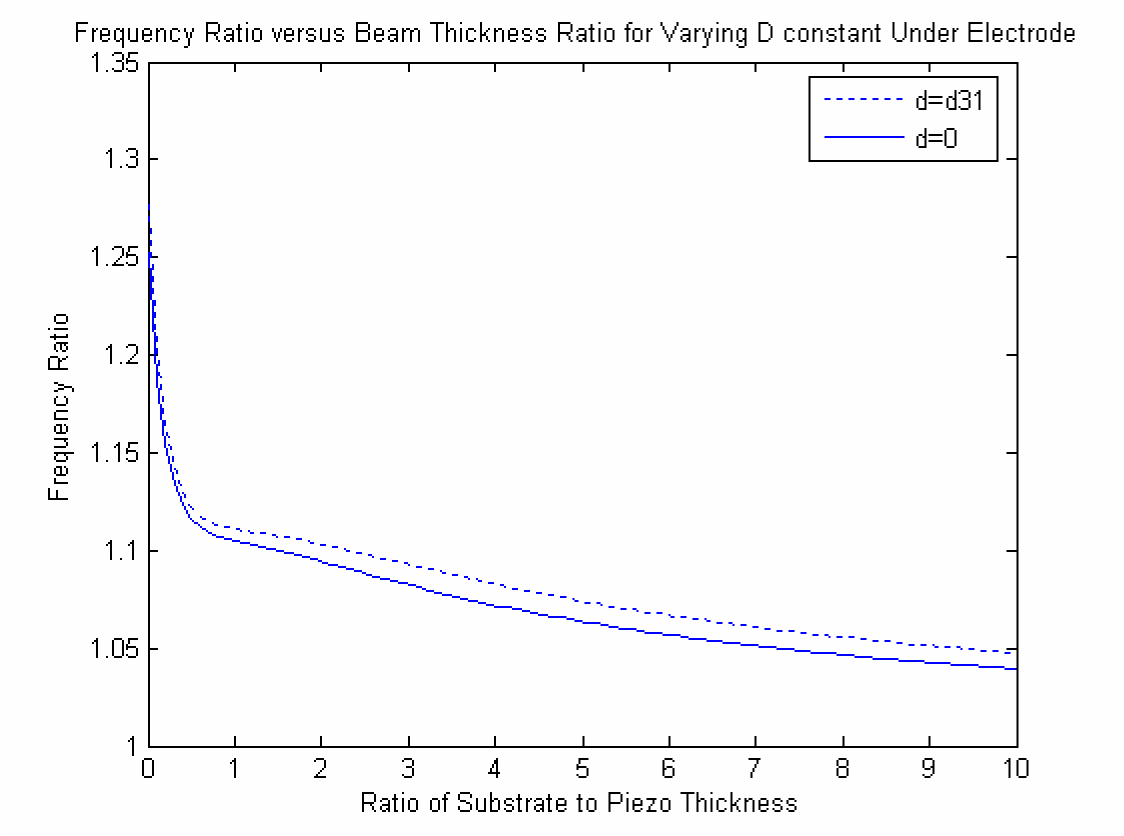

Figure 12. Beam Stiffness Ratio Versus Beam Thickness Ratio for Extreme Assumptions of d Constant under Electrode

If the number of electrodes and the length of the beam are held constant, one can observe the effect that changing the electrode length has on the ability to change the beam stiffness. Figure 13 shows the relationship between the frequency ratio and the amount of electrode covering the beam at a constant electrode number of fifteen.

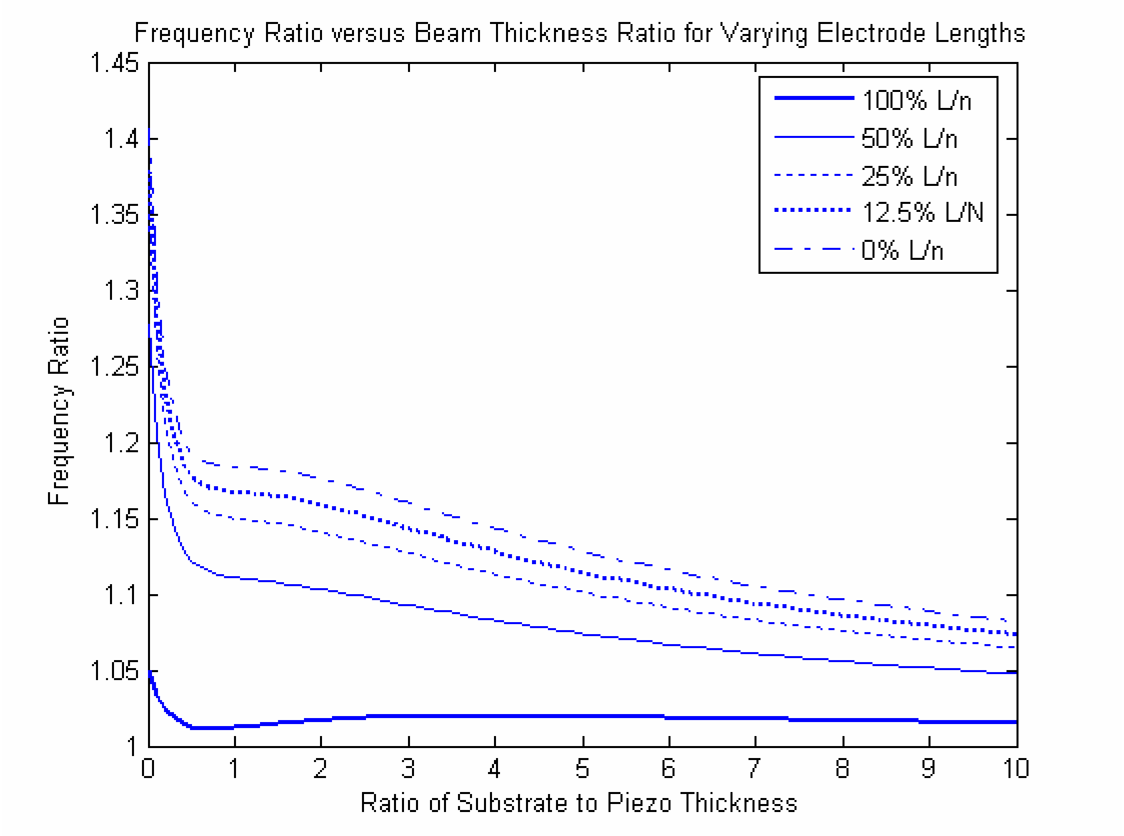

Figure 13. Beam Stiffness Ratio Versus Beam Thickness Ratio for Varying Electrode Lengths

Figure 13 demonstrates that as the length of the electrode decreases (that is, a lesser percentage of the PZT is covered with the electrode material, which from Figure 10 indicates that a greater portion of the PZT is acting in the d_{33} mode), the frequency ratio increases, an effect of a larger area of the beam being governed by the d_{33} constant and the thinner, lower stiffness portion of the beam. It is important to address the fact that, although the theoretical model predicts the highest available tunability for an infinitely small electrode, this is not practical in reality. Not only do limits exist on the fabrication ability for such small features, but more importantly, the issue must be addressed as to the voltage necessary to establish an electric field which can penetrate the entire depth of the piezoelectric layer. The model does not currently address this concern, and more research should be done in order to fully understand the limitations this puts on the design. This becomes especially important for smaller numbers of electrodes, where the spacing is particularly large at smaller electrode lengths.

It is known from mechanics that the deflection of a beam with a point force applied to its free end is not linear across the length of the beam. Similarly, it is accepted that the strain and deflection occurring in a cantilever beam will vary across the length of the device. Consequently, the conclusion can be drawn that the amount of frequency change available for a given piezoelectric composite beam with a certain number of electrodes is dependant upon the spacing of these electrodes across the length of the beam. The electrode configuration can thus be designed in such a way as to optimize the available tunability for a given number of electrodes of equal length.

Figure 14 demonstrates how at a constant number of electrodes and a constant electrode length, the amount of spacing can be varied across the length of the beam.

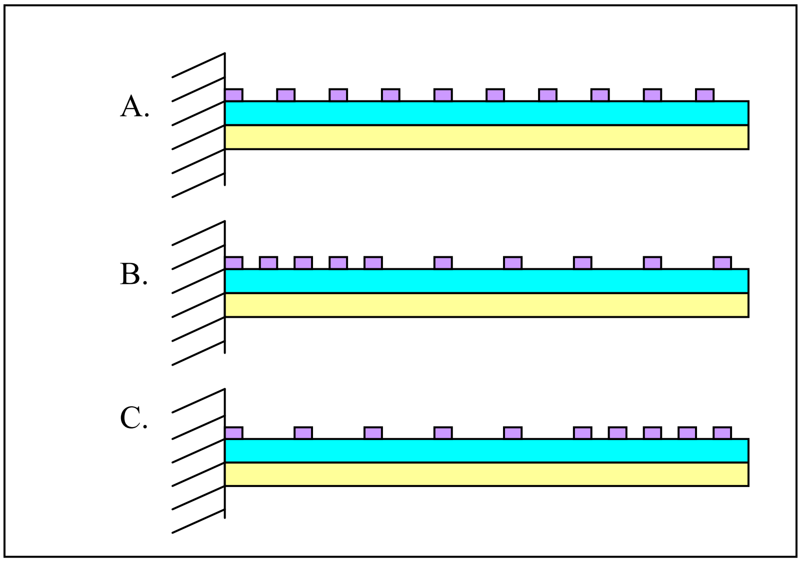

Figure 14. D_{33} (Interdigitated) Electrode Beams with Varied Electrode Spacing Along the Beam

The results of a similar analysis are shown in Figure 15. Here, the number of electrodes is kept constant (n=15), and the electrode length is set equal to half of the length divided by the number of electrodes, but the spacing is varied between 25% of this dimension and 75% of this dimension between the first half and second half of the electrodes. It can be seen that with less spacing near the free end (more spacing near the clamped end), or a configuration of the electrodes similar to that shown in case B of Figure 14, a higher frequency ratio is possible, a result of the fact that a higher amount of strain is present at the clamped end of the beam. One can note that these spacing considerations could also play a very important role in designing a self-oscillating device which incorporates a sensing and actuating segment along with the tuning portion.

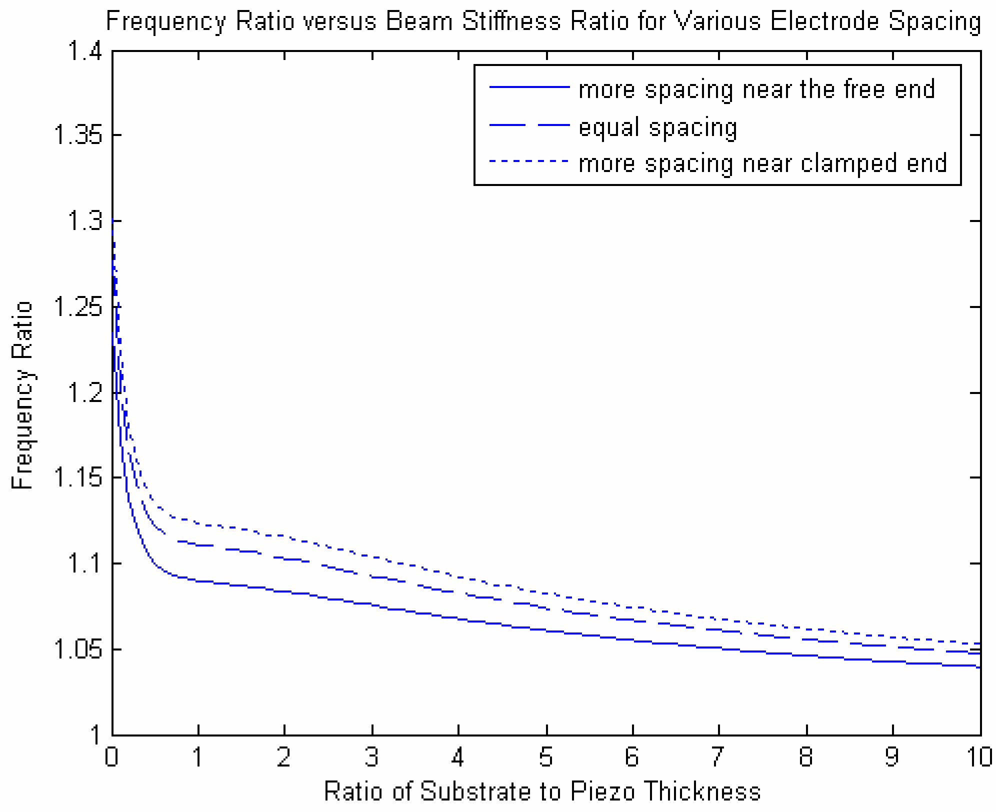

Figure 15. Beam Stiffness Ratio Versus Beam Thickness Ratio for Varied Electrode Spacing

Figure 16 displays the results of frequency ratio versus substrate to piezoelectric ratio while varying the number of electrodes, under conditions of constant electrode spacing throughout the beam.

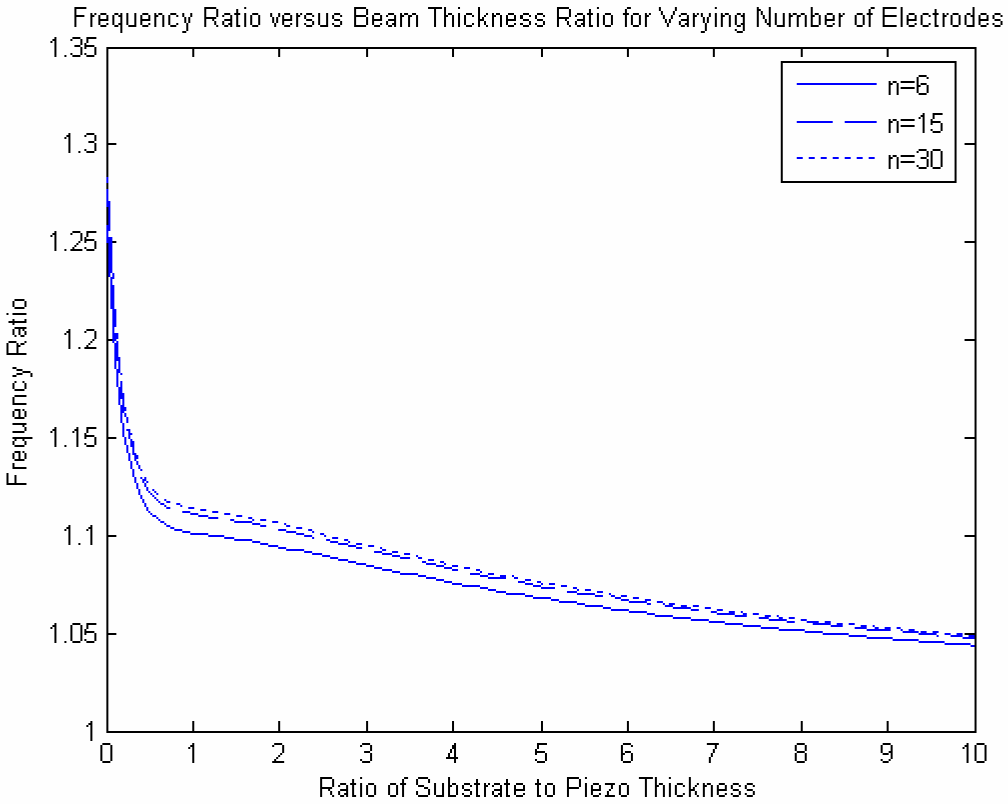

Figure 16. Beam Stiffness Ratio Versus Beam Thickness Ratio for Varying Number of Electrodes

It can be seen that a higher frequency ratio results from a greater number of electrodes, but that there are diminishing returns as this number becomes increasingly large. This result is another effect of the varying strain across the length of the beam, combined with the assumption in the model that the first segment of beam is an electrode segment. For smaller number of electrodes, the effect demonstrated is similar to that shown in varying spacing throughout the length of the beam; however, as the number of electrodes increases, there is less strain difference between electrode and spacing segments, and thus the increase in frequency ratio becomes less substantial.

For the next analysis, a constant number of electrodes (n=15) and equal electrode length and spacing was assumed for studies on devices of three different piezoelectric materials; Aluminum Nitride, Zinc Oxide and Lead Zirconate Titanate. The results of the simulation are shown in Fig. 17.

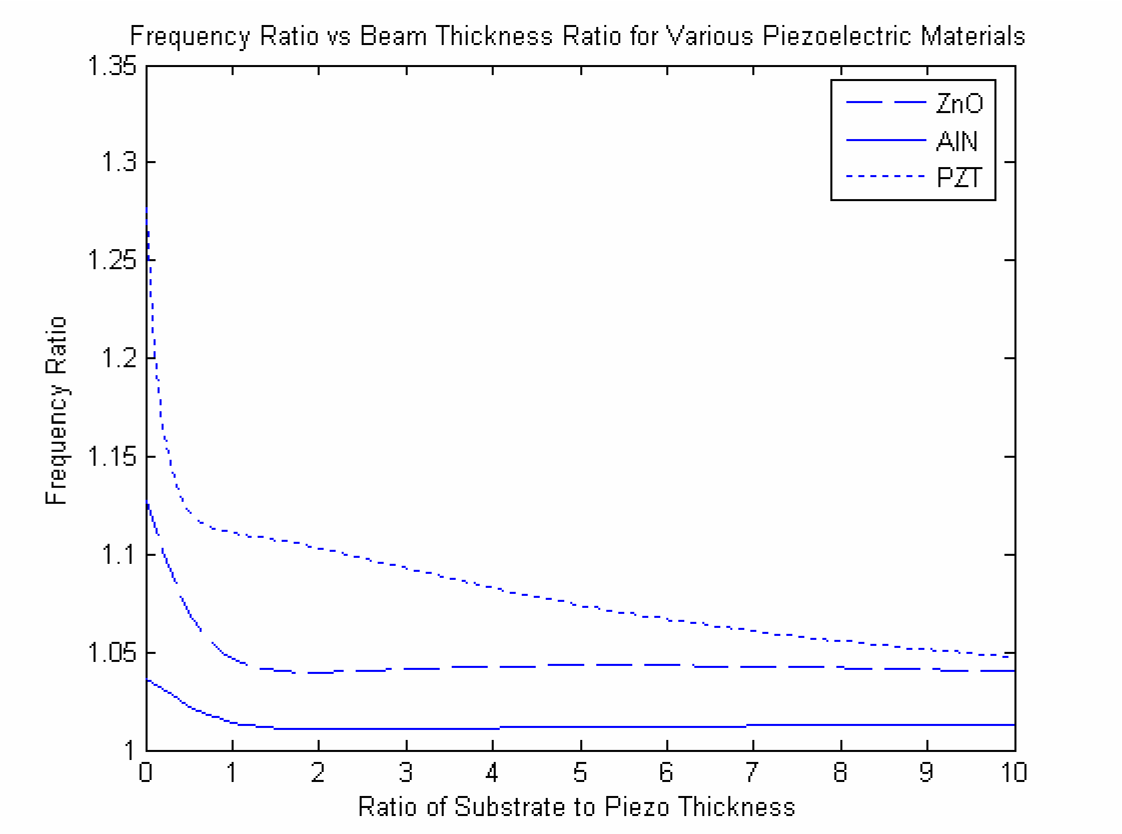

Figure 17. Beam Stiffness Ratio Versus Beam Thickness Ratio for Varying Piezoelectric Materials

As this graph demonstrates, the largest change in frequency results when the piezoelectric layer is made of PZT. This is logical since PZT has the highest electromechanical coupling of the three materials. The graph also demonstrates, however, that significant changes in frequency are still achievable for the other materials, with ZnO offering a better result than AlN. Since these materials offer additional benefits in areas such as processing and quality factors, the results of these analyses, in combination with more particular information about the other pros and cons, could be used to determine which material is best suited for a particular application. The frequency changes for each material could also be optimized in accordance with the results of the previous analyses.

Changing the other beam materials, the substrate and the electrode, can affect the resonator's tunability as well. Getting a quantitative measure of exactly how much change can result is difficult since well-defined material property values are hard to find, particularly for MEMS thin film materials, since new types of tests are necessary for evaluating material properties on this scale, and processing conditions can radically change the results from trial to trial. However, using averages of the parameters, some general trends and design considerations can still be noted.

Figure 18 evaluates the stiffness ratio available for beams with substrates of steel, aluminum, and silicon nitride. The number of electrodes (n=15), the length of the electrode (L/30) and the spacing (L/30) were held constant. While steel and aluminum would be more likely used on beams manufactured on the macro scale, the fact that they have very different moduli (200 GPa for steel and 70GPa for aluminum) makes them desirable for a material comparison. SiNx was used as a third material, since this is the primary material of the substrate that was used in the MEMS wafer fabrication. As Table 2 shows, the modulus for silicon nitride can be estimated to be the same as steel, although this is a very vague estimate since property tests have measured moduli ranging from as low as 85GPa to as high as almost 400GPa for MEMS applications using this material (MEMS and Nanotechnology Clearinghouse, 2006).

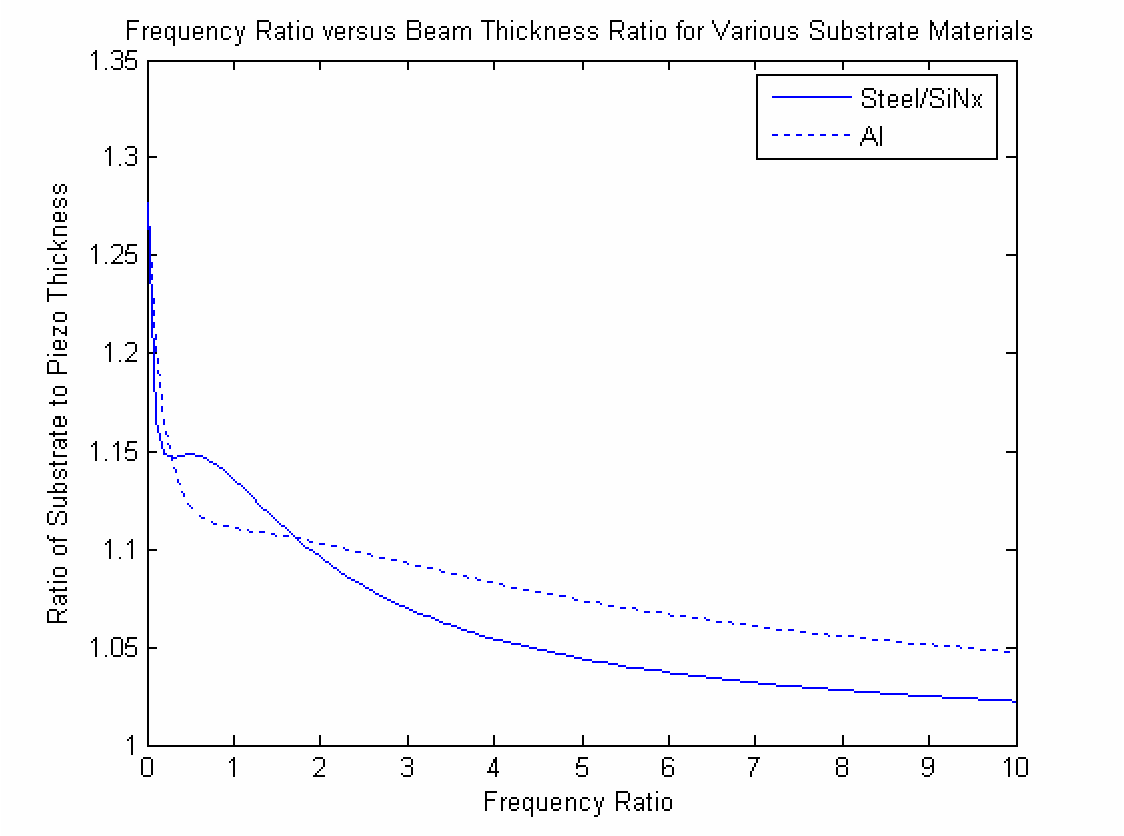

Figure 18. Effect of Varying Substrate Materials

As Figure 18 indicates, the thickness ratio plays an important role in deciding which substrate material offers the most tunability. This can be partially related to how the difference in material moduli affects the centroid and moment of inertia of the beam. The graph clearly displays that for higher thickness ratios, aluminum offers a higher ratio of available tuning, whereas at lower thickness ratios, steel gives better values. As previously mentioned, one must pay attention to the fact that the values are only meaningful at the points where the centroid is located outside of the piezoelectric: for the parameters given previously, and an electrode set at 20% of the substrate height (a realistic scaling for MEMS devices), this occurs at a ratio of less than 1 for steel/SiNx, whereas with Aluminum, a ratio between 1.5 and 2 was necessary. Thus, for this study, the original conclusions remain the same; however, this may not always hold true. Additionally from this analysis, it can be noted that the thickness ratio also plays less of a role in varying the amount of tunability in the Aluminum case, since the material moduli of Aluminum and PZT are closer to each other, and relatively smaller than that of Steel.

Just as the substrate material can have an effect on the available frequency change, the electrode material can as well. Figure 19 plots the frequency ratio versus beam thickness ratio for a gold electrode and a platinum electrode.

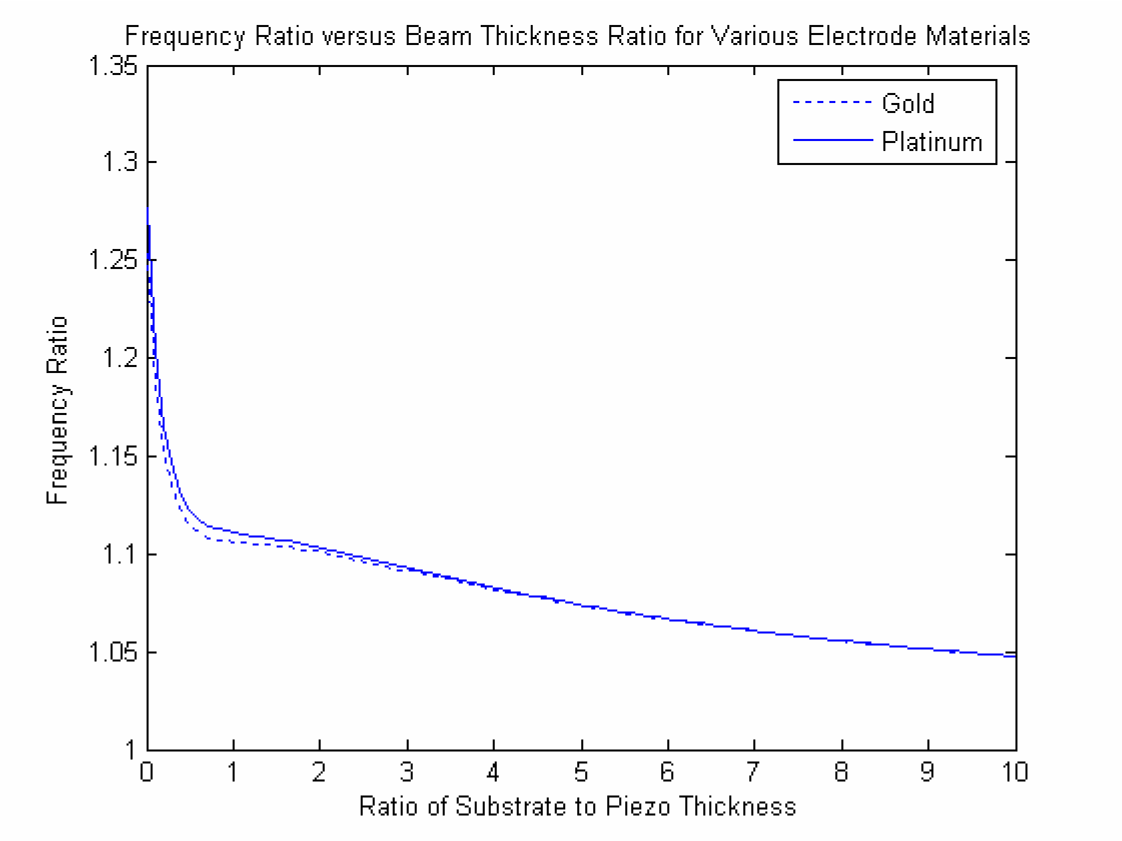

Figure 19. Effect of Varying Electrode Materials

Since the electrode height is usually significantly smaller than the substrate and piezoelectric layers, there is less of a difference in the effective frequency change between materials here than there are in the other material comparisons. As the ratio of substrate to piezoelectric thickness becomes greater, the difference almost diminishes entirely, since the thickness of the electrode becomes increasingly small in relation to the other layers.

From these analyses, the following conclusions can be drawn about resonator parameters as they relate to the range of tunability:

- The d_{33} case results in a wider range of tunability than the d_{31} case for all cases considered.
- A more conservative estimate of the tuning range is achieved by setting the d constant to zero for the piezoelectric layer under the interdigitated electrodes: a more liberal estimate sets the d constant to the d_{31} case. The results are more affected by the assumption at lower numbers of electrodes.
- The smaller the electrode length, the higher the range of tunability for all cases predicted. In reality, a limit on the minimum acceptable electrode length would need to be determined, taking into account the necessary voltage input with respect to electric field depth penetration and minimum achievable feature size.
- Concentrating the electrode spacing so that there is less spacing near the free end and more spacing near the clamped end results in a wider range of tunability.
- The number of electrodes has little effect on the change in frequency, particularly at higher electrode counts. What effect it does have is analogous to the electrode spacing effect and how there is a greater amount of strain at the clamped end of the beam.
- PZT offers the greatest available frequency change of the materials examined, followed by ZnO and finishing with AlN.

- The choice of substrate and electrode material can also affect the range of tunability, although the differences are less when varying the substrate layer than for changes in the piezoelectric layer, and even smaller for changes in the electrode material.

4.3 SAW LOVE-MODE MODEL

4.3.1 Background/Derivation

For this analysis, the surface acoustic wave resonator is modeled as a specific type of SAW resonator called a Love Wave SAW resonator. Love Wave resonators are identifiable by their possession of a guiding overlayer, which has a shear acoustic speed lower than that of the substrate. The effect of this physical setup is that a shear mode wave is set to propagate throughout the length of the resonator when a voltage is applied across the piezoelectric. Love-wave devices are particularly useful for many sensor applications since they have increased sensitivity due to the fact that the acoustic energy is concentrated near the surface, rather than distributed throughout the substrate.

For a regular SAW device without the guiding layer, the nominal frequency (f_o) is a function of the shear velocity (V_s) and electrode spacing λ, which are dependant on the thickness of the piezoelectric layer (t), the shear modulus (μ) and the density (ρ) as given by:

$$f_o = \frac{V_s}{\lambda} = \frac{\sqrt{\frac{\mu}{\rho}}}{2t} \tag{22}$$

When the guiding layer is added, the change in the nominal frequency (Δf) is given as:

$$\Delta f = -f_o * \frac{V_s}{4} \rho_t t_t \left[1 - \left(\frac{V_t}{V_s} \right)^2 \right] [\hat{\mu}]^2_{z=0} \tag{23}$$

where $[\hat{\mu}]^2_{z=0}$ is the particle velocity at the surface of the guiding layer, t is the tuning layer thickness, the subscript s denotes the main piezoelectric layer and the subscript t indicates a property of the guiding layer, in our case, used for tuning (Du, 1998). It should be noted that the change in frequency with the addition of the piezoelectric guiding layer is negative; consequently the frequency of the multi-loaded SAW sensor is lower than the SAW without the extra guiding layer.

As equation 23 shows, the frequency of a Love Mode resonator is dependant on the shear velocities of both of the piezoelectric layers. In turn, these acoustic velocities are functions of the shear moduli of the materials, which can be altered by means of varied shunt capacitor conditions as described in the beginning of the theoretical modeling section. Thus by adding an additional set of interdigitated electrodes to the top of the tuning layer, as shown in Figure 20, the modulus of the guiding layer can be varied to tune the Love Mode resonator frequency.

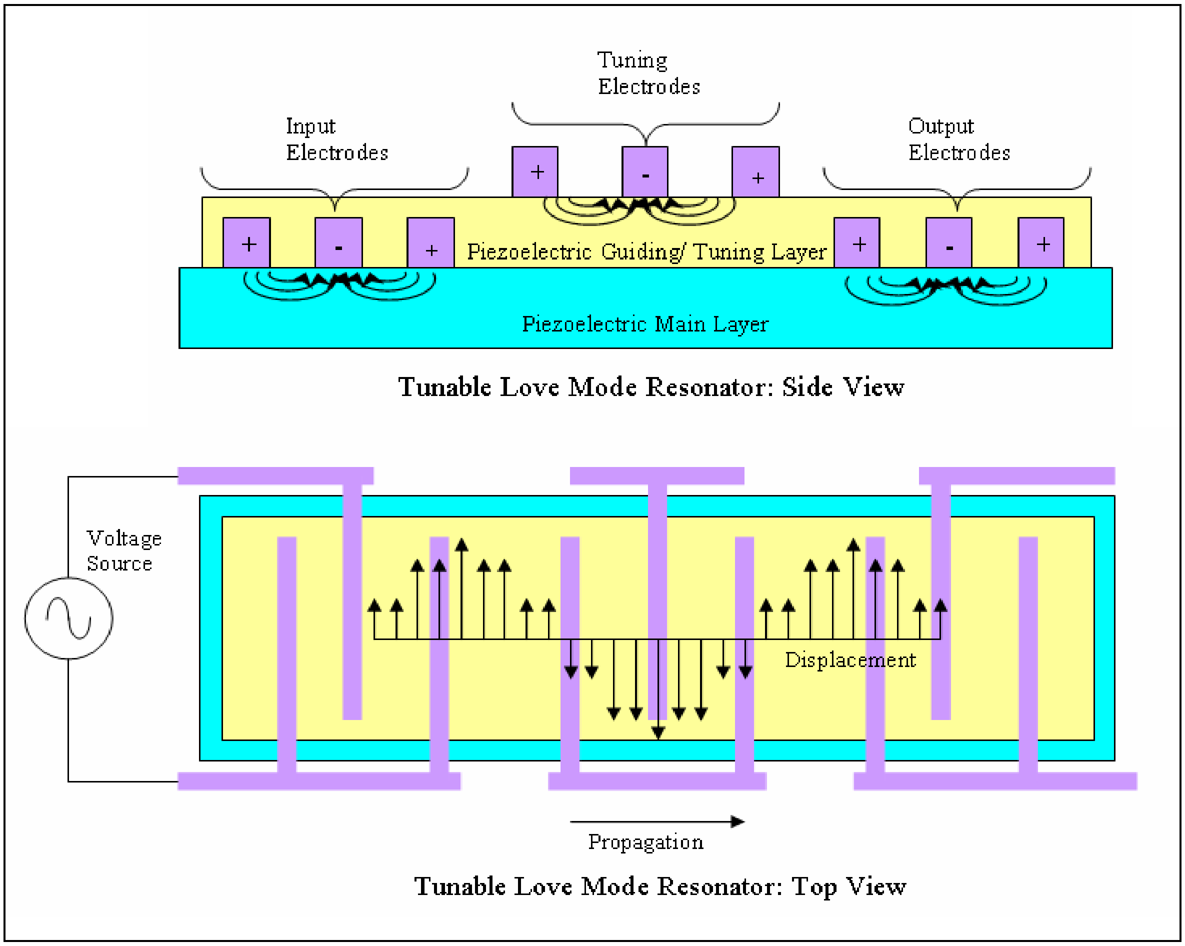

Figure 20. Tunable Love-Mode Resonator

Since the resonator is oscillating in shear, the d_{15} constant should be used to describe the electromechanical coupling effect, and since the d_{15} constant is generally one of the larger piezoelectric coupling constants (for PZT, the d_{15} is equal to 500 pm/V, as opposed to 390 for d_{33} or 190 for d_{31}), a large degree of tunability is possible.

Applying the varied circuit conditions, the closed circuit, open circuit, and shunt capacitor frequencies can be defined as:

$$f_{sc} = \frac{V_s}{\lambda_o} - f_o * \frac{V_s}{4} \rho_t t_t \left[1 - \left(\frac{\sqrt{\frac{\left(\frac{(S^{-1})}{2(1+\upsilon)} \right)}{\rho}}}{V_s} \right)^2 \right] [\hat{\mu}]_{z=0}^2 \tag{24}$$

which is the upper frequency limit,

$$f_{sc} = \frac{V_s}{\lambda_o} - f_o * \frac{V_s}{4} \rho_t t_t \left[1 - \left(\frac{\sqrt{\frac{\left(\frac{(S - (\frac{d^2}{E_3^T}))^{-1}}{2(1+\upsilon)} \right)}{\rho}}}{V_p} \right)^2 \right] [\hat{\mu}]_{z=0}^2 \tag{25}$$

which is the lower frequency limit, and

$$f_{sc} = \frac{V_s}{\lambda_o} - f_o * \frac{V_s}{4} \rho_t t_t \left[1 - \left(\frac{\sqrt{\frac{\left(\frac{(S - (\frac{d^2}{E_3^T}) + Z_{sc})^{-1}}{2(1+\upsilon)} \right)}{\rho}}}{V_p} \right)^2 \right] [\hat{\mu}]_{z=0}^2 \tag{26}$$

respectively. Once again, the shunt capacitor frequency can be altered to any value between the upper and lower limits through use of the appropriate shunt capacitor.

Correspondingly, a ratio of the frequency changes at their open and short circuit conditions can be used to indicate the tunability of the Love Mode resonator:

$$\frac{\Delta f_{sc}}{\Delta f_{oc}} = \frac{\left[1-\left(\frac{\sqrt{\frac{\left(\frac{(S^{-1})}{2(1+\upsilon)}\right)}{\rho}}}{V_p}\right)^2\right]}{\left[1-\left(\frac{\sqrt{\frac{\left(\frac{(S-(\frac{d^2}{E_3^T}))^{-1}}{2(1+\upsilon)}\right)}{\rho}}}{V_p}\right)^2\right]} \qquad (27)$$

4.3.2 Simulation Results

The thin film material properties used in the SAW Love Mode simulations are compiled in Table 3.

Table 3. Material Properties for Beam Layers: SAW Simulations

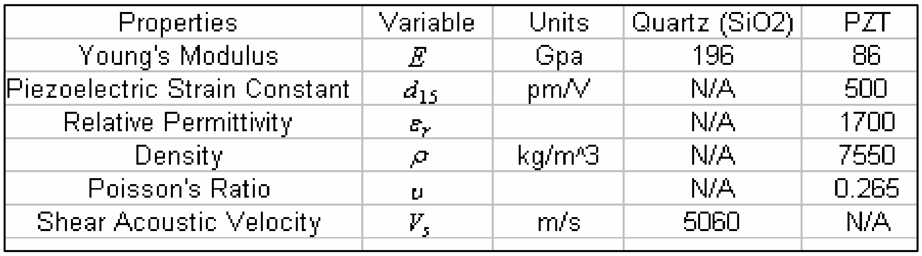

Properties	Variable	Units	Quartz (SiO2)	PZT
Young's Modulus	E	Gpa	196	86
Piezoelectric Strain Constant	d_{15}	pm/V	N/A	500
Relative Permittivity	ε_r		N/A	1700
Density	ρ	kg/m^3	N/A	7550
Poisson's Ratio	υ		N/A	0.265
Shear Acoustic Velocity	V_s	m/s	5060	N/A

Since, in a Love Wave resonator, the shear acoustic velocity of the guiding layer must be lower than that of the substrate, the number of possible materials that are eligible to be the tuning piezoelectric are greatly reduced. In addition, the substrate must also be a piezoelectric, ideally with an acoustic velocity significantly different than that of the guiding layer, and consequently this also places certain restrictions on the material choices. Taking these factors, as well as the availability of modeling parameters for the necessary material constants, into account, SiO_2 was chosen as the substrate material for the simulation of the Love Wave resonator (having a shear acoustic velocity of 5060 m/s) and PZT (having a shear acoustic velocity of 1447 m/s) was used to demonstrate the effects of tunability in the Love Wave Piezoelectric. AlN and ZnO were not used in this analysis for a combination of the reasons previously mentioned.

For these parameters, using Equation 27, the frequency ratio between the open circuit and short circuit conditions was evaluated to be 1.376 (37.6% change), a significantly large amount. It is also valuable to note that this tuning ratio is NOT dependant on the thickness of the layers, a result that distinguishes this study from that done on the bending beams. The change in nominal frequency with the addition of the guiding layer is, however, dependant on the thickness of the layer, as can be seen in Figure 21. The y-axis of Figure 21 plots a change in frequency coefficient for the short circuit case, equal to the delta frequency value calculated using equation 21 without the inclusion of the squared particle velocity term ($[\hat{\mu}]_{z=0}^{2}$).

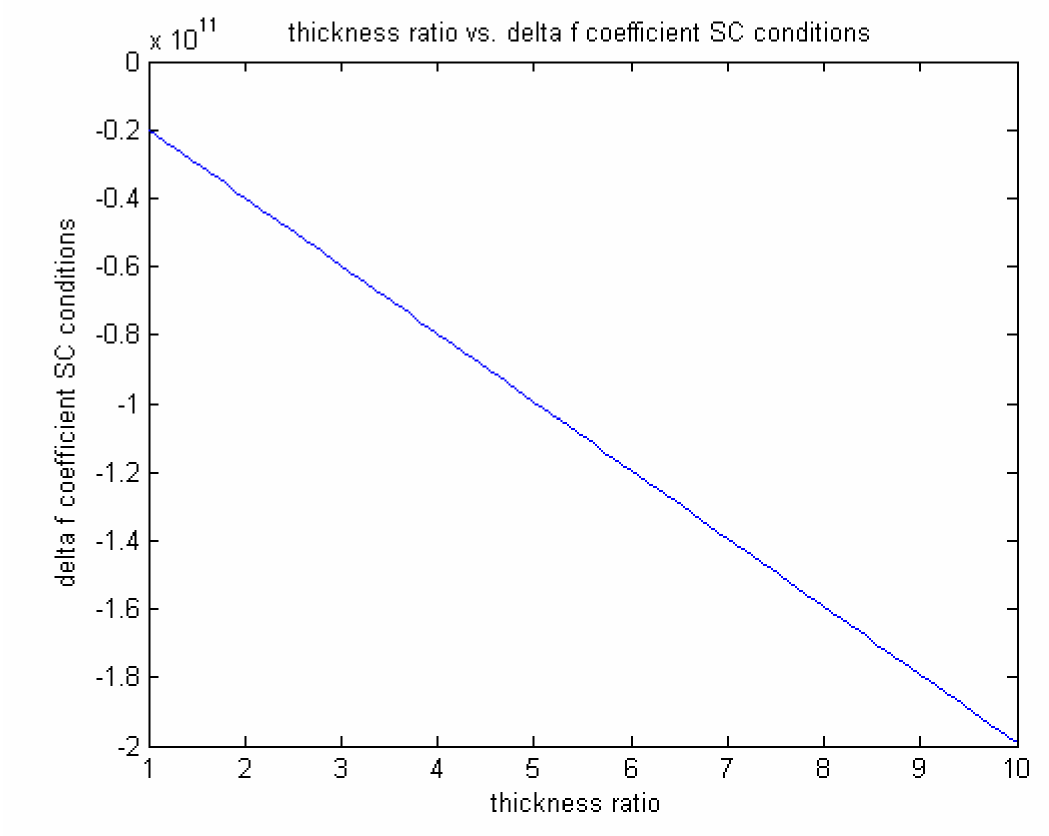

Figure 21. Thickness Ratio Versus Change in Nominal Frequency

As expected, as the thickness of the additional layer increased, the available change in nominal frequency increased as well. Theoretically, since the change in nominal frequency is negative (Equation 23), the frequency would eventually go to zero and wave propagation would cease to exist; however, since the particle velocity at the surface of the guiding layer $[\hat{\mu}]_{z=0}^{2}$ must be solved for experimentally, it is difficult to pinpoint the exact dimensions at which this would occur, or to get a good estimate of the exact changes in frequency with the addition of the guiding layer from a theoretical model.

Through this analysis, the following conclusions can be drawn:

- SAW frequency tunability is achievable in a Love-Mode SAW device: for a structure with a SiO_2 substrate and a PZT guiding layer, the amount of tunability achievable is estimated to be 1.376, or 37.6% change in the frequency.
- The SAW tunability is NOT dependent on the thickness of the guiding layer, a result that distinguishes the study on the Love Mode device from those done on the bending beam configuration.
- The nominal resonant frequency with the addition of the guiding layer IS dependant on the thickness of the guiding layer: as the thickness of this layer increases, the frequency of the resonator decreases.

4.4 FBAR MODEL

4.4.1 Background/Derivation

For this model, a detailed frequency equation for a film bulk acoustic resonator (FBAR), accounting for three electrode layers and two device layers (in our case, an active piezoelectric layer and a tuning piezoelectric layer) has been derived, based on previous works by Chen and Zhang (Chen, 2006 and Zhang, 2003).

The matrix model used to describe a 5-layer FBAR is shown in Figure 22.

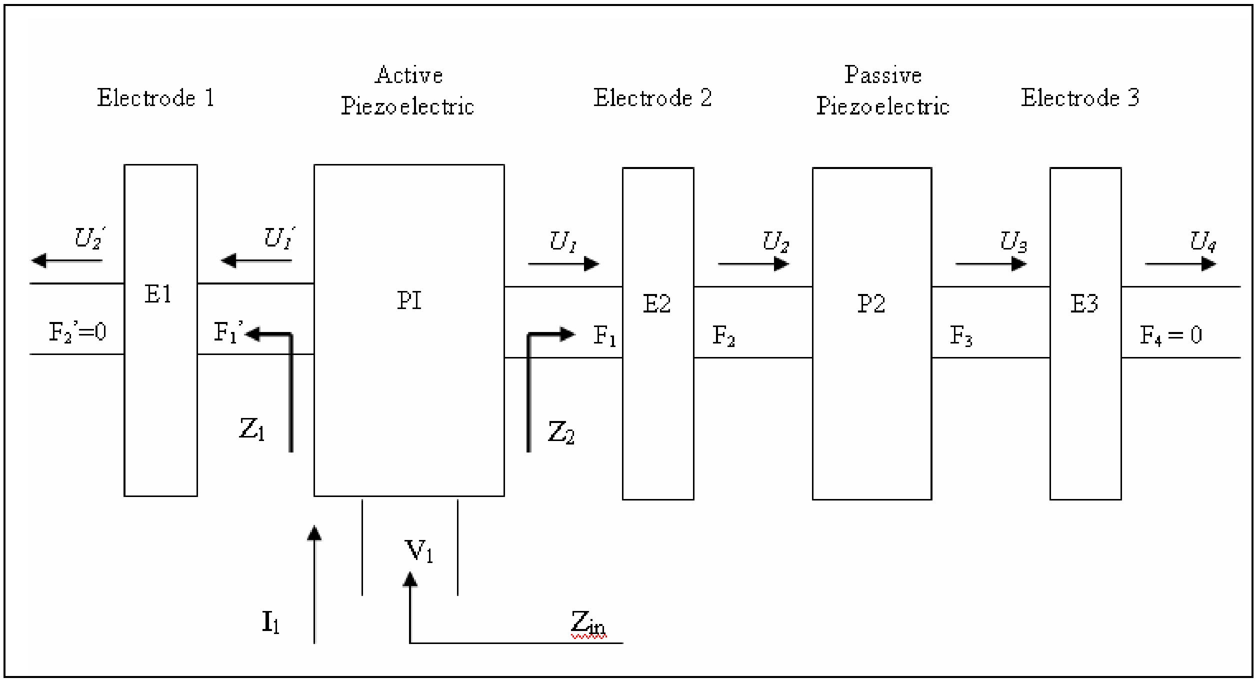

Figure 22. Matrix Model for Film Bulk Acoustic Resonator

The transfer matrix relationship for the top electrode is given as:

$$\begin{bmatrix} F_1' \\ u_1' \end{bmatrix} = \begin{bmatrix} \cos\gamma_{e1} & jZ_{e1}\sin\gamma_{e1} \\ j\sin y_{e1}/Z_{e1} & \cos\gamma_{e1} \end{bmatrix} * \begin{bmatrix} F_2' \\ u_2' \end{bmatrix} \tag{28}$$

where F and u represent force and displacement velocity, $Z = S\rho V$ is the acoustic impedance (S, ρ, and V are the surface area, density, and acoustic velocity, respectively), and $\gamma = \omega l / V$ is the phase delay in the top electrode ($w = 2\pi f$ is the angular frequency, with f being the resonant frequency, and l is the length). The subscript $e1$ denotes a property of the first electrode, and other scripts indicate placement, as indicated in Figure 22.

Since the left surface of the first electrode is free, $F_2^{'}$ = 0, thus making the acoustic impedance of the first electrode, presented at the left side of the first (active) piezoelectric layer in Figure 22 equal to:

$$Z_1^{'} = \frac{F_o}{u_o} = jZ_{e1} \tan\gamma_{e1} \tag{29}$$

Similarly, for the second (middle) electrode, the passive (tuning) piezoelectric layer, and the third (right) electrode, the transfer matrices are equal to:

$$\begin{bmatrix} F_1 \\ u_1 \end{bmatrix} = \begin{bmatrix} \cos\gamma_{e2} & jZ_{e2}\sin\gamma_{e2} \\ j\sin y_{e2} / Z_{e2} & \cos\gamma_{e2} \end{bmatrix} * \begin{bmatrix} F_2 \\ u_2 \end{bmatrix} \tag{30}$$

$$\begin{bmatrix} F_2 \\ u_2 \end{bmatrix} = \begin{bmatrix} \cos\gamma_{p2} & jZ_{p2}\sin\gamma_{p2} \\ j\sin y_{p2} / Z_{p2} & \cos\gamma_{p2} \end{bmatrix} * \begin{bmatrix} F_3 \\ u_3 \end{bmatrix} \tag{31}$$

and

$$\begin{bmatrix} F_3 \\ u_3 \end{bmatrix} = \begin{bmatrix} \cos\gamma_{e3} & jZ_{e3}\sin\gamma_{e3} \\ j\sin y_{e3} / Z_{e3} & \cos\gamma_{e3} \end{bmatrix} * \begin{bmatrix} F_4 \\ u_4 \end{bmatrix} \tag{32}$$

where the subscripts $e2$, $p2$, and $p3$ signify the second electrode, tuning piezoelectric, and third electrode, respectively. These matrices can be combined to give:

$$\begin{bmatrix} F_1 \\ u_1 \end{bmatrix} = \begin{bmatrix} \cos\gamma_{e2} & jZ_{e2}\sin\gamma_{e2} \\ j\sin y_{e2}/Z_{e2} & \cos\gamma_{e2} \end{bmatrix} * \begin{bmatrix} \cos\gamma_{p2} & jZ_{p2}\sin\gamma_{p2} \\ j\sin y_{p2}/Z_{p2} & \cos\gamma_{p2} \end{bmatrix} * \begin{bmatrix} \cos\gamma_{e3} & jZ_{e3}\sin\gamma_{e3} \\ j\sin y_{e3}/Z_{e3} & \cos\gamma_{e3} \end{bmatrix} * \begin{bmatrix} F_4 \\ u_4 \end{bmatrix} \tag{33}$$

Assuming the right side of the second piezoelectric to be free, F_4=0. Solving for the acoustic impedance of the middle electrode, tuning piezoelectric, and right electrode, presented at the right side of the first (active) piezoelectric layer, we find:

$$Z_1 = \frac{F_1}{u_1} = \frac{j(Z_{e3}\tan\gamma_{e3} + z_{p2}\tan\gamma_{p2} + z_{e2}\tan\gamma_{e2} + \frac{z_{e2}z_{e3}}{Z_{p2}}\tan\gamma_{e3}\tan\gamma_{p2}\tan\gamma_{e2})}{1 - \left(\left(\frac{z_{e3}}{z_{e2}}\right)(\tan y_{e2}\tan\gamma_{e3}) + \left(\frac{z_{e3}}{z_{p2}}\right)(\tan\gamma_{p2}\tan\gamma_{e3}) + \left(\frac{Z_{p2}}{Z_{e2}}\right)(\tan\gamma_{e2})(\tan\gamma_{p2})\right)} \tag{34}$$

In a similar fashion, if the left electrode port of the active piezoelectric layer is considered as the acoustic backing port terminated with acoustic impedance, $Z_1^{'}$, then electrical variables V_1 and I_1 can be calculated as:

$$\begin{bmatrix} V_1 \\ I_1 \end{bmatrix} = [A] * \begin{bmatrix} F_1 \\ u_1 \end{bmatrix} \tag{35}$$

where

$$[A] = \frac{1}{\phi H_A} \begin{bmatrix} 1 & J\phi^2 / \omega C_{01} \\ j\omega C_{01} & 0 \end{bmatrix} * [A^{'}] \tag{36}$$

with

$$H_A = \cos\gamma - 1 + jz_1^{'} \sin\gamma \tag{37}$$

and

$$\left[A^{'}\right] = \begin{bmatrix} \cos\gamma + jz_1^{'}\sin\gamma & Z_o(z_1^{'}\cos\gamma + j\sin\gamma) \\ j\sin\gamma / Z_o & 2(\cos\gamma - 1) + jz_1^{'}\sin\gamma \end{bmatrix} \tag{38}$$

where $z_1^{'} = Z_1^{'} / Z_o$ is $Z_1^{'}$ (Equation 29) normalized with respect to the impedance of the active piezoelectric layer, C_{01} is the clamped capacitance active piezoelectric layer, and $\phi = \sqrt{k_t^2 C_{01} ZV / l}$ is the transformer ratio in the Mason's equivalent circuit for the active piezoelectric layer (where k_t^2 is the electromechanical coupling coefficient for thickness extensional mode).

Solving these equations, the electrical input impedance for the composite resonator can be expressed as:

$$Z_{in} = \frac{V}{I} = \frac{1}{j\omega C_o}\left[1 - \frac{k_t^2(z_1 + z_1^{'})\sin\gamma + j2(1-\cos\gamma)}{\gamma(z_1 + z_1^{'})\cos\gamma + j(1 + z_1 z_1^{'})\sin\gamma}\right] \tag{39}$$

where $z_1 = Z_1 / Z_o$ is Z_1(Equation 34) normalized with respect to the impedance of the active piezoelectric layer.

According to the IEEE standard for piezoelectric materials (IEEE, 1987), the parallel resonant frequencies will correspond to the maximum resistance values of the resonator, which are the real parts of Z_{in} at infinite impedance ($Z_{in} \to \infty$). To find these values, we set the denominator of Equation 39 equal to zero to get an equation for the parallel resonant frequencies, given as:

$$(z_1 + z_2)\cos\gamma + j(1 + z_1 z_2)\sin\gamma = 0 \tag{40}$$

For the resonator, the normal regions correspond to the areas in which γ is close to an integer multiple of pi; thus, for the first normal region, the $m_N + 1$ order resonant frequency will correspond to:

$$\gamma \approx \pi\,;\ \gamma_{p2} \approx m_N \pi \tag{41}$$

where m_N is the mode order of the tuning piezoelectric resonator at the center of the first normal region. This gives the approximations:

$$\tan\gamma \approx \gamma - \pi\,;\ \tan\gamma_{p2} \approx \gamma_{p2} - m_N \pi \tag{42}$$

Because the electrodes are usually much thinner than the piezoelectric film, $\gamma_{e1} << 1$ and $\gamma_{e2} << 1$ in this region, giving:

$$\tan\gamma_{e1} \approx \gamma_{e1}\,;\ \tan\gamma_{e2} \approx y_{e2} \tag{43}$$

As a result,

$$z_1^{'} \approx j\frac{Z_{e1}}{Z_0}\gamma_{e1} = jz_{e1}y_{e1} \tag{44}$$

and

$$z_1 \approx \frac{j(Z_{e3}\gamma_{e3} + z_{p2}(\gamma_{p2} - m_n\pi) + z_{e2}\gamma_{e2} + \frac{z_{e2}z_{e3}}{Z_{p2}}\gamma_{e3}\gamma_{e2}(y_{p2} - m_n\pi)}{1 - \left(\left(\frac{z_{e3}}{z_{e2}} \right) \left(y_{e2}\gamma_{e3} \right) + \left(\frac{z_{e3}}{z_{p2}} \right) (\gamma_{e3})(\gamma_{p2} - m_n\pi) + \left(\frac{Z_{p2}}{Z_{e2}} \right) (\gamma_{e2})(\gamma_{p2} - m_n\pi) \right)}$$

$$\approx j(Z_{e3}\gamma_{e3} + z_{p2}(\gamma_{p2} - m_n\pi) + z_{e2}\gamma_{e2} + \frac{z_{e2}z_{e3}}{Z_{p2}}\gamma_{e3}\gamma_{e2}(y_{p2} - m_n\pi) \qquad (45)$$

Substitution of approximations (Equations 41-45) into (Equation 40), gives:

$$\begin{aligned}
& jz_{e1}\gamma_{e1} + j(Z_{e3}\gamma_{e3} + z_{e2}\gamma_{e2} + z_{p2}(\gamma_{p2} - m_n\pi) + \frac{z_{e2}z_{e3}}{Z_{p2}}\gamma_{e3}\gamma_{e2}(\gamma_{p2} - m_N\pi)) \\
& + \left\{ 1 + (jz_{e1}\gamma_{e1}) \left(j(Z_{e3}\gamma_{e3} + z_{e2}\gamma_{e2} + z_{p2}(\gamma_{p2} - m_n\pi) + \frac{z_{e2}z_{e3}}{Z_{p2}}\gamma_{e3}\gamma_{e2}(\gamma_{p2} - m_N\pi)) \right) \right\} \left(y - \pi \right) \\
& = jz_{e1}\frac{2\pi f l_{e1}}{V_{e1}} + j(Z_{e3}\frac{2\pi f l_{e3}}{V_{e3}} + z_{e2}\frac{2\pi f l_{e2}}{V_{e2}} + z_{p2}(\frac{2\pi f l_{p2}}{V_{p2}} - m_n\pi) + \frac{z_{e2}z_{e3}}{Z_{p2}}\frac{2\pi f l_{e2}}{V_{e2}}\frac{2\pi f l_{e3}}{V_{e3}}(\frac{2\pi f l_{p2}}{V_{p2}} - m_N\pi)) \\
& + \left\{ 1 + (jz_{e1}\frac{2\pi f l_{e1}}{V_{e1}}) \left(j(Z_{e3}\frac{2\pi f l_{e3}}{V_{e3}} + z_{e2}\frac{2\pi f l_{e2}}{V_{e2}} + z_{p2}(\frac{2\pi f l_{p2}}{V_{p2}} - m_n\pi) + \frac{z_{e2}z_{e3}}{Z_{p2}}\frac{2\pi f l_{e3}}{V_{e3}}\frac{2\pi f l_{e2}}{V_{e2}}(\frac{2\pi f l_{p2}}{V_{p2}} - m_N\pi)) \right) \right\} \\
& * \left(\frac{2\pi f l}{V} - \pi \right) = 0
\end{aligned}$$

$$(46)$$

Utilizing the aforementioned assumptions, it can be recognized that

$\frac{z_{e2}z_{e3}}{Z_{p2}}\gamma_{e3}\gamma_{e2}(\gamma_{p2} - m_N\pi)$ and

$$(jz_{e1}\frac{2\pi f l_{e1}}{V_{e1}}) \left(\begin{array}{l} j(Z_{e3}\frac{2\pi f l_{e3}}{V_{e3}} + z_{e2}\frac{2\pi f l_{e2}}{V_{e2}} + z_{p2}(\frac{2\pi f l_{p2}}{V_{p2}} - m_n\pi) + \\ \frac{z_{e2}z_{e3}}{Z_{p2}}\frac{2\pi f l_{e3}}{V_{e3}}\frac{2\pi f l_{e2}}{V_{e2}}(\frac{2\pi f l_{p2}}{V_{p2}} - m_N\pi)) \end{array} \right)$$

are significantly small, higher-order terms that can be omitted from the relationship. Thus Equation 46 becomes:

$$f_p(m_N+1)=\frac{(m_N Z_{p2}+1)}{2(\frac{z_{e1}l_{e1}}{V_{e1}}+\frac{z_{e2}l_{e2}}{V_{e2}}+\frac{z_{e3}l_{e3}}{V_{e3}}+\frac{z_{p2}l_{p2}}{V_{p2}}+\frac{l}{V})} \tag{47}$$

which is a linear expression for the (m_n+1) frequency of the resonator.

It can be seen that the resonant frequency given in Equation 47 is dependant on the acoustic impedance of the passive layer, which in turn is a function of the acoustic velocity. Furthermore, since the two parameters which influence the acoustic velocity are the material's density and modulus, it becomes apparent that altering the modulus of the material, as described in the general tuning circuit conditions section of this work, will result in modifications of the natural frequency. Accordingly, the lower frequency limit becomes equal to:

$$\begin{aligned} f_{p_{sc}}(m_n Z_{p_{sc}}+1) &= \frac{m_n z_{p2_{sc}}+1}{2(\frac{z_{e1}l_{e1}}{V_{e1}}+\frac{z_{p2}l_{p2}}{V_{p2}}+\frac{z_{e2}l_{e2}}{V_{e2}}+\frac{z_{e3}l_{e3}}{V_{e3}}+\frac{l}{V})} = \\ &\frac{m_n(S\rho\sqrt{\frac{(S^E)^{-1}}{\rho}})+1}{2(\frac{z_{e1}l_{e1}}{V_{e1}}+\frac{z_{p2}l_{p2}}{V_{p2}}+\frac{z_{e2}l_{e2}}{V_{e2}}+\frac{z_{e3}l_{e3}}{V_{e3}}+\frac{l}{V})} \end{aligned} \tag{48}$$

and the upper frequency limit becomes equal to:

$$f_{p_{oc}}(m_n Z_{p_{oc}}+1)=\frac{m_n z_{p2_{oc}}+1}{2(\frac{z_{e1}l_{e1}}{V_{e1}}+\frac{z_{p2}l_{p2}}{V_{p2}}+\frac{z_{e2}l_{e2}}{V_{e2}}+\frac{z_{e3}l_{e3}}{V_{e3}}+\frac{l}{V})}=$$

$$\frac{m_n(S\rho\sqrt{\frac{(S^E-\frac{d^2}{\varepsilon_p})^{-1}}{\rho}})+1}{2(\frac{z_{e1}l_{e1}}{V_{e1}}+\frac{z_{p2}l_{p2}}{V_{p2}}+\frac{z_{e2}l_{e2}}{V_{e2}}+\frac{z_{e3}l_{e3}}{V_{e3}}+\frac{l}{V})} \tag{49}$$

In the intermediate case, with impedance Z_{sh} for the shunt capacitor, the frequency can be equated to:

$$f_{p_{sh}}(m_n Z_{p_{sh}}+1)=\frac{m_n z_{p2_{sh}}+1}{2(\frac{z_{e1}l_{e1}}{V_{e1}}+\frac{z_{p2}l_{p2}}{V_{p2}}+\frac{z_{e2}l_{e2}}{V_{e2}}+\frac{z_{e3}l_{e3}}{V_{e3}}+\frac{l}{V})}=$$

$$\frac{m_n(S\rho\sqrt{\frac{(S^E-\frac{d^2}{\varepsilon_p}+Z_{sh})^{-1}}{\rho}})+1}{2(\frac{z_{e1}l_{e1}}{V_{e1}}+\frac{z_{p2}l_{p2}}{V_{p2}}+\frac{z_{e2}l_{e2}}{V_{e2}}+\frac{z_{e3}l_{e3}}{V_{e3}}+\frac{l}{V})} \tag{50}$$

Assuming all other variables (thickness, surface area, density, etc.) are constant between the open circuit and short circuit conditions, a frequency ratio, equal to the open circuit stiffness divided by the short circuit stiffness, can be used as a measure of the degree of tunability of the FBAR:

$$\frac{f_{p_{oc}}}{f_{p_{sc}}}=\frac{m_n(S\rho\sqrt{\frac{(S^E-\frac{d^2}{\varepsilon_p})^{-1}}{\rho}})+1}{m_n(S\rho\sqrt{\frac{(S^E)^{-1}}{\rho}})+1} \tag{51}$$

4.4.2 Simulation Results

The estimated properties used in the simulations for the piezoelectric materials are given in Table 4.

Table 4. Material Properties for Beam Layers: FBAR Simulations

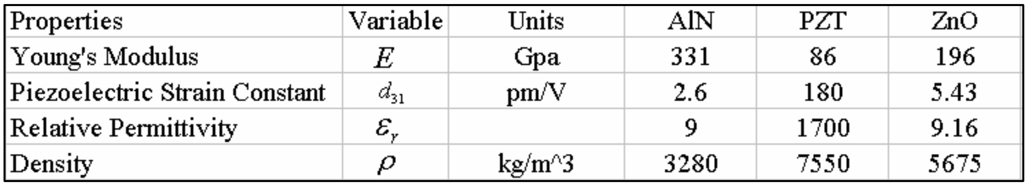

Properties	Variable	Units	AlN	PZT	ZnO
Young's Modulus	E	Gpa	331	86	196
Piezoelectric Strain Constant	d_{31}	pm/V	2.6	180	5.43
Relative Permittivity	ε_r		9	1700	9.16
Density	ρ	kg/m^3	3280	7550	5675

Since, in the FBAR configuration, the applied stress and poling directions are perpendicular, the d_{31} response of the piezoelectric is elicited; thus the d_{31} piezoelectric strain constant is used as the variable relating the electromechanical coupling in the device.

Table 5 gives the values of the frequency ratios for each of the three materials, as calculated by Equation 51.

Table 5. Frequency Ratios for FBAR Simulations on Various Piezoelectrics

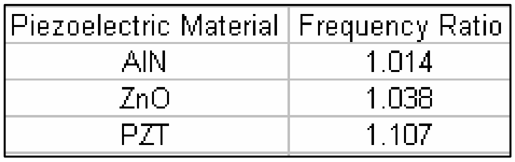

Piezoelectric Material	Frequency Ratio
AlN	1.014
ZnO	1.038
PZT	1.107

The fact that all values are greater than 1 coincides with Equations 48 and 49 that show the open circuit frequency is greater than the short circuit frequency for each of the piezoelectric materials. The magnitude of that difference represents the tunability of the FBAR. The most significant change is accomplished using Lead Zirconate Titanate, or PZT, a logical result since

PZT has the highest electromechanical coupling of the three materials investigated. PZT's frequency ratio of greater than 1.1 signifies that the resonant frequency of the FBAR can be tuned by more than 10%. Although the other materials have smaller frequency ratios (approximately 1.038 (3.8% change) for Zinc Oxide and 1.014 (1.4% change) for Aluminum Nitride), it is necessary to perceive that these are still substantial potentials for tunability of devices, particularly since the FBARs are operating in the gigahertz range. Other important parameters such as the quality factors, acoustic velocities, and processing issues could be considered in selecting the material, and might make these other materials more desirable for some applications. It should be noted that there is also the potential for using different piezoelectric materials in the active and tuning layers of the FBAR. In this configuration, it would be possible to take advantage of multiple benefits (ex. use AlN as the active layer for its high quality factor and high acoustic velocity and PZT as the tuning layer to achieve the largest range of frequency tunability).

Arguably the most important parameter in designing an FBAR is that of the resonant frequency. Thus, it is important to note that both the open circuit and short circuit frequencies are dependant on the thickness of the additional piezoelectric tuning layer, and as a result, this layer should be taken into account when designing the device. This idea is demonstrated in Figure 23 for PZT FBARs, showing both the open circuit and short circuit frequencies plotted against a thickness ratio, which is a ratio of the thickness of the active layer of piezoelectric to that of the tuning layer of piezoelectric.

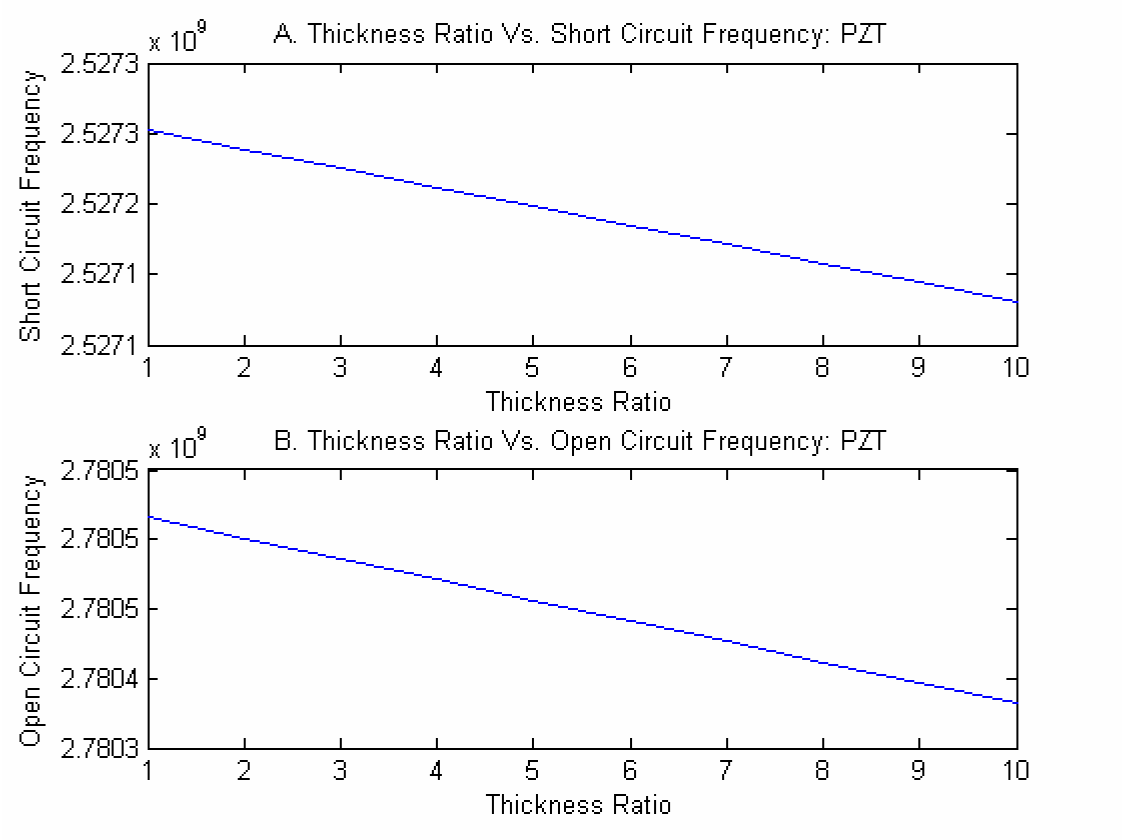

Figure 23. Thickness Ratio Versus Frequency for PZT FBARs

Additionally, the piezoelectric material chosen has a similar affect on the frequencies encountered, and this result is demonstrated in Figure 24: the higher the acoustic velocity of the material, the higher the resonant frequency of the FBAR.

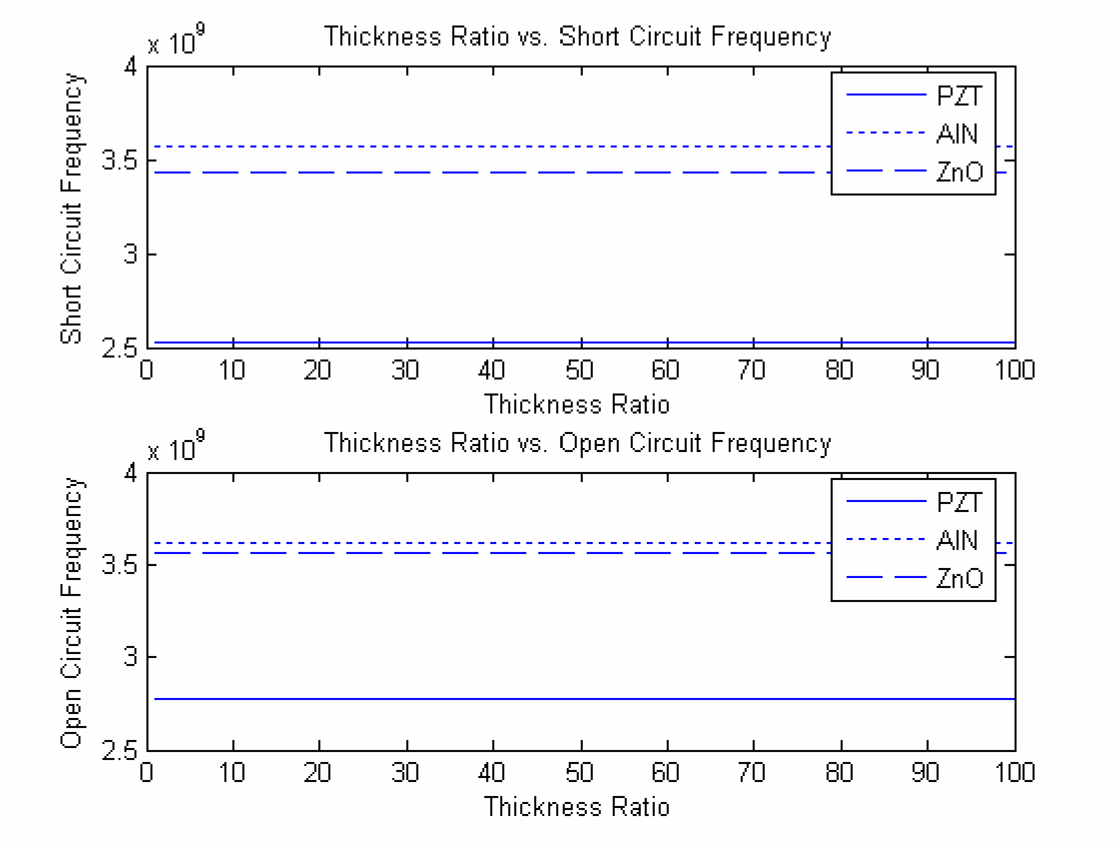

Figure 24. Thickness Ratio Versus Frequency Three Different Piezoelectric FBAR Materials

Although no slope can be seen for the graphs in Figure 24, Figure 23 shows that there is a frequency dependence that is a function of the thickness of the additional piezoelectric layer: however, Figure 24 demonstrates that the piezoelectric material chosen has a much larger impact on the operating frequencies relative to the thickness of the layers. Consequently, the best approach for design would likely be to choose the material for the active layer of the FBAR to be closest to the desired operating frequency of the device, while still accounting for the tuning piezoelectric in the frequency calculation to fine tune the frequency prediction of the design as much as possible.

Finally, attention should be drawn to the fact that although the frequencies themselves are dependant on the thickness of the layers, the frequency *ratio* for an FBAR, which is the measure of tunability, is independent of the thickness of the piezoelectric tuning layer, as is evidenced by Equation 51. This result distinguishes the findings of the FBAR application from prior studies on bending cantilever beams utilizing the same tuning concept, but is consistent with the Love-mode SAW simulations, another acoustic-mode device. This result would be another important deduction to consider in the design of a tunable FBAR.

From these analyses, the following conclusions were made:

- FBAR tunability is achievable; the amount of tunability is NOT dependant on the thickness of the additional layer, but is dependant on the piezoelectric material.
- The largest amount of tunability is possible for a PZT device, followed by ZnO and finishing with Aluminum Nitride.
- The resonant frequency of the device is a function of the thickness of the additional piezoelectric layer: the thicker the layer, the lower the frequency.
- The device material has a larger impact on the resonant frequency than the thickness of the additional layer.
- The higher the acoustic velocity of the device, the higher the resonant frequency.

5.0 PROCESSING OF PZT INTERDIGIATED TUNABLE RESONATORS

The following fabrication steps were investigated to develop a successful process flow capable of fabricating tunable piezoelectric resonators, most specifically, PZT interdigitated, bending devices. Both successful and unsuccessful processing is documented to reason through the methodology behind the fabrication choices that led to the development of the final process plans established.

5.1 PROCESSING OF THIN FILM PZT

5.1.1 Sputtered PZT Film

In the first stage of fabrication investigation for this project, the sputtering method of piezoelectric material deposition was employed. Although the spin-coating method was recognized for having significant advantages, as described in the background on piezoelectric thin films, the availability of the sputtering processing equipment proved as incentive to begin the investigations on this technique. A RF-magnetron sputtering system, manufactured by Kurt J. Lesker Company, was used for the deposition. Process recipes from Abe and Reed were employed, as detailed in (Abe, 1994). The major process parameters from Abe and Reed are given in Table 6. Both rapid thermal annealing (done in an AG Associates Heatpulse 210 RTA system in flowing O_2 for 5s) and conventional furnace annealing (in a F48055 Benchtop Muffle furnace in air for 1 hr) were used on the sputtered films.

Table 6. Sputtering Parameters Used in Deposition, Given by Abe and Reed

Sputtering Parameter	Value
Sputtering Gas	Ar (83%) + O2 (17%)
Pressure	5 mTorr
RF Power	100 W
Target Diameter	5.08 Cm
Base Pressure	2*10^-7
Target to Substrate Separation	6.7 cm
Target Voltage	230 V
Sputtering Rate	1.2 A/sec at 400C

Several problems were encountered in the sputtering process, particularly with respect to reaching the desired deposition temperature of 400C. The sputtering chamber was heated and controlled using a heating lamp connected to a thermocouple and controller. The thermocouple was attached to the wafer backside via high temperature cement. The highest temperature that was able to be measured was 230 C, and the source of the variation was not able to be determined. Hypotheses for the discrepancy include a problem with the heating lamp or strong insulation of the cement. Large particle contamination in the chamber, due to the long sputtering deposition time, was also found to be a problem.

Post-deposition, large differences in surface thickness were found across the wafers. Figure 25 shows both a macroscopic view (Figure A) and several microscopic views (Figure B.) of the wafer surface (microscopic pictures taken using the Nikon Eclipse L150 Microscope).

The large differences in the colors, which take place over a very small area of the wafer, give an indication of the large variation in film thickness. Evidence supporting this presumption was found by applying vacuum tape to the substrate prior to deposition and then measuring the respective thicknesses using the Detek surface profilometer. Thicknesses measured were also significantly less than the expected values, based on the 1.2A/second estimated deposition rate, a finding which could be a result of an inability to reach the desired deposition temperature.

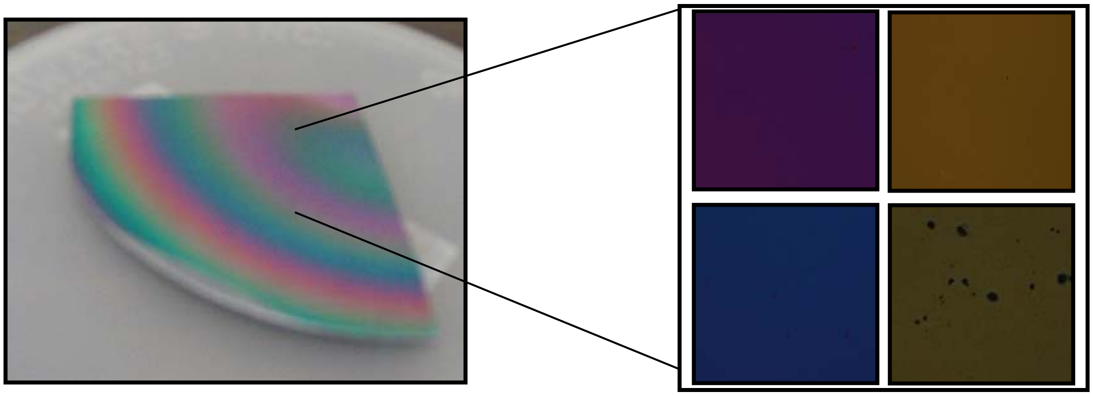
Figure A: Macroscopic View Figure B: Microscopic Views

Figure 25.-Sputtered PZT Prior to Annealing

Furthermore, even prior to annealing, the beginning of crack propagation could be seen at certain locations in the wafer surface (Figure 26).

Figure 26. Close Up: Microscopic View of Sputtered PZT Prior to Annealing

These cracks proved to progress further throughout the wafer after the annealing process (using both the Rapid Thermal Annealer (RTA) and the conventional furnace heating methods), making the films increasingly undesirable for use in fabricating micro-scale devices. Post annealing microscope pictures are given in Figure 27. The significant crack propagation may also be due to the inability to reach a higher deposition temperature, as there have been some prior research investigations suggesting that it is necessary to raise substrate temperatures to at least 250C in order to prevent microcracking (Sreenivas, 1989). Target degradation, deterioration in the quality of the piezoelectric material of the PZT sputtering target, is another possibility for the poor quality of the film, as the available target used for these trials was significantly old.

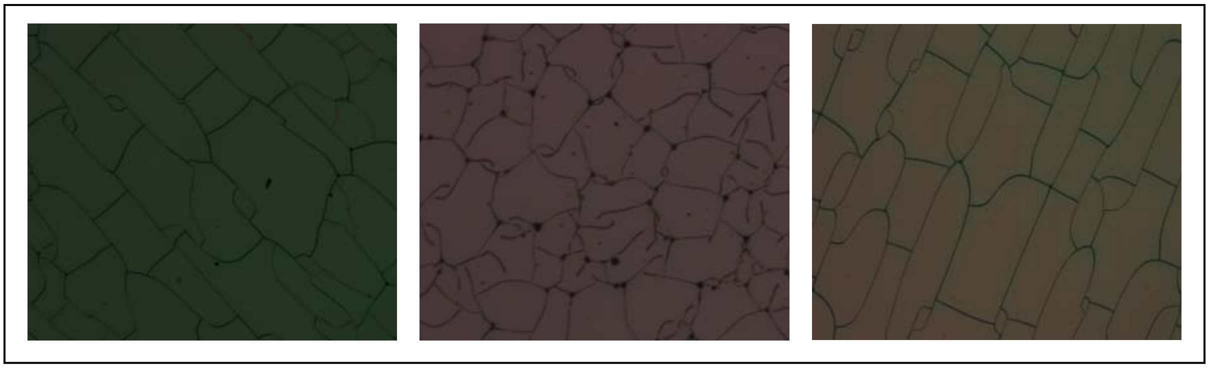

Figure 27. Microscopic View of Sputtered PZT After Annealing

5.1.2 Sol Gel PZT Film

After these initial attempts at PZT sputtering resulted in some negative findings, the investigation turned to sol-gel PZT fabrication. The sol-gel deposition process outlined by Jeon (Jeon, 2005) became the outline for thin film fabrication.

This process was slightly altered by Massachusetts Institute of Technology (MIT) researcher Wonjae Choi in order to achieve more reliable results, and the corresponding sol-gel spin coat/ pyrolysis/ annealing steps used are outlined in Figure 28. These parameters also served as the first set of process values used for the first trial of sol-gel deposition of this research project, done at MIT.

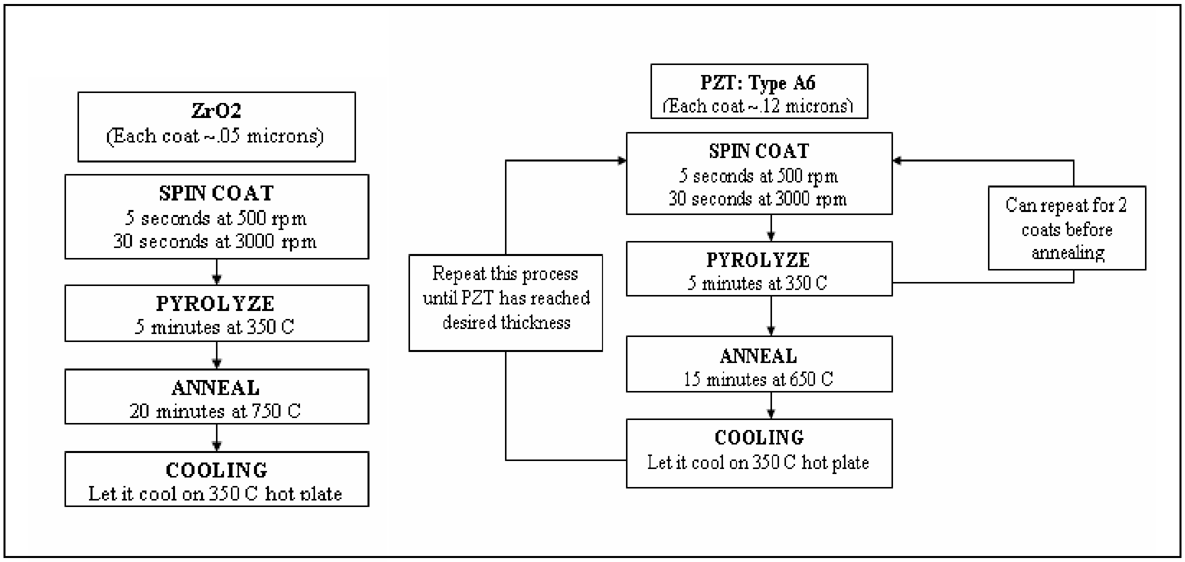

Figure 28. MIT Researcher's (Wonjae Choi) Process Plan for Sol Gel PZT Thin Films

MIT piezoelectric films were fabricated on Si/SiNx/SiO_2 substrates. The SiNx and SiO_2 layers were manufactured via LPCVD (low pressure chemical vapor deposition) and were chosen so as to minimize the curvature in the beams by matching the compressive and tensile stresses between layers. In addition, the SiO_2 layer served as an adhesion layer for the ZrO_2, and the SiNx layer provided a membrane layer for structural support of the piezoelectric cantilever. The sol-gel layer of ZrO_2 applied to the substrate prior to the PZT deposition provided a barrier layer for preventing electrical charge diffusion from the piezoelectric layer, as well as allowed for a means of adhesion between the SiO_2 and the PZT layers. Both the ZrO_2 and PZT sol-gel solutions used in this study were pre-prepared and were purchased from Mitsubishi Materials Inc. All annealing steps were done in an environment of flowing N_2 for each trial of sol gel processing.

Figure 29 shows some initial results of PZT films prepared at MIT using this process.

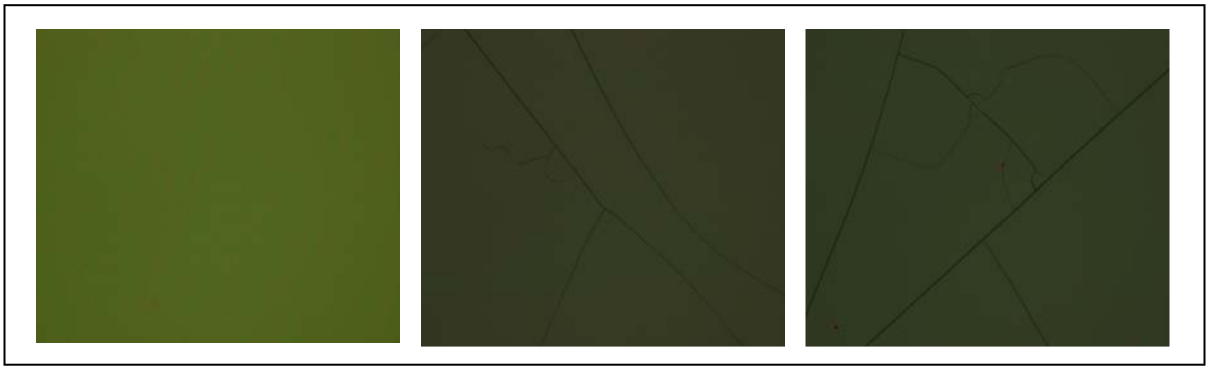

Figure 29. Microscope Images of MIT Sol-Gel Films

It can be seen that these films show some degree of microcracks; however, there were also large portions of the film that remained crack free, suggesting the ability for successful fabrication of microdevices.

The first rounds of ZrO_2/PZT films processed at University of Pittsburgh were mistakenly done on Si/SiO_2/SiNx rather than Si/SiNx/SiO_2 substrates. Figure 30 shows some pictures of the resulting piezoelectric films.

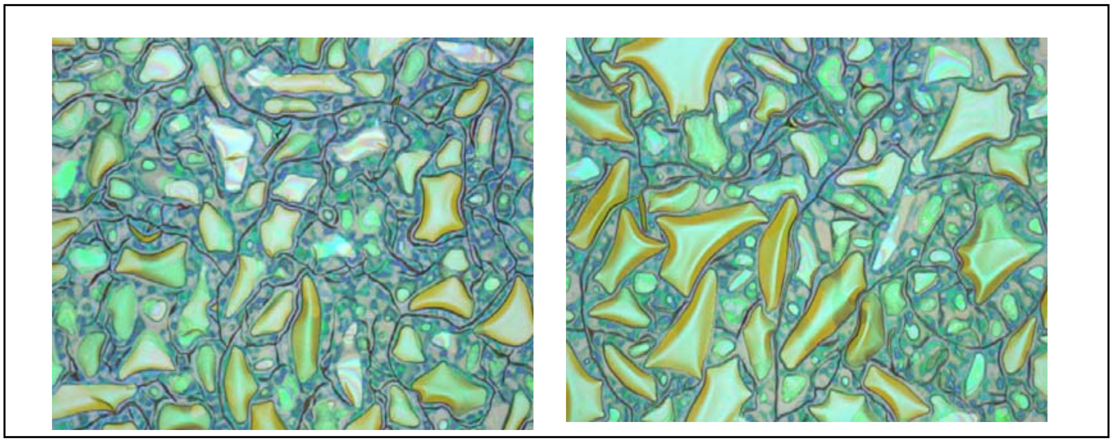

Figure 30. Microscope Images Pitt Sol-Gel Films (First Pitt Trial)

It can be seen that the films exhibit severe problems both with hillocks (bubbles) and with cracking. One reason for this is likely the lack of SiO_2 layer serving as an adhesion layer for the ZrO_2. However, as later results showed, the processing conditions also played an important role in these material defects.

As the first step in obtaining higher quality films, a second SiO_2 layer (LPCVD) was added to the top of the layers for purposes of adhesion. Since the SiO_2 layers were extremely thin (1000A), it was hoped that having an extra layer would not significantly affect the stress in the beams, or even that the sandwiching of the SiNx between the SiO_2 films would results in a better stress distribution.

Also in the next round of processing tests, the ZrO_2 annealing time was increased from 20 minutes to 3 hours. This process change came as a suggestion through personal communication with researchers Wonjae Choi and Robert Xia of MIT as a potential solution for crack reduction. Pictures at this stage of the $Si/SiO_2/SiNx/SiO_2$ substrates with a layer of ZrO_2 and two layers of PZT are shown in Figure 31.

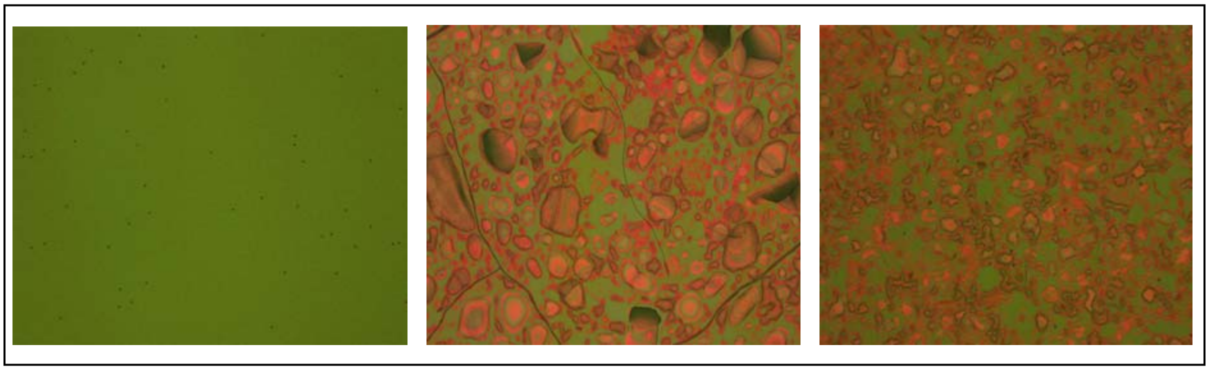

Figure 31. Microscope Images Pitt Sol-Gel Films (Second Pitt Trial)

A very small section of the wafer, hypothesized to be an area that only received one layer of PZT coating, showed to have a clean surface structure, and the majority of the wafer appeared to be largely crack-free. However, there was still a large problem with hillocks across almost the entire wafer, and thus additional process changes were sought out to decrease this effect, since hillocks can cause electric shorting within sensor and actuator microdevices as well as lead to increased probability of microcracks (Dai, 2004).

Literature research suggests that PZT thin films can exhibit hillocks for several reasons. Primary among these is the fact that high-temperature annealing causes volume reduction of the PZT solution, thus initiating contraction and deformation in the PZT film. Also, at higher temperatures, grain sizes are larger, and recrystallized grains are known to lead to hillocks and cracking (Dai, 2004). Since high-temperature annealing is necessary to transform the amorphous PZT to the preferred perovskite phase, it was desired to find an annealing temperature which would not result in hillocks, but would still allow for complete transformation to the perovskite phase. Some studies have suggested that the perovskite phase appears at 500C, with crystallization increasing with increased annealing temperatures up to 625C (Velu, 1996). Thus, the annealing temperature of PZT was changed from 650C to 625C for the next round of testing. Furthermore, two sets of trials were done at this temperature; one annealing after every spin coat of PZT and another annealing after every 2 coats (same as before), in order to monitor any differences in results between these two methods. Results from both methods after each annealing step are shown in Figures 32 and 33.

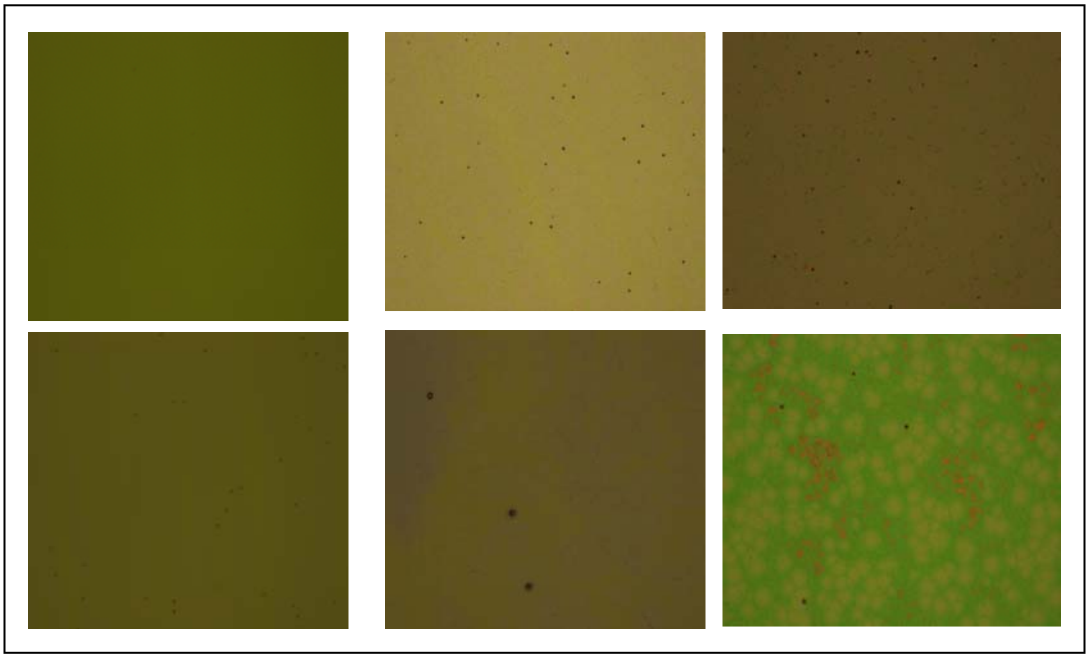

After 1st Annealing After 2nd Annealing After 3rd Annealing

Figure 32. Microscope Images Pitt Sol-Gel Films (Third Pitt Trial)

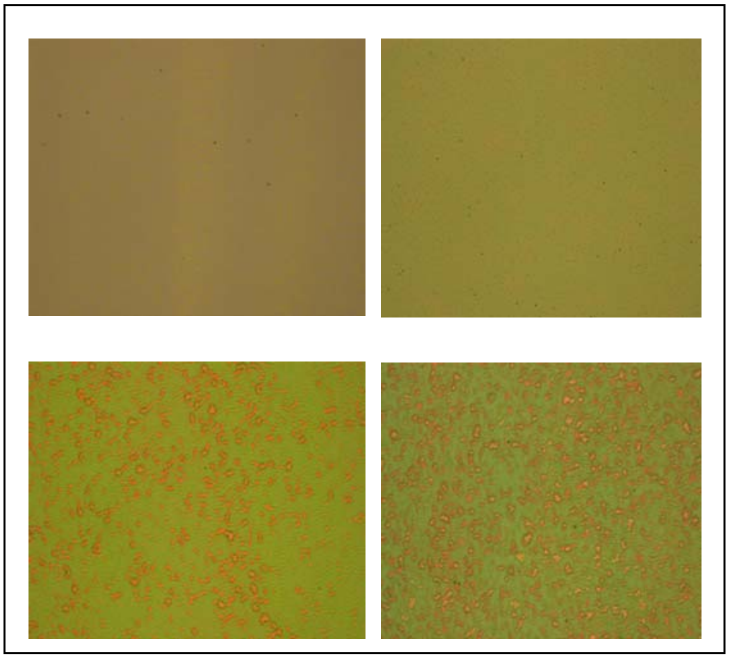

After 1st Annealing After 2nd Annealing

Figure 33. Microscope Images Pitt Sol-Gel Films (Fourth Pitt Trial)

As can be seen, the quality of the films is significantly improved at this lower annealing temperature. Although there is some evidence of hillocks appearing at the third stage of annealing in the first set of results and at the first stage of annealing in the second set, in both cases the hillocks were only found at the very edge of the wafers, and the majority of the surface appeared to be free of both hillocks and cracks. By means of the microscope pictures, it was hard to gauge whether annealing after every layer had positive or adverse effect on the quality of the PZT films, as there was not a significant difference in the size or amount of the defects that were present.

Although this process plan appeared to give good results during this trial, results using this recipe were not repeatable with further wafers. Three more wafers were tested using this same process, and each came out with severe hillocks across the entire surface of the wafer and poor XRD results, as will be discussed in the next section. Consequently, the process was further modified to find a more consistent process for yielding crack, hillock-free wafers with good piezoelectric properties.

Since the annealing temperature appeared to play the most important role in causing hillocks, the PZT annealing temperature was further reduced to 600C for the next round of fabrication. A more gradual heating and cooling process was also used for these trials, where the wafers were heated from/cooled to 350 C in the annealing furnace before and after the annealing, respectively. It was thought that this more gradual heating might make the volume reduction of the PZT sol-gel solution more controlled, thus minimizing one of the potential causes of hillocks. Three separate wafers were processed using this technique, and all appeared to give good crack-free, hillock-free surfaces across the entire PZT film. Figure 34 shows microscope images of these wafers.

Figure 34. Microscope Images Pitt Sol-Gel Films (Fifth Pitt Trial)

When XRD results suggested that the piezoelectric properties of the PZT annealed at the lower temperature were not as good as those annealed at 625, a final stage was added to the previous process plan where a single 625 degree annealing was done after the deposition of all four PZT layers (with the corresponding prior annealing steps in place), also using the gradual heating/cooling process described previously. It was hoped that by minimizing the 625 annealing phase to a single step, done after previous 600C annealing steps and using the gradual heating/cooling process, the chances of hillocks would be minimized without sacrificing the quality of the film with respect to piezoelectric properties. Figure 35 summarizes this entire process flow and Figure 36 gives microscope imagines of the wafers after the completion of this process.

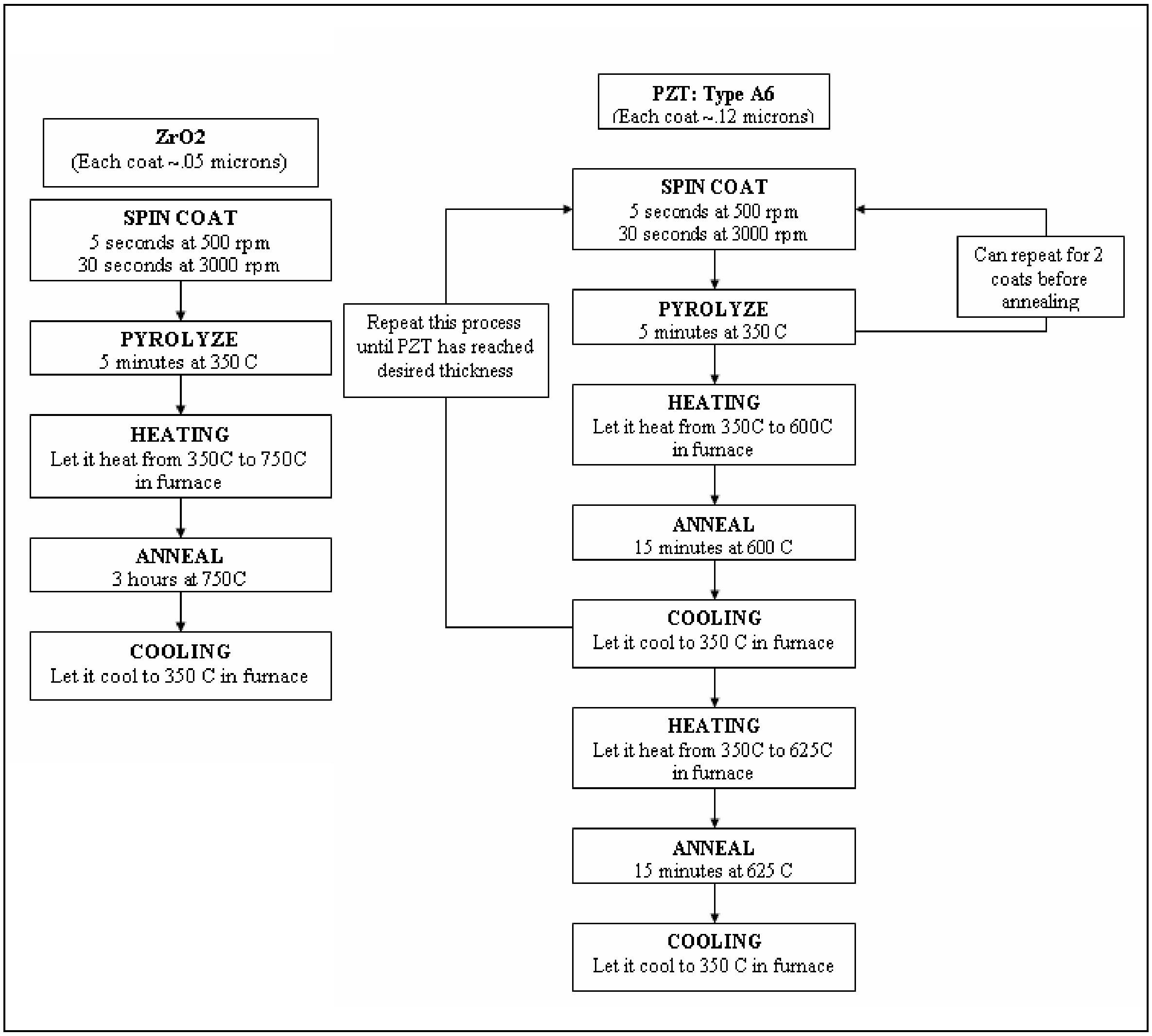

Figure 35. Final Process Plan for Processing PZT Thin Films

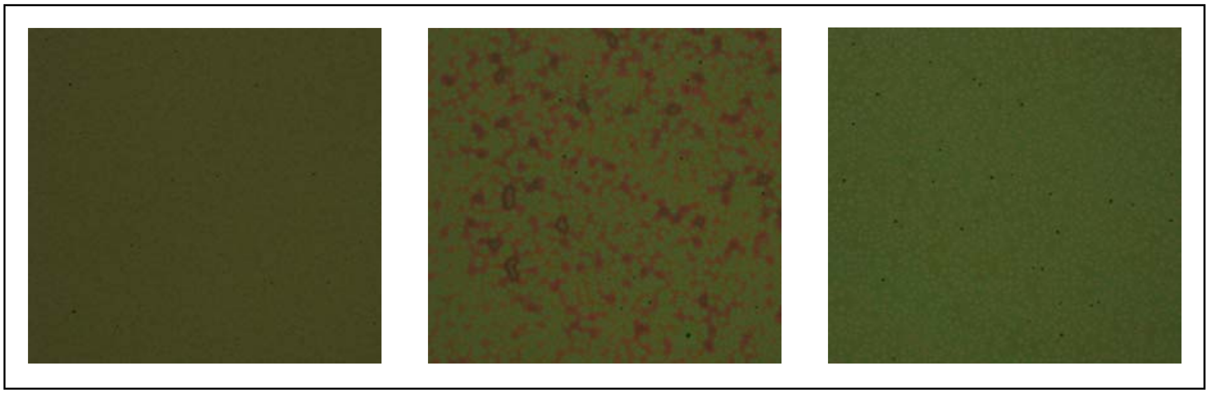

Figure 36. Microscope Images Pitt Sol-Gel Films (Sixth Pitt Trial)

Although some hillocks did begin to appear with this final annealing step, they were not present in all three samples, and were not found across the entire surface of the wafer in any of the three samples. Thus it was judged that this process plan was the most effective in consistently giving quality PZT thin-film results, exhibiting good piezoelectric properties, no cracks, and minimal hillocks. Thus the process flow described by Figure 35 was established as the final processing method which should be used for future fabrication of ZrO_2 and PZT films.

A chart summarizing the sol-gel process recipes and their corresponding results is given in Table 7.

Table 7. Summary of Sol Gel Processing

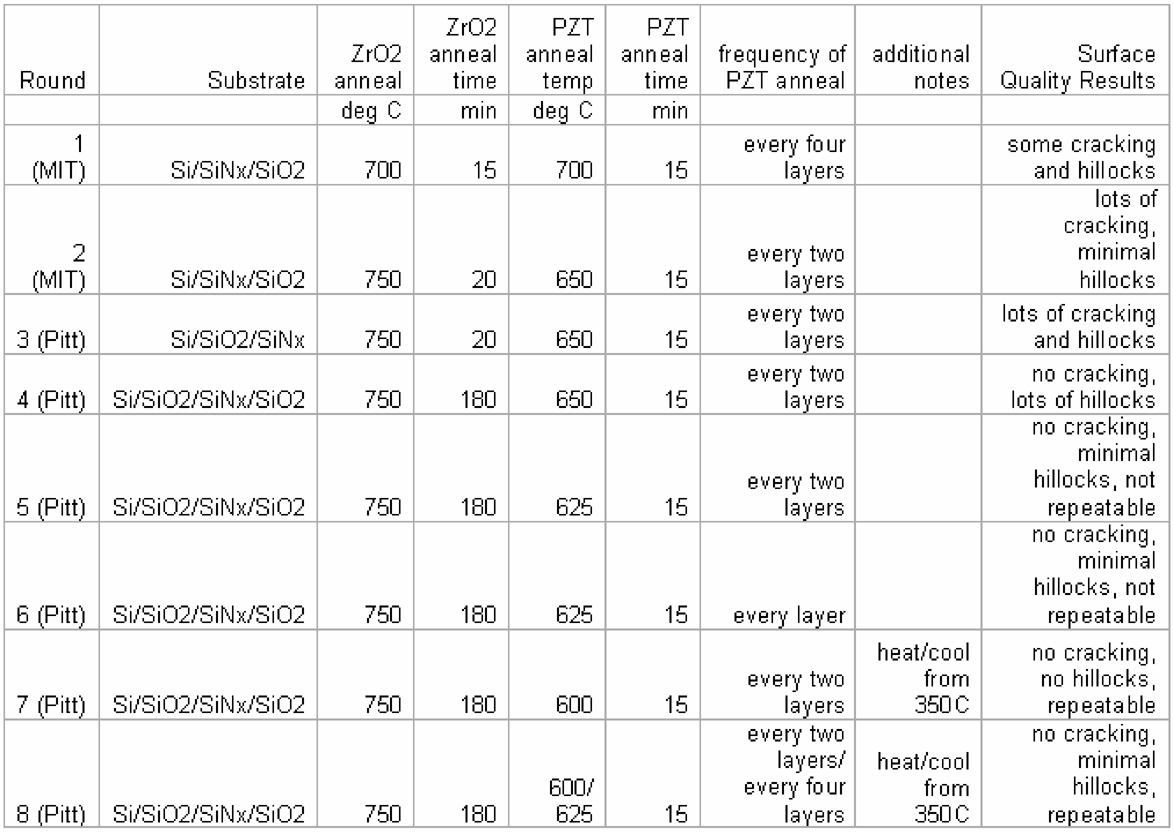

Round	Substrate	ZrO2 anneal	ZrO2 anneal time	PZT anneal temp	PZT anneal time	frequency of PZT anneal	additional notes	Surface Quality Results
		deg C	min	deg C	min			
1 (MIT)	Si/SiNx/SiO2	700	15	700	15	every four layers		some cracking and hillocks
2 (MIT)	Si/SiNx/SiO2	750	20	650	15	every two layers		lots of cracking, minimal hillocks
3 (Pitt)	Si/SiO2/SiNx	750	20	650	15	every two layers		lots of cracking and hillocks
4 (Pitt)	Si/SiO2/SiNx/SiO2	750	180	650	15	every two layers		no cracking, lots of hillocks
5 (Pitt)	Si/SiO2/SiNx/SiO2	750	180	625	15	every two layers		no cracking, minimal hillocks, not repeatable
6 (Pitt)	Si/SiO2/SiNx/SiO2	750	180	625	15	every layer		no cracking, minimal hillocks, not repeatable
7 (Pitt)	Si/SiO2/SiNx/SiO2	750	180	600	15	every two layers	heat/cool from 350C	no cracking, no hillocks, repeatable
8 (Pitt)	Si/SiO2/SiNx/SiO2	750	180	600/ 625	15	every two layers/ every four layers	heat/cool from 350C	no cracking, minimal hillocks, repeatable

5.1.3 XRD Testing

XRD testing is commonly used to determine crystalline phases, crystallographic texture, and crystal plane orientations of thin films. For this project, XRD testing served as a means for a more quantitative judgment of the quality of the PZT films that had been processed. While amorphous materials will not have clearly defined peaks, PZT that has completed its structural change from the amorphous to the perovskite phase should only feature peaks associated with the established diffraction pattern for ideal PZT films. The Joint Committee for Powder Diffraction Studies (JCPDS) diffraction data defines the peaks associated with the perovskite phase of PZT, as well as their related relative intensities. Perovskite PZT can be verified by preference to the (111) orientation, and the greater the intensity of PZT (111), the better the piezoelectricity of the film (Dai, 2004).

The principle behind X-ray diffraction testing is based on Bragg's Law. Diffraction occurs when waves interact with a structure whose repeat distance is approximately the same as the wavelength of the source. XRD-testing works since X-rays have wavelengths on the order of a few angstroms, the same distance as typical interatomic distances in crystalline solids. When the necessary geometric requirements are met, X-rays scattering from the crystalline material will constructively interfere, producing a diffracted beam. The angle of diffraction (θ), the wavelength of the wave source (λ), and the interatomic spacing (d) of the material can then be related by Bragg's law, or $n\lambda = 2d\sin\theta$. In XRD testing, the X-ray intensity is recorded as a function of a 2-theta angle, and the plot of this information is known as the diffraction pattern for the material.

Two primary types of measurements are done with XRD testing, and both were used to analyze the quality of the PZT films. The first of these is the standard 2-theta test. The important parameters for the 2-theta tests done on the PZT films at the University of Pittsburgh are given in Table 8.

Table 8. Parameters for 2-Theta XRD Test at University of Pittsburgh

wavelength of the wave source	1.54	angstrom
starting angle	20	theta
step size	0.02	theta
time per step	0.5	sec
ending angle	67	theta
divergence angle	1/2	theta
length from x-ray to sample	173	mm

The wavelength is a material property of the source material: for the XRD machine at the University of Pittsburgh, the source is copper, so the associated wavelength is 1.54 angstrom. Step size and time per step values are fairly standard for XRD testing, as is a 20 degree 2-theta starting angle. 67 was used as the 2-theta ending angle in order to get a good amount of measurement data, while still stopping before the large 69 degree peak that is characteristic of silicon (the substrate material).

The second of the tests is the glancing angle test. The glancing angle test allows for better control of the depth of penetration of the wave source: consequently, it can be used to measure the properties at different thicknesses in a wafer, or to better separate the properties of a thin film layer from its substrate. In this case, the glancing angle test allowed for two primary capabilities. First, it allowed the test to be run over a wider range of theta without worrying about catching the intense peaks of the silicon substrate in the data. Additionally, and more importantly for these tests, by isolating the test to the top layer, it also allowed the tests to gauge whether the non-PZT-associated peaks found for some of the trials were a result of the lower thin films/substrate ($Si/SiO_2/SiNx/ZrO_2$ layers) or of incomplete transformation of the PZT. The relevant parameters for the glancing angle tests performed on the PZT films at the University of Pittsburgh are given in Table 9.

Table 9. Parameters for Glancing Angle XRD Test at University of Pittsburgh

wavelength of the wave source	1.54	angstrom
starting angle	20	theta
step size	0.02	theta
time per step	0.5	sec
ending angle	80	theta
sample angle	2	theta
divergence angle	1/2	theta
length from x-ray to sample	173	mm

As Table 9 displays, the ending angle (80 degrees) is higher in the glancing angle test. Also, an additional parameter, the sample angle, is set at 2 degrees. This parameter is influential in determining the penetration depth as well as the length of area examined across the wafer (known as the illuminated length). The illuminated length can be calculated using the formula

$$A = \frac{r * \tan\delta}{\sin\Theta} \tag{52}$$

where A is the illuminated length, r is the length from the X-ray to the sample, δ is the divergence angle, and Θ is the angle at which the sample is held. For the tests performed here, A was found equal to 43.26 mm or 1.7 inches, meaning just under half the length of the wafer was sampled during the tests. Also, by keeping the sample angle relatively small, the glancing angle test was able to isolate the XRD measurements to the PZT (topmost) layer.

Unfortunately, the benefits of the glancing angle test do not come without their drawbacks, for the intensity and peak measurements are not as sharp in the glancing angle test as they are in the 2-theta test. This is a result of the fact that the measurement is being taken over a much wider length of the sample, thus making the refracted signal less well-defined. Different combinations of the glancing angle and two-theta tests were done on the PZT samples throughout to draw the necessary conclusions for distinguishing the quality of the films.

The relative intensities associated with the diffraction measurements for perovskite PZT, as given by the JCPDS database, are displayed in Table 10.

Table 10. JCPDS Diffraction Data for PZT

2 Theta	Intensity	h	k	l
21.415	9	0	0	1
22	12	1	0	0
30.917	u	1	0	1
31.362	100u	1	1	0
38.252	15	1	1	1
43.627	9	0	0	2
44.88	16	2	0	0
49.383	5	1	0	2
50.375	6	2	0	1
50.375		2	1	0
53.345	5			
54.688	12	1	1	2
55.477	24	2	1	1
64.378	9	0	2	2
65.341	5	2	2	0
67.75	2	0	0	3
68.941	u	2	1	2
69.583	6u	2	2	1

This diffraction pattern was also superimposed on each of the XRD plots for comparison purposes.

XRD tests were first performed on the Si/SiO_2/SiNx films with the original MIT processing recipe used for the ZrO_2 and PZT film deposition (processing round 3 at the University of Pittsburgh in Table 7). As noted earlier, these wafers showed clear problems with cracking and hillocks. The corresponding XRD test is shown in Figure 37.

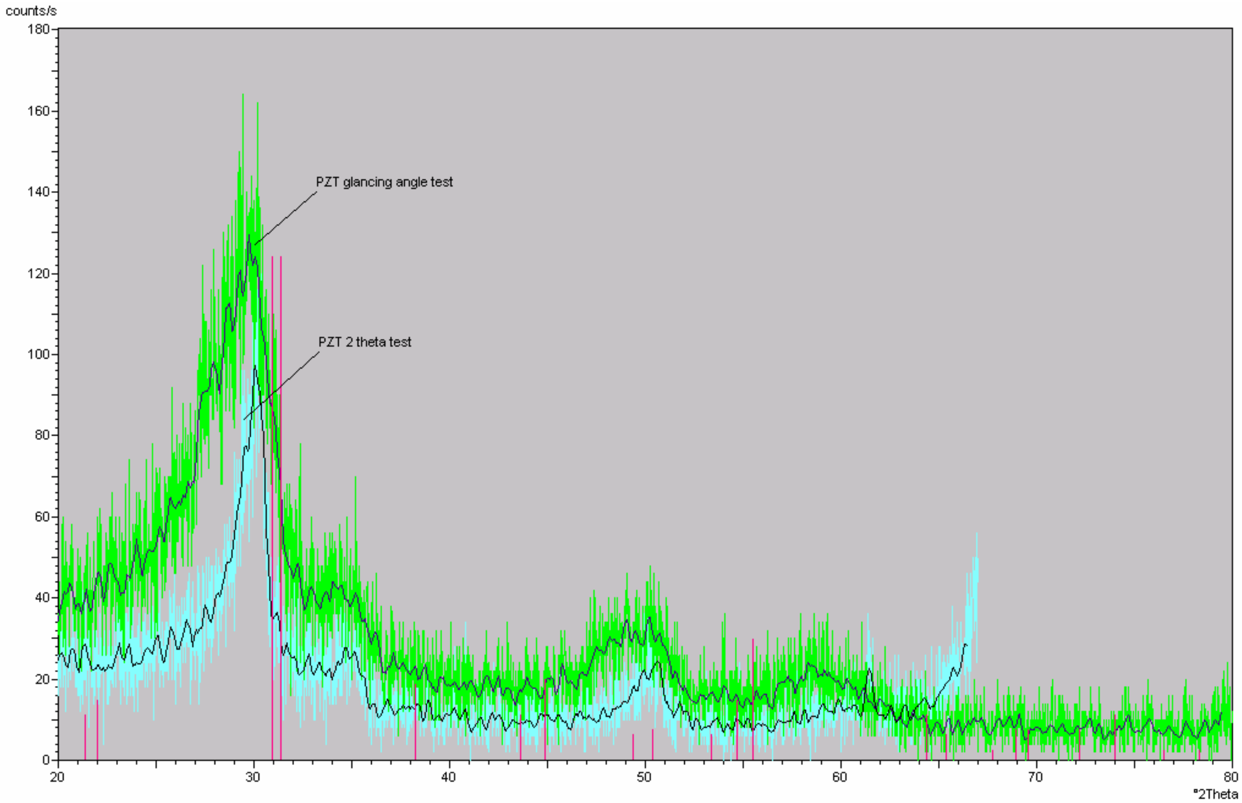

Figure 37. XRD Plot for Round 3 PZT Film

As expected, the poor quality of this PZT film is evident through the lack of clarity and low intensity in the peaks, as well as the poor alignment with the established diffraction pattern.

The tests were next done on the rounds five and six results, the Si/SiO2/SiNx/SiO2 substrates with the processing recipe that originally was found to give quality, crack-free, hillock-free results. XRD diffraction data for these two rounds are given in Figures 38 and 39.

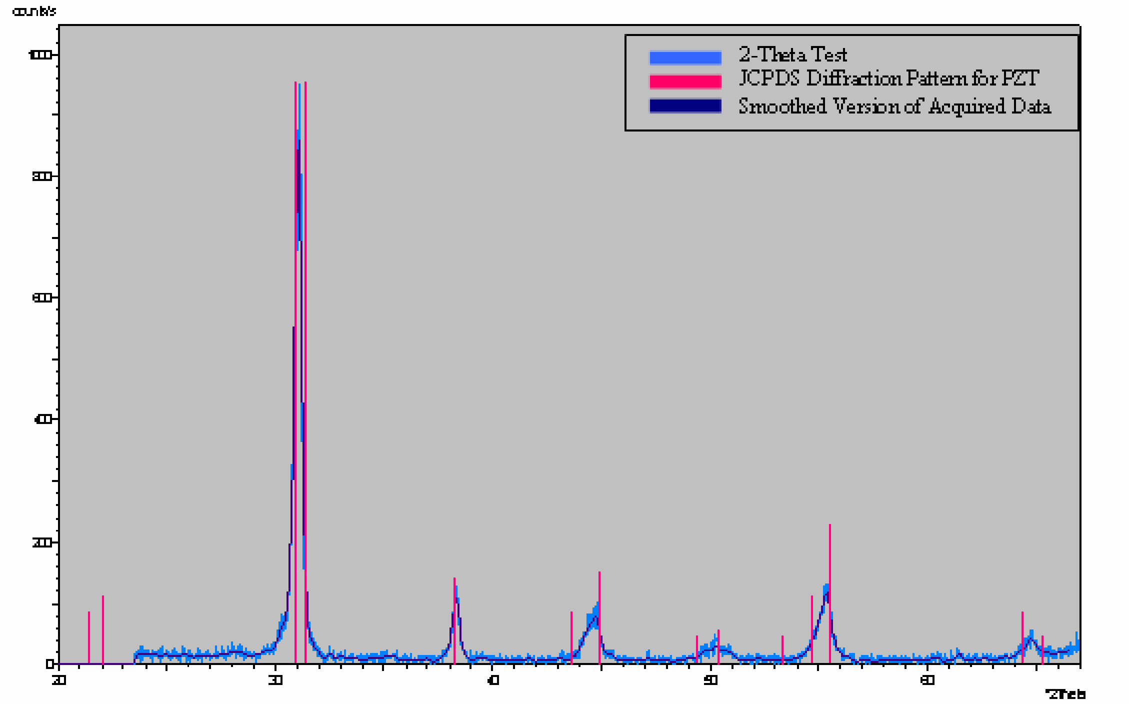

Figure 38. XRD Plot for Round 5 PZT Film

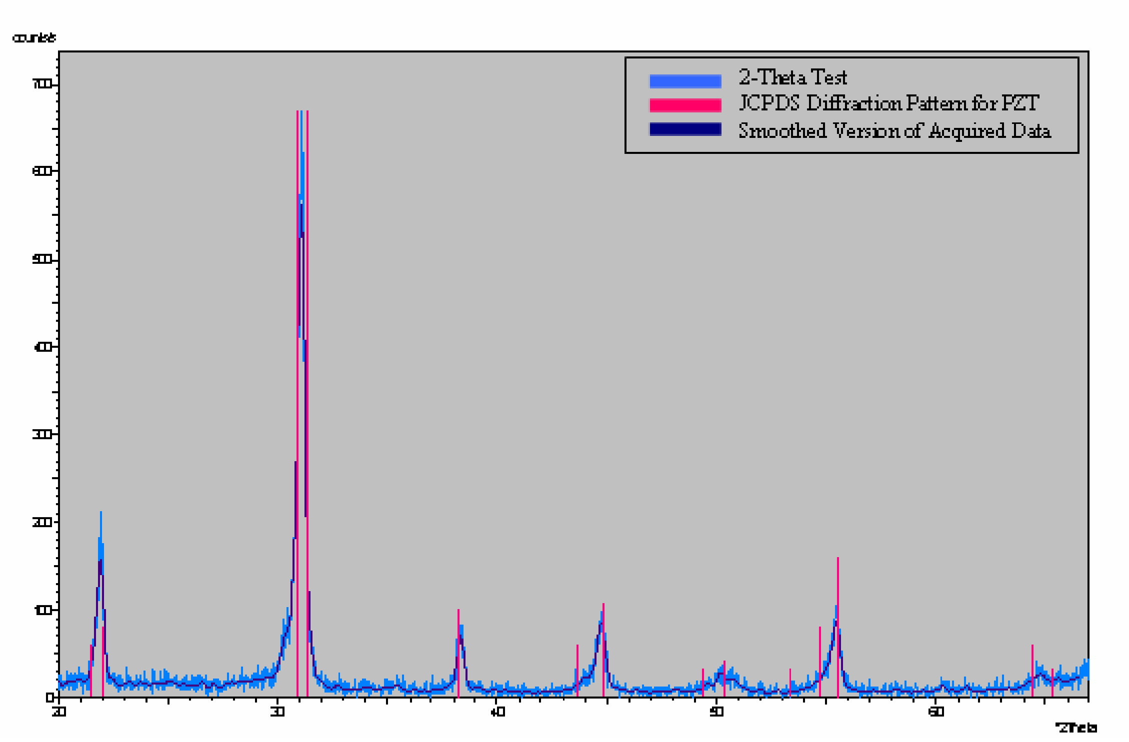

Figure 39. XRD Plot for Round 6 PZT Film

Clearly, the quality of the film is significantly improved. The peaks are much sharper, significantly more intense, and much better aligned to the established diffraction pattern. These findings, in combination with the lack of appearance of other peaks not associated with the perovskite PZT, indicate a film that has completed its transformation to the perovskite phase, a result indicative of good piezoelectric quality in the film. The splitting in the peaks (for instance, the 101 and 110 peaks at the primary 31 degree peak) notable in the established diffraction pattern was not observed, thus indicating that the PZT film was in the rhombohedral phase rather than the tetragonal (Abe, 1995); however, since the rhombohedral and tetragonal phases coexist at the desired morphotropic phase boundary (52/48 Zr/Ti), the material composition whereat the piezoelectric properties are known to be the best quality (Cross, 2004), the results were judged to be of the desired composition. It can also be noted that the wafers which were annealed only after every other PZT spin coating process showed slightly better XRD results, having more intense diffraction peaks. Glancing angle tests were not done on these samples since the only peaks present were those of the established PZT phase and the majority of the PZT peak information could be found below the 67 degree end point.

When this previously successful process plan started to yield unrepeatable results, one of the corresponding wafers (judged to be of poor quality from the abundant amount of hillocks found across the film) underwent an XRD test in order to verify that these wafers were indeed inferior. The corresponding test results are shown in Figure 40.

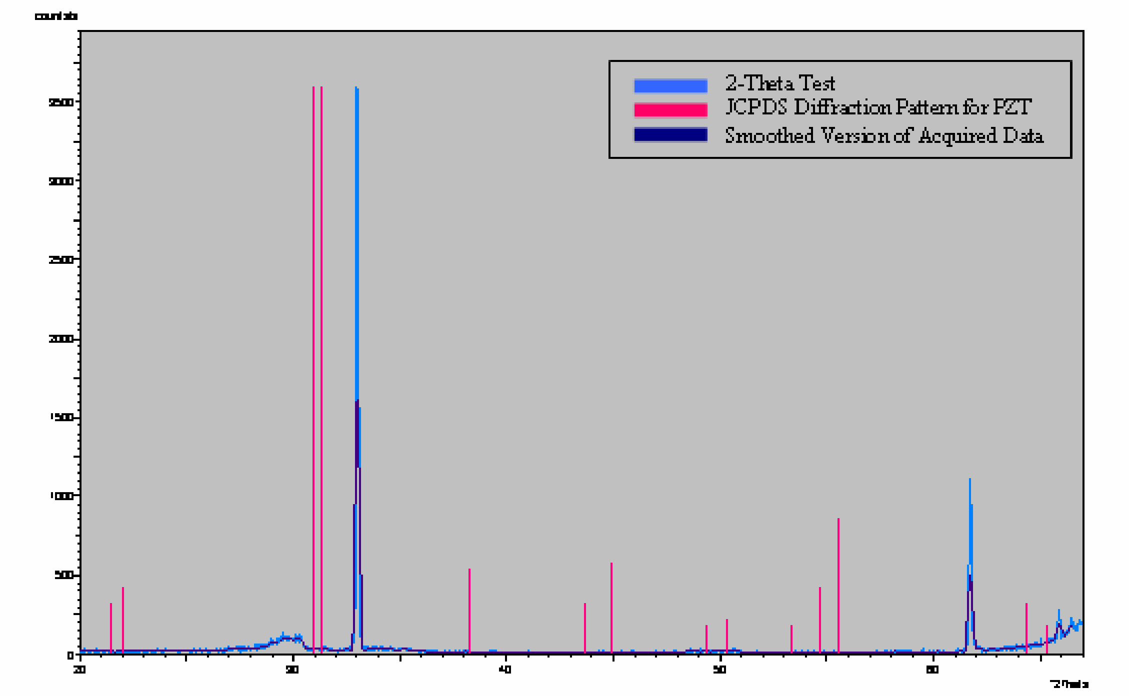

Figure 40. XRD Plot for a Repetition of Round 6 PZT Film

These results validate the hypothesis about the poor-quality of this film, since the peaks are not well-aligned with the established PZT pattern.

The next XRD test was done on round seven of the processed films, those with the 600 C annealing temperature. This result is given in Figure 41.

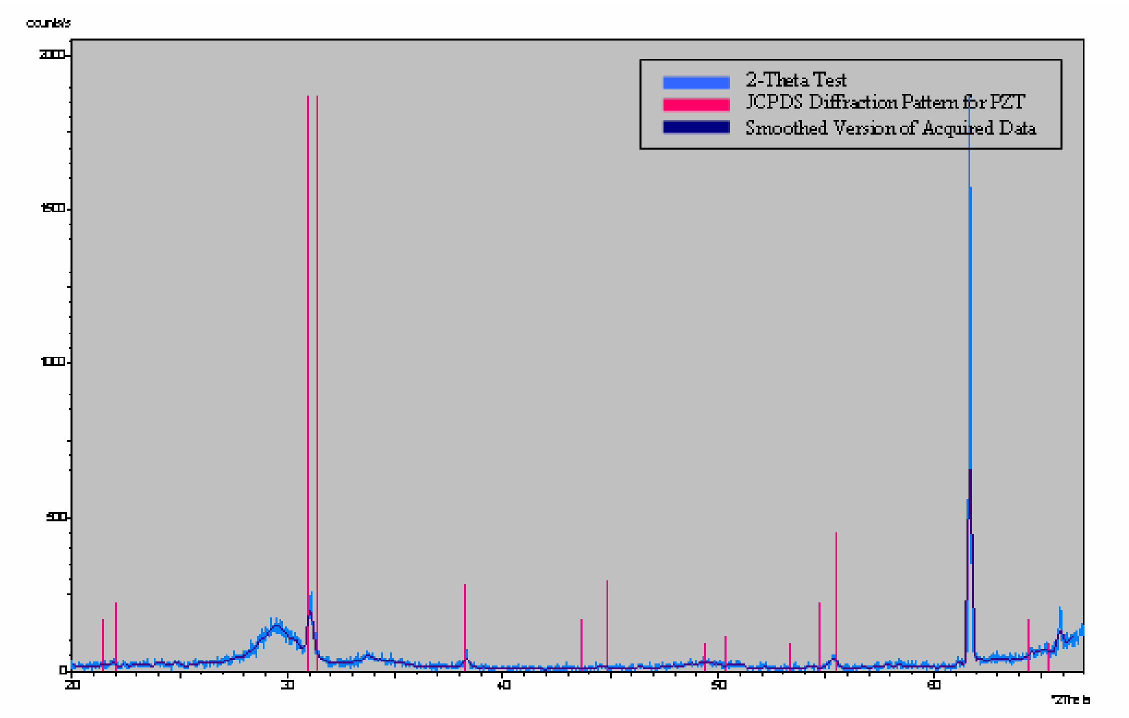

Figure 41. XRD Plot Round 7 PZT Film

It can be seen that the peaks have become better aligned to the established diffraction pattern with this technique, but it is also evident that they are not as intense as they had been in previous trials when annealed at 625 C, and that not all established PZT peaks are present. Focusing in on the primary peak of PZT, located at around 31 degrees, the intensity is measured to be just above 250 counts/second, as compared with results around 600-900 counts/ second for the prior high-quality films. Thus it was determined that to maximize the quality of the films, the 625 degree annealing was most likely necessary to complete phase transformation.

In the final process (round eight) with the single 625 degree annealing step and extra heating precautions, the XRD tests showed better results. Figure 42 shows the results for the same wafer used in trial seven with the extra annealing step added.

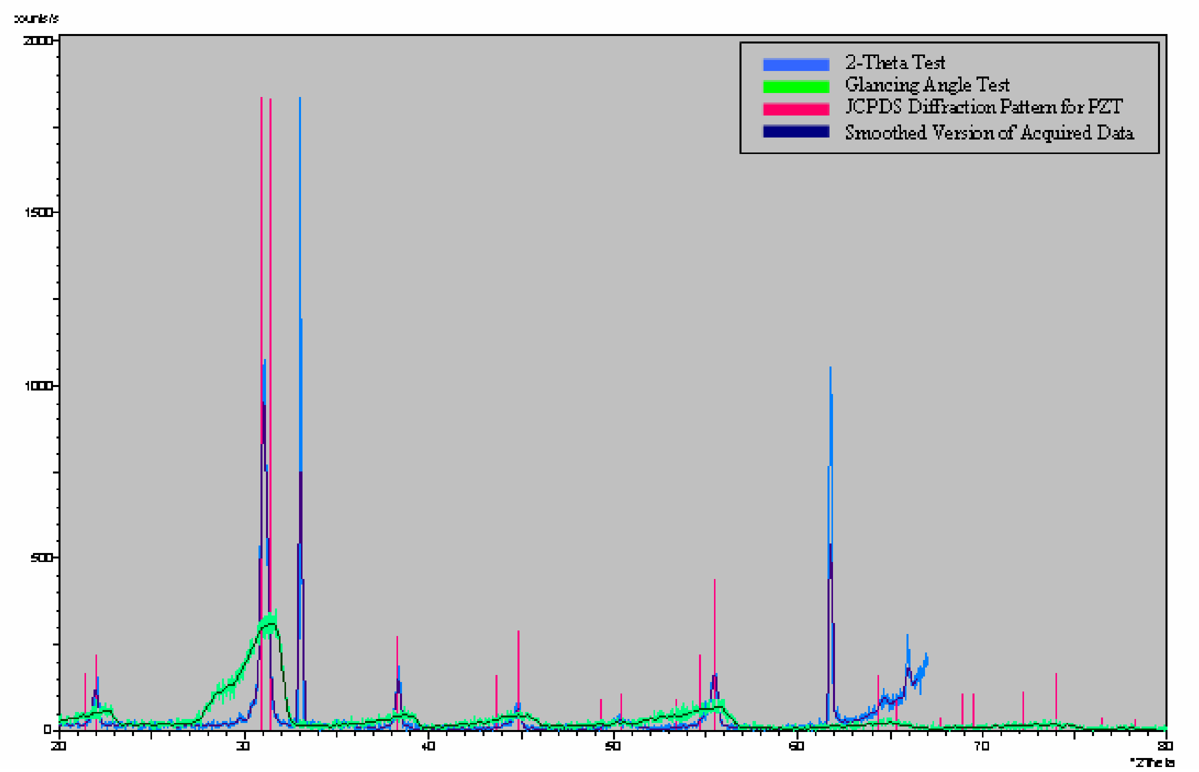

Figure 42. XRD Plot Round 8 PZT Film

The significant improvement with the 625C annealing step is evident through a comparison between these two trials. In Figure 42 (after the 625 annealing) the peaks are significantly more intense (the 31 degree peak now over 1000 counts/ second) and many of the later peaks that had not shown up before are now present. Some additional peaks, not corresponding to the established PZT pattern, are still there, but the results of the glancing angle test indicated these to be peaks not associated with the topmost layer, and thus they can be assumed to be a contribution from one of the support layers rather than an indication of an incomplete phase transformation in the PZT film.

Additional XRD tests were also done on the second and third wafers fabricated using the final process (Figures 43 and 44, respectively). These tests were done to verify the consistency of the quality of this processing, particularly since some hillocks were appearing at the 625 annealing step at portions of the later wafers.

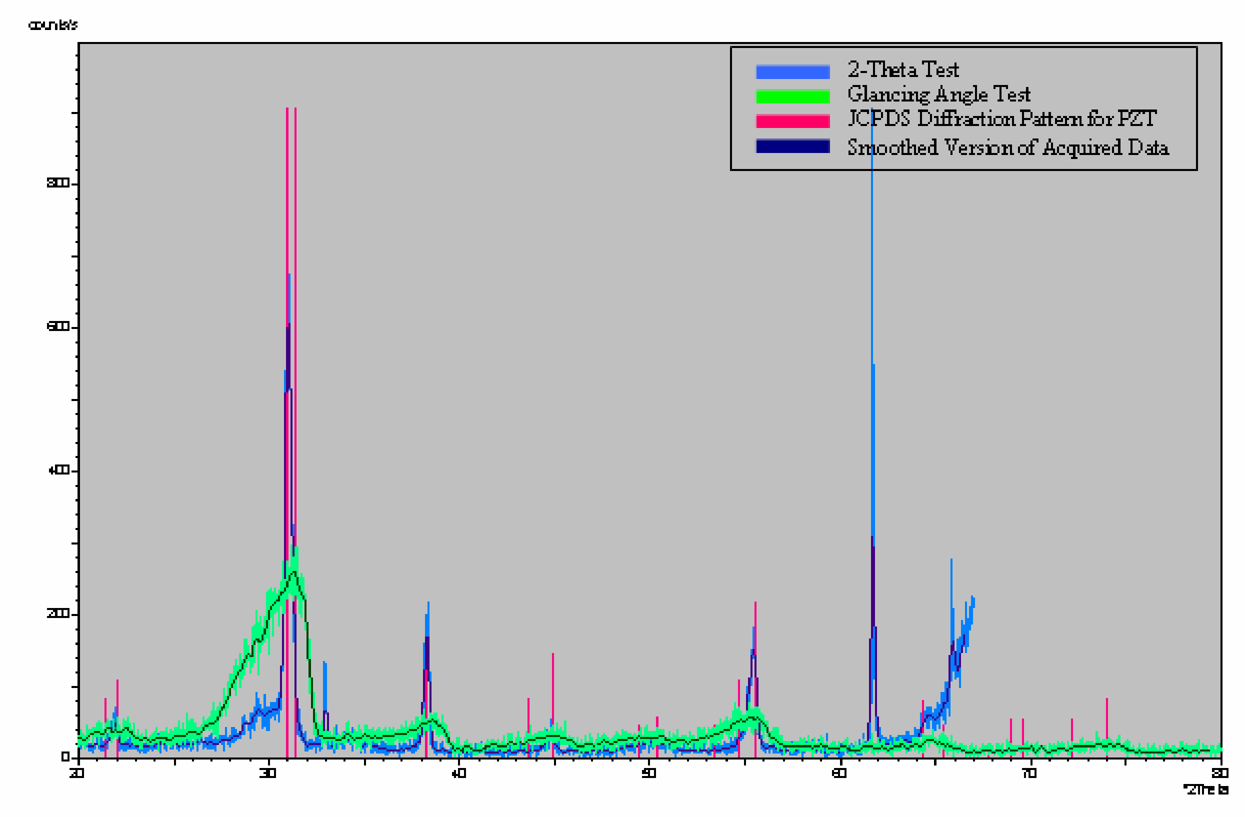

Figure 43. XRD Plot for Repetition 1 of Round 8 PZT Film

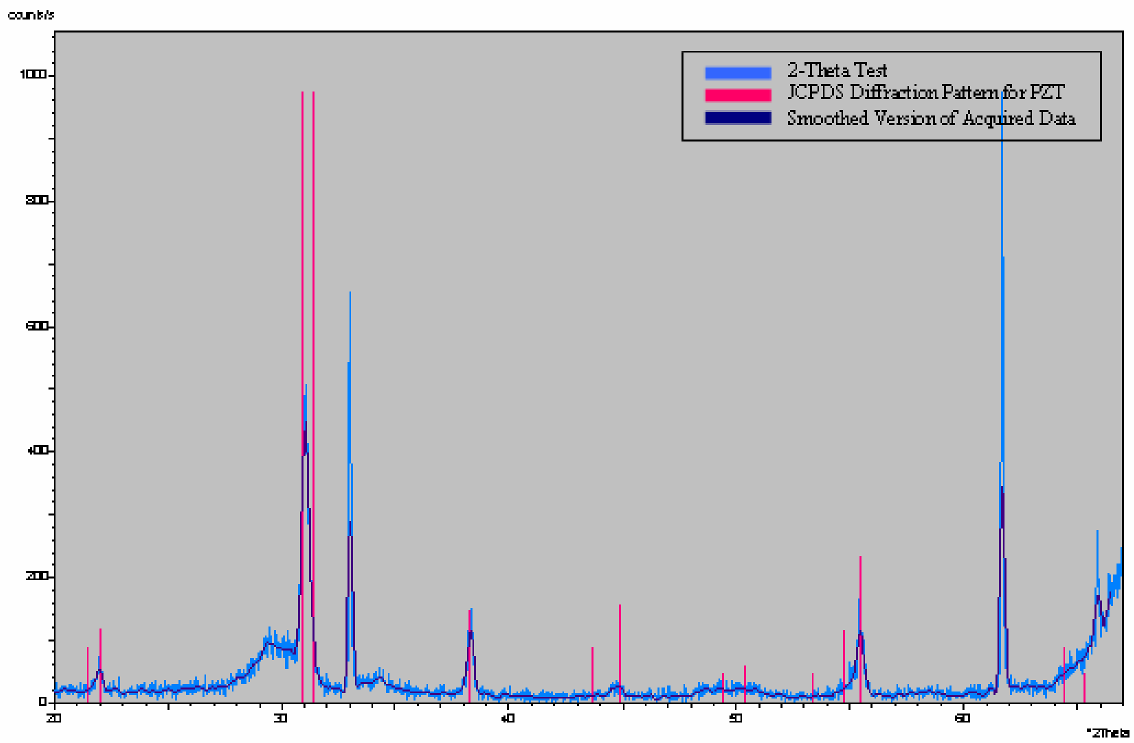

Figure 44. XRD Plot for Repetition 2 of Round 8 PZT Film

Although the peaks are not as intense as for the original sample, they are still relatively high, and well aligned. Thus it was concluded that the piezoelectric properties of these samples were of good quality, and that they could still be usable for device fabrication.

One final test was done in order to determine the consistency of the piezoelectric properties across one of these round eight repetition samples. The XRD 2-theta test was repeated at two different points on the wafer, one which had small hillocks and one which did not. The corresponding plot is shown in Figure 45.

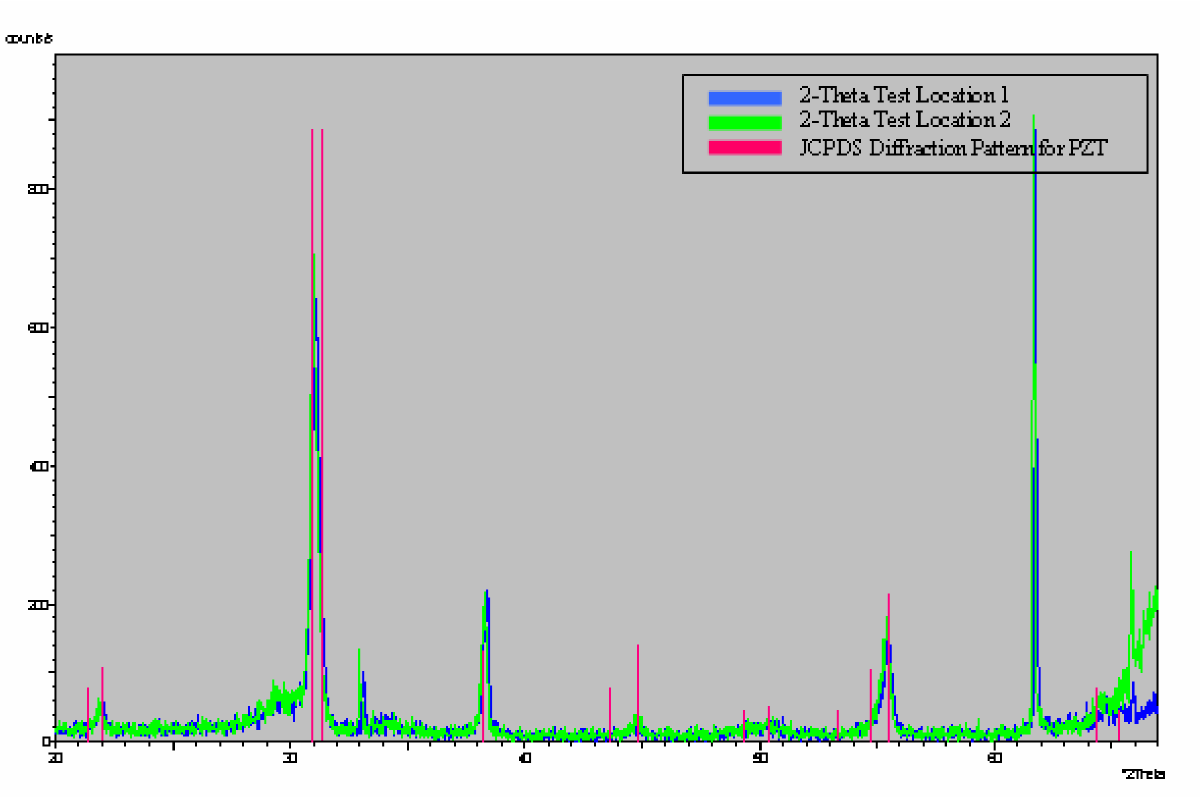

Figure 45. XRD Plot for Repetition of Round 8 PZT Film at Two Different Locations on the Same Wafer

As is apparent from the figure, the XRD results are highly consistent at the two different points on the sample, thus indicating that in the case of this wafer, the beginning of the appearance of hillocks does not adversely effect the piezoelectric properties of the PZT film. The results further indicate that film properties can be thought to be consistent across the surface of the wafer.

A chart summarizing the trails and the results of the corresponding XRD tests is given in Table 11.

Table 11. PZT Trials and Their Corresponding XRD Results

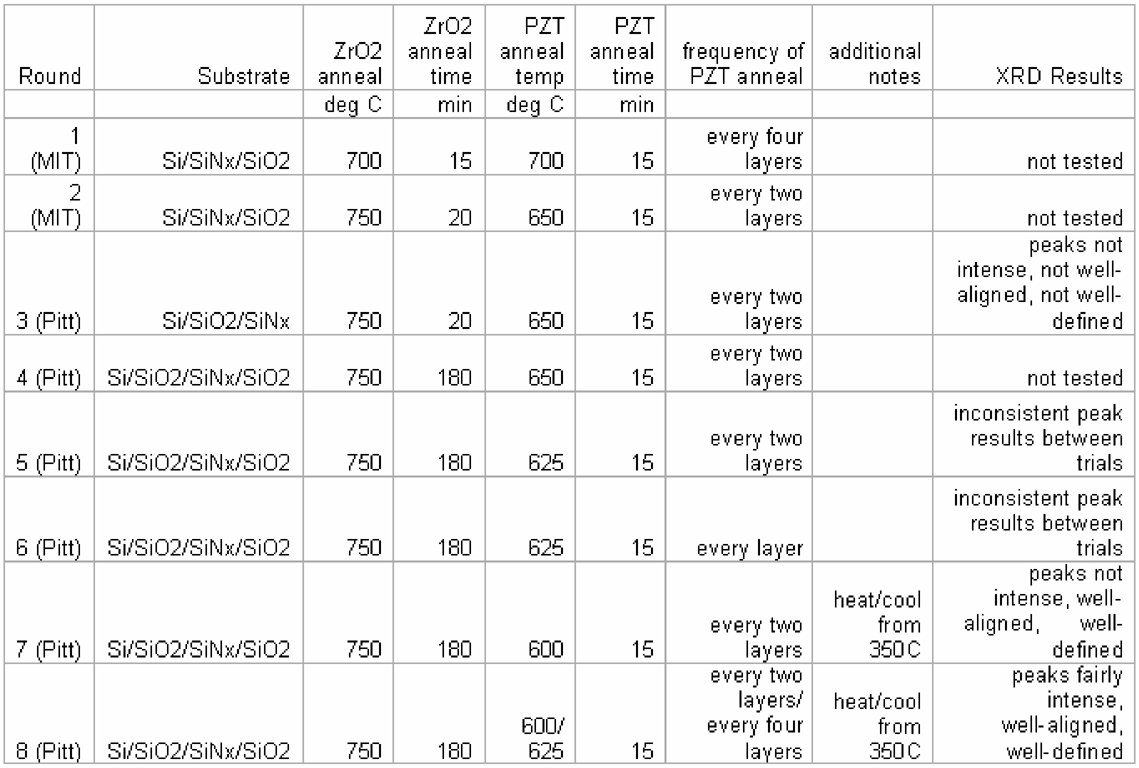

Round	Substrate	ZrO2 anneal	ZrO2 anneal time	PZT anneal temp	PZT anneal time	frequency of PZT anneal	additional notes	XRD Results
		deg C	min	deg C	min			
1 (MIT)	Si/SiNx/SiO2	700	15	700	15	every four layers		not tested
2 (MIT)	Si/SiNx/SiO2	750	20	650	15	every two layers		not tested
3 (Pitt)	Si/SiO2/SiNx	750	20	650	15	every two layers		peaks not intense, not well-aligned, not well-defined
4 (Pitt)	Si/SiO2/SiNx/SiO2	750	180	650	15	every two layers		not tested
5 (Pitt)	Si/SiO2/SiNx/SiO2	750	180	625	15	every two layers		inconsistent peak results between trials
6 (Pitt)	Si/SiO2/SiNx/SiO2	750	180	625	15	every layer		inconsistent peak results between trials
7 (Pitt)	Si/SiO2/SiNx/SiO2	750	180	600	15	every two layers	heat/cool from 350C	peaks not intense, well-aligned, well-defined
8 (Pitt)	Si/SiO2/SiNx/SiO2	750	180	600/ 625	15	every two layers/ every four layers	heat/cool from 350C	peaks fairly intense, well-aligned, well-defined

5.2 MASK DESIGN

Before any patterning could be done, the first steps in the processing of the resonators were device design and mask making. Several beam designs were drawn up which would test the results of the parameter study described in the theoretical analysis of bending beams portion of this work, and a few variations on these patterns were made for testing some newly brainstormed ideas.

To begin, basic length and electrode size dimensions were chosen by looking at previously processed designs of successfully fabricated interdigitated, piezoelectric devices. Beyond this, the minimum dimension sizes achievable with Pitt lithography capabilities were kept in mind, as was the 1:10:100 (height: width: length) standard for beam dimensioning. Each beam was given its own electrode pads so that voltage leakage would not become a problem. The beams were also arranged so that the majority of the electrode pads were placed in a rectangular array outside the beams, as shown in Figure 46. This was done to minimize the difficulty of wire bonding to electrode pads.

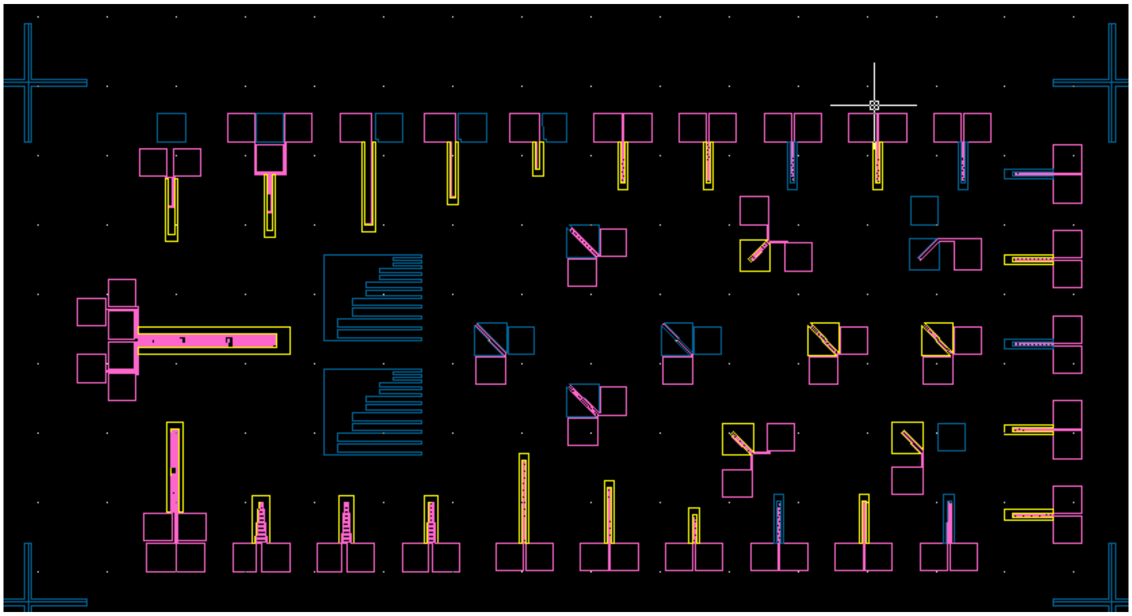

Figure 46. Rectangular Array of MEMS Beam Designs

Three masks were drawn: one for the beams, one for top electrode designs and one for bottom electrode designs (to be used only in the case of fabricating d31 devices). A single rectangle for each of these layers is shown in Figures 47, 48, and 49.

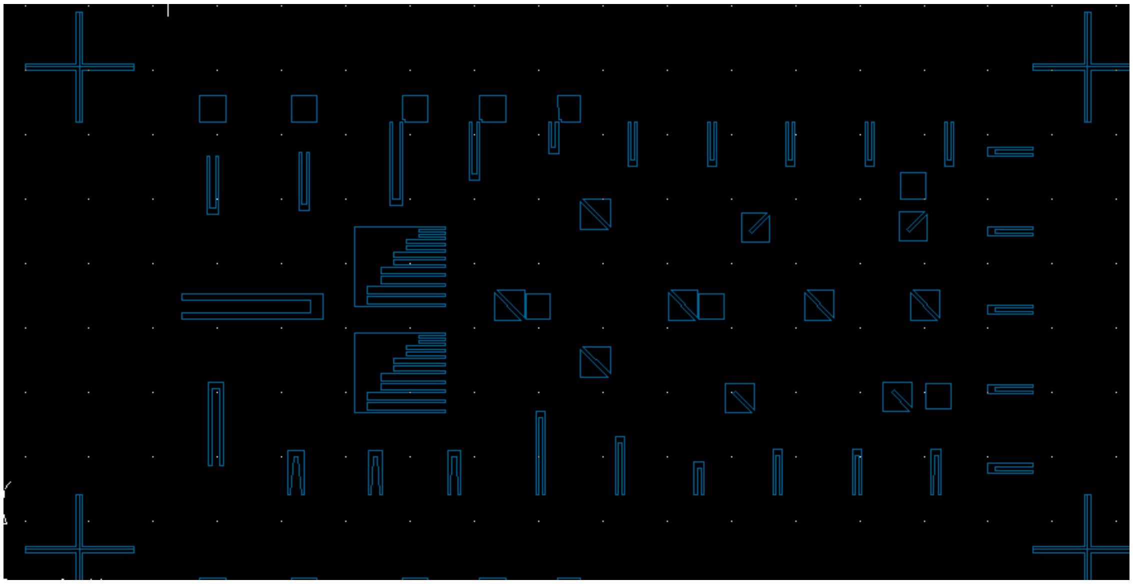

Figure 47. Rectangular Array of MEMS Bottom Layer Electrode Designs

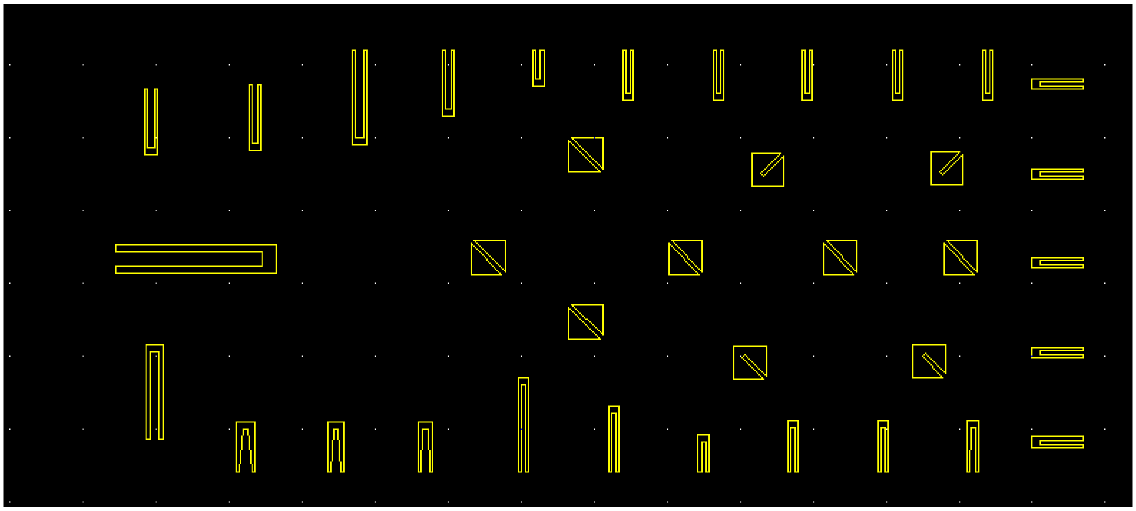

Figure 48. Rectangular Array of MEMS Beam Designs

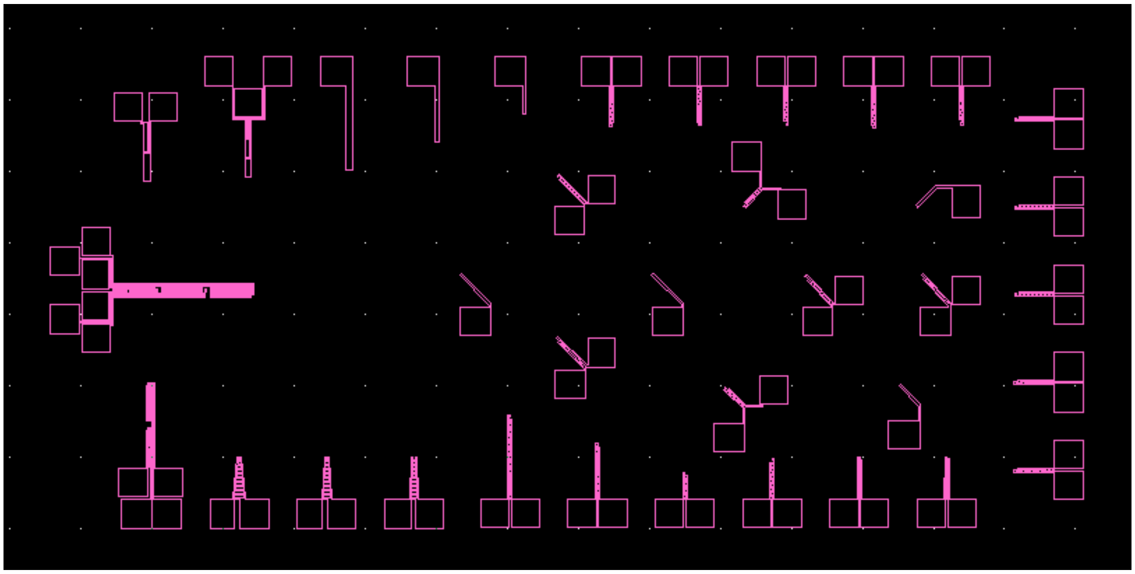

Figure 49. Rectangular Array of MEMS Top/Interdigitated Layer Electrode Designs

In general, although most beams were aligned horizontally, some beams were set on a diagonal, like those shown in Figure 50, to take advantage of different etching characteristics.

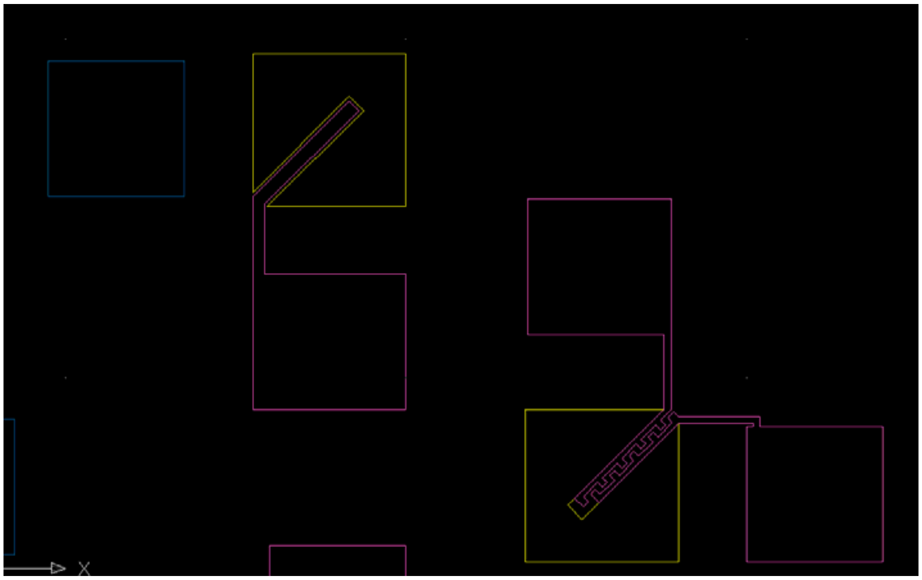

Figure 50. Diagonally-Oriented Beam Designs

Some tapered beams and clamp-clamped configurations were added to enhance the variability of the designs. In the electrode mask the number, spacing, and length of the electrodes was varied in order to test previous results of changes in tunability (section 4.2). Finally, some electrodes were segmented to include sensing and actuating portion (as shown in Figure 51) so that the same masks could later be used to fabricate self-oscillating devices.

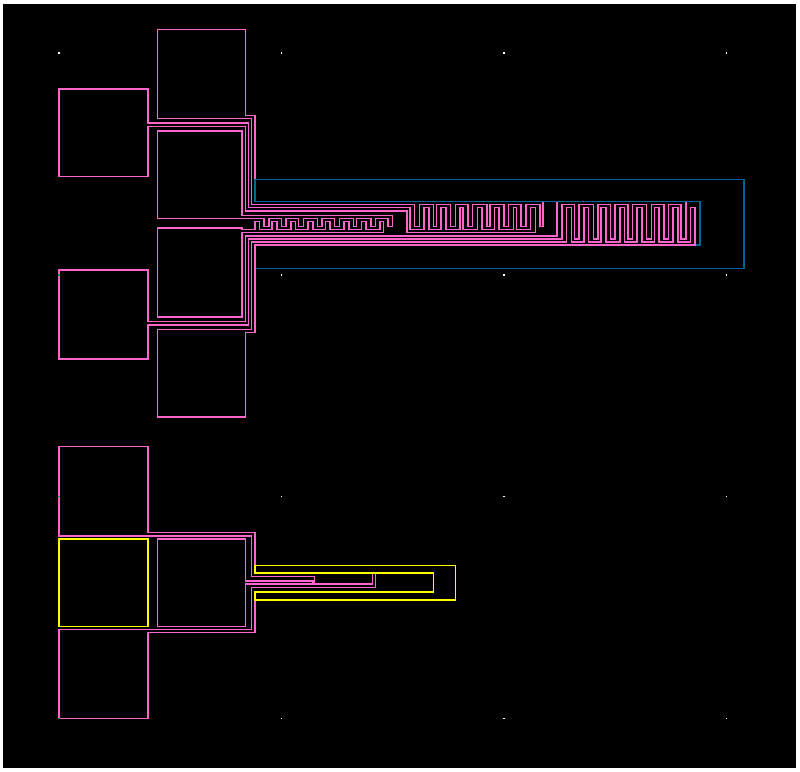

Figure 51. Layout for Self-Oscillating Resonant Devices

In addition to the main beams that were to be tested, a few basic cantilever arrays were added to the mask design to make it easier to measure piezoelectric material properties and see the effects of the stress. Specially designed alignment keys (Figure 52) were also incorporated to allow the electrodes to be properly aligned with the beams, and to provide an additional means for judging the resolution of the lithography.

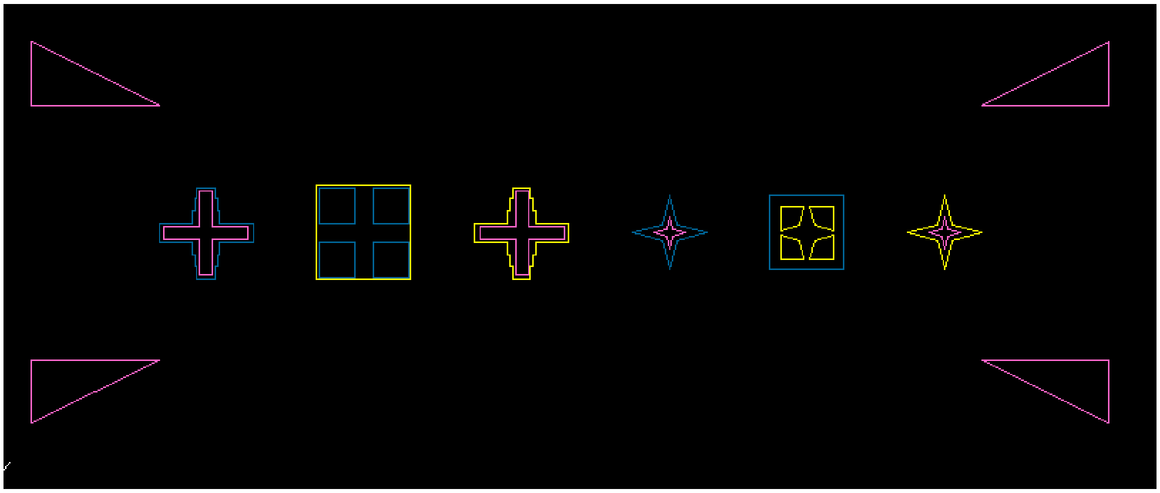

Figure 52. Layout for Alignment Keys Between all Three Layers

All layout drawings were made in AudoCAD 2002 and saved in .gds format. These files were then uploaded onto the computer connected to the Heidelberg DWL66 laser lithography writing system at Carnegie Mellon University, where they were converted to .lic files in Linux, the type readable by the system, and transferred to the DWL66 laser lithography machine.

The DWL66 is a high-resolution imaging system used for direct-write laser lithography. Patterns are made by exposing the necessary areas of photoresist to the laser and performing the same process of mask development and etching that are characteristic of wafer lithography processes. All three mask designs were patterned on the DWL66 system. Basic AZ400K developer was used for 1-2 minutes to develop the photoresist and chrome 7 etchant was used for 1 minute to etch the chrome. Alternating baths of acetone and isopropanol were used to remove the excess photoresist from the mask plates. When sticking was found to be a problem, the

MEMS ultrasonic agitator was used in attempt to eliminate the remaining resist: however, it did not seem to have much of an effect on the results. Since the excess photoresist did not appear to adversely effect the patterning of the devices, the no further cleaning processes were performed. Figure 53 shows microscope images of the mask patterns after development and etch.

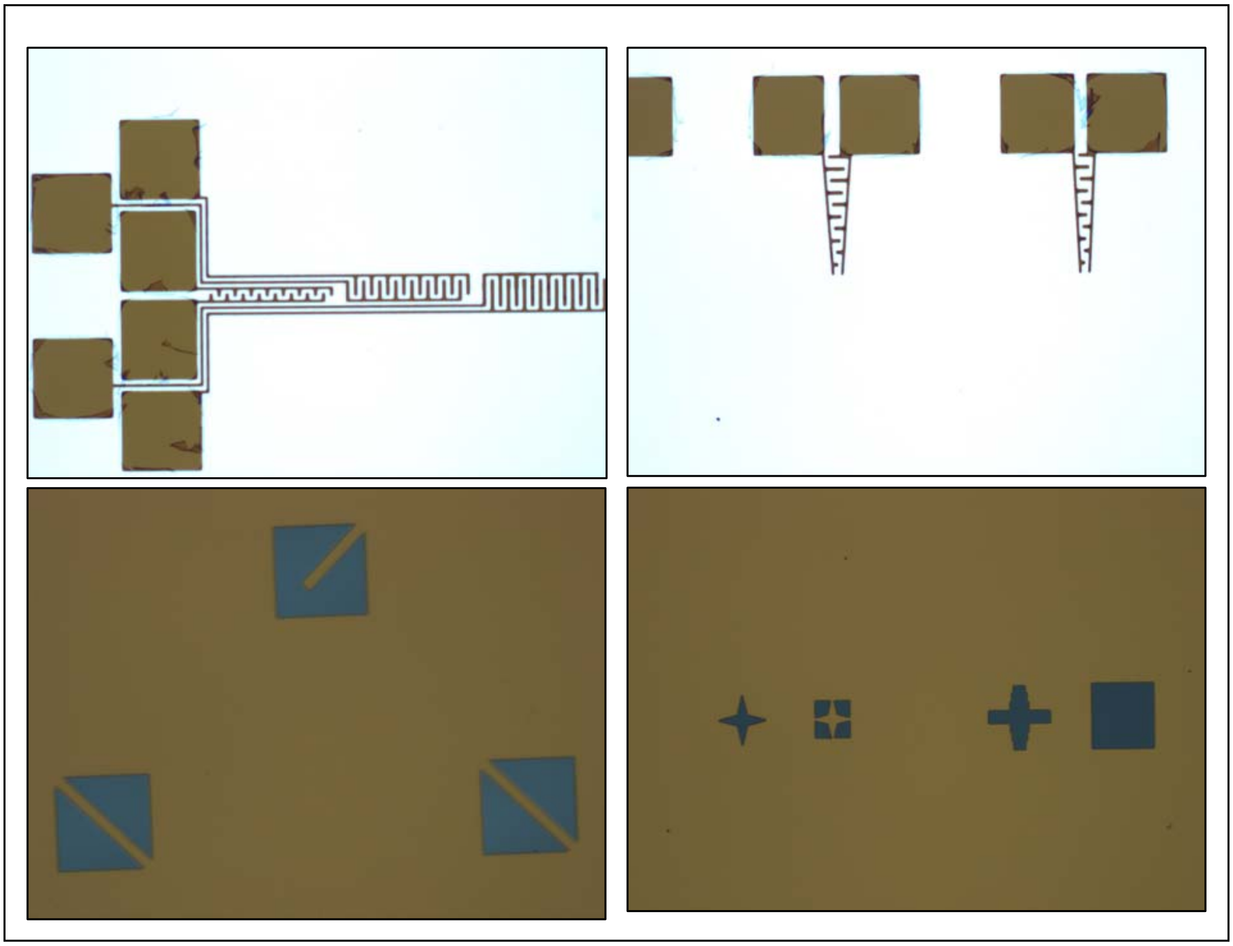

Figure 53. Microscope Images of Mask Features

5.3 DEVICE PATTERNING

Once a spin-coating process plan yielding satisfactory results of thin-film PZT had been realized and the necessary lithography masks had been designed and fabricated, the next step was to determine a method for patterning the layers of the device. This included the patterning of the original SiO_2/SiNx/SiO_2 layers, the new ZrO_2 and PZT spin-coated films, the to-be-deposited Cr/Au electrodes, as well as the release of the structures via silicon etching. It is important to note that in the beginning the choices for processing steps were made largely based on the availability of machinery here at Pittsburgh, as well as at neighboring, cooperative Universities. Consequently, some techniques, such as the Reactive Ion Etch (RIE) in BCl_3:Cl_2 used at MIT, which would be capable of patterning the SiO_2/SiNx/SiO_2/ZrO_2/PZT structure in a single RIE etch step, were not an option originally due to an inability to have PZT material in the RIE machines available. However, as further results were gathered, the pros of involving processing at other Universities were weighed, and additional process plans were developed accordingly.

5.3.1 Process Plan 1: ZrO2/PZT deposition on Pre-Patterned Wafers

As mentioned, since PZT could not enter the RIE machine, it became necessary to pattern the devices *before* the sol-gel deposition; thus, the following process plan, shown in Figure 54, was developed for the initial steps of the device fabrication in the first process plan.

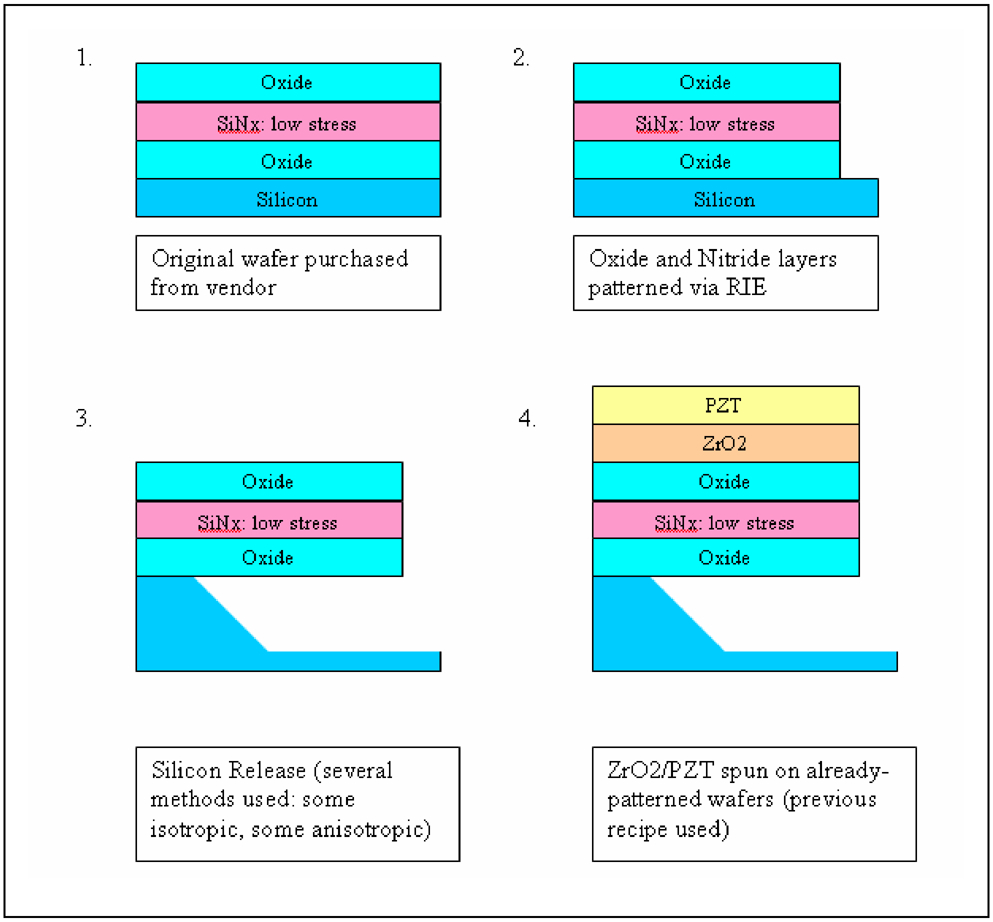

Figure 54. Initial Steps of Proposed Process Plan 1

5.3.1.1 SiO2/SiNx/SiO2 Patterning

For initial trials, the Unaxis ICP-RIE 790 was used to do the patterning of the oxide and nitride layers. After several trials, the following parameters were set for the etch process:

Table 12. Unaxis RIE Etch Recipe Parameters

		Flow %	Flow Rate (sccm)
Gas	CF_4	100	37
	O_2	50	4

Pressure	15 mT
Btm Temp	25 C

	RF1	RF2
Power	160 W	150 W

and a 7 minute and 40 second etch time was used. Microscope pictures corresponding to the devices at this stage in the process are shown in Figure 55.

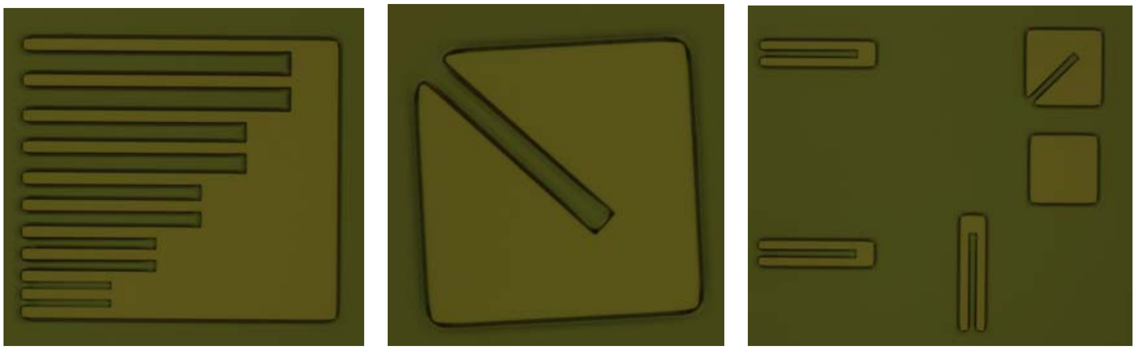

Figure 55. Microscope Images of SiO2/SiNx/SiO2 beams after RIE Etch

5.3.1.2 Structural Release

Next, it was necessary to release the beams. First, two wet etching processes were tried, again, due to ease of process availability. Later, a dry-etching process was employed for reasons that will be discussed below.

KOH Etch

The first of the wet-etching techniques used was an anisotropic KOH etch, the related pictures given in Figure 56. Prior to KOH etching, the samples were dipped in buffered oxide etchant (diluted HF) very briefly in order to remove any native oxides that had accumulated on the surface.

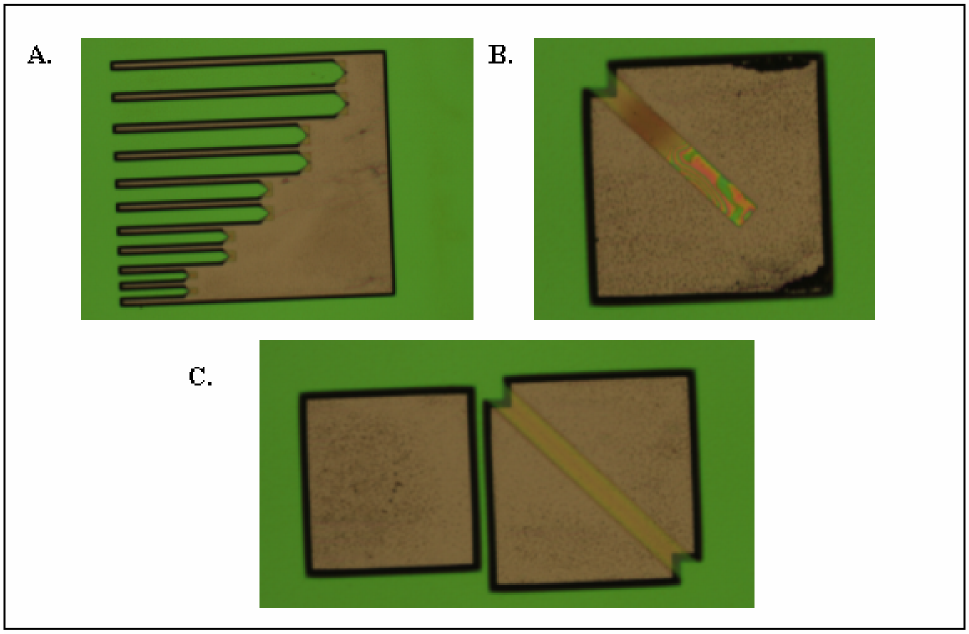

Figure 56. Microscope Images of KOH Etched Beams

Several important conclusions can be drawn from the photos. First, as can be seen in Figure 56 A, this etching technique is insufficient for releasing the horizontal beams, as it operates on the convex corner effect. Only the transparent areas at the end of the beams have been released after 15 minutes of KOH etching: consequently, a new technique would be necessary for releasing the majority of the structures. Next, it was determined that an etch time between 10-15 minutes was necessary for full release of the diagonal beams, since beams appeared to be insufficiently etched after 10 minutes, but fully released after 15 (Figure 56 C. shows a horizontal beam not fully released after 10 minutes of etching). Finally, a problem with sticking was observed in the clamped-free diagonal beams (Figure 56 B., where the color of the free end (stuck portion) differs drastically from that of the clamped end). It was hypothesized that the sticking was caused by a drying problem, where water droplets were succeeding in pulling the beams down to the bottom of the cavities, since an air gun was used to dry these samples. In order to prevent this, the first solution attempted was a quick-drying technique, where the samples were placed on a 200 C hot plate immediately following the etching process. However, even with the hot plate drying employed, the beams continued to stick to the bottom, and consequently, a dry-etching process was sought out.

HNO3:HF Etch

The second wet etch technique used to release the beams was an isotropic etch using HNO_3 and HF at a ratio of 84:16. Processing pictures from this trial, after 5 minutes of etching, are given in Figure 57.

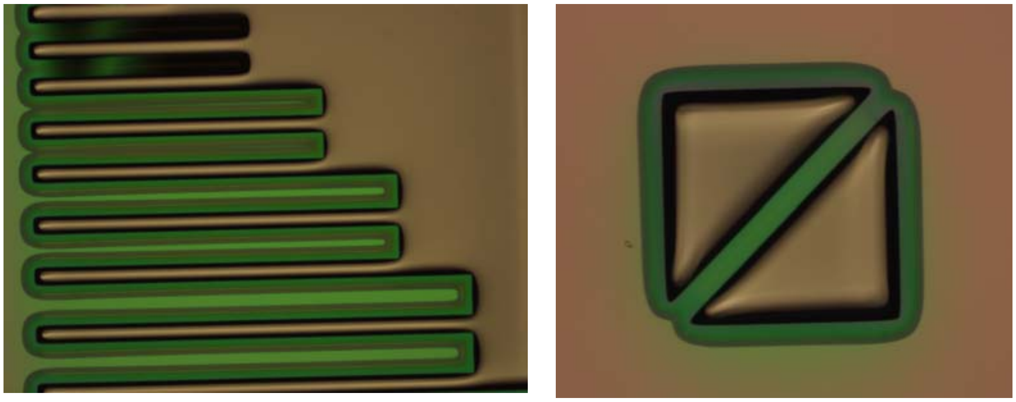

Figure 57. Microscope Images of HNO3:HF

It can be seen that the majority of these beams are not yet released: the smallest horizontal beams, which appear almost black, are closest to being fully undercut; consequently, a longer etch time would be needed if this technique were to be used to release the structures. From the macroscopic view, it can also be judged that the top layer of SiO_2 has been removed (a significant color change can be seen across the entire top layer of the wafer surface). This is due to the poor selectivity of HF between SiO_2 and Silicon. If this technique were to be further employed, it would be necessary to keep the photoresist layer on top in order to protect the top SiO_2 layer. However, despite the potential benefits that could be gained from these processing adjustments, it was assumed that the same sticking problem found to occur in the KOH etching would happen in this wet-etch process as well, and as a result, this technique was not further investigated.

XeF_2 Etch

Following these trials, it was determined that the XeF_2 etcher was the best possible alternative for releasing the structures. As an isotropic dry etch, it was hypothesized that the XeF_2 etching would be capable of solving the sticking problem, and would provide a means for effective release of the horizontal and diagonal structures simultaneously. The fact that XeF_2 also has high selectivity to photoresist and other structural layers, as well as a high etch rate for silicon, suggest that this technique should result in well-defined structures, deep etch cavities and efficient processing.

The process parameters for the first two trials of XeF_2 etching using the XACTIX XeF_2 etcher at Carnegie Mellon University are shown in Table 13. For these parameters, a "cycle" is defined as a sequence of the following steps: filling of the expansion chamber with the pressures set by the recipe, opening the valve to the main process chamber for the described etch time and purging the chamber.

Table 13. Process Parameters for XeF2 Etching

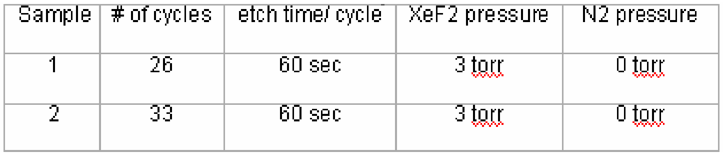

Sample	# of cycles	etch time/ cycle	XeF2 pressure	N2 pressure
1	26	60 sec	3 torr	0 torr
2	33	60 sec	3 torr	0 torr

Results were viewed under the scanning electron microscope (SEM) in order to best understand all of the properties of the XeF_2 etch.

Several important conclusions can be drawn from the SEM photos. To begin, it is evident that the XeF_2 did not prove to be a consistent isotropic etch. Figure 58 shows a beam undergoing XeF_2 etching and indicates the respective etch depths. The vertical etch distances are much larger than the lateral etch distances. Also, the left side of the beam is etched more than the right side of the beam. Additionally, the etch depths measured differed drastically from those expected. In Figure 58, the depths indicated were measured off of sample 1: a sample etched for 26 cycles of 60 seconds (26 minutes total). Similarly, the depth of sample 2 (etched for 33 minutes total) was measured to be approximately 29 microns. Since the documented etch rate of this etcher is 2 microns per minute for Silicon, it is evident that some condition was not as expected in the etching process, or that the documented etch rates were not accurate for the machine and the etching conditions used.

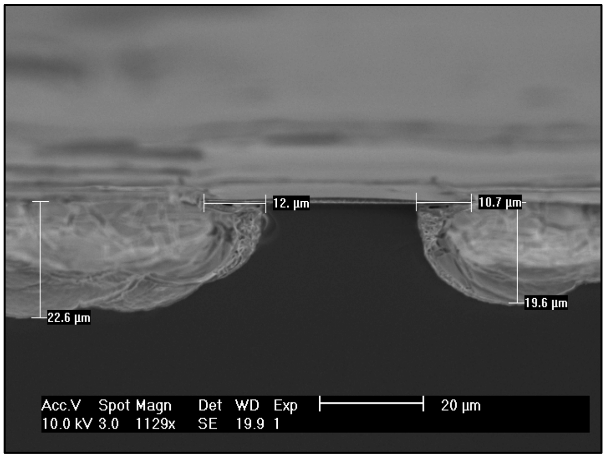

Figure 58. Indicated Etch Depths on Beam Not Fully Released

As a result of the unpredictable nature of the etch rates, many of the beams were not yet released (in particular, those on sample 1), despite what the etch rates indicated would be more than sufficient etch time. Figure 59 shows one beam of this nature, still attached at certain portions.

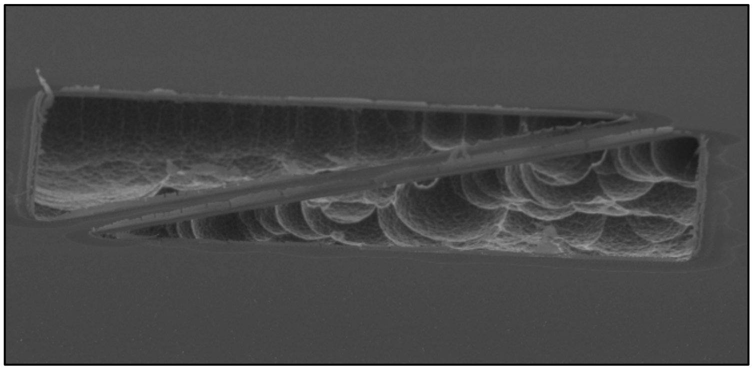

Figure 59. Not Fully-Released Beam

An additional problem which became evident through the SEM photos was that the top layer of SiO_2 was being attacked. This was visible though the delamination of SiO_2 around the outer edges of the beams and cavities (Figures 60 and 61).

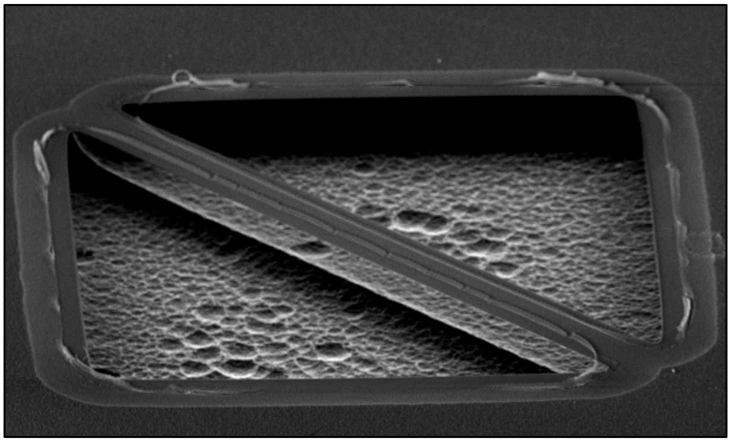

Figure 60. SiO2 Delamination Occurring in Clamped-Clamped Beam

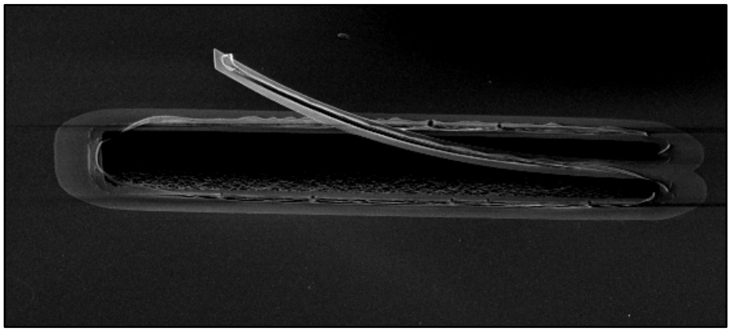

Figure 61. SiO2 Delamination Occurring in Clamped-Free Beam

Since the selectivity of XeF_2 to the SiO_2 was anticipated to be very high (2000:1 between SiO_2 and Silicon), and a layer of photoresist should have remained on top of the beams (selectivity between Silicon and photoresist was assumed so large it could be considered infinite), the cause of the delamination is not easily explained. It is possible that this problem was occurring earlier, at the RIE stage of processing, and earlier photos of PZT coated on the wet-etched samples showing similar (although, less drastic) inconsistencies in depth would support this conclusion; however, again, the photoresist was expected to be a sufficient masking for the structural layers, and thus the results are not conclusive. It is also possible that overexposure of the wafer during photoresist development could have led to areas with insufficient photoresist masking at the corners of the patterns; however, this hypothesis was not investigated. In any case, the delamination presented a serious problem, since removal of a large portion of the oxide top layer would most definitely cause problems with adhesion and film homogeneity of future layers, and could present additional concerns about the residual stress in the beams. Consequently, for future process plans, a process where the SiO_2 was covered with additional layers (besides the photoresist) before its patterning and structural release would be seen as an advantageous design, helping to preserve the integrity of the beam.

Many of the beams that were fully released (these were found on sample 2, etched for a longer period of time) showed an additional problem of curling. An array of curled beams is shown in Figure 62.

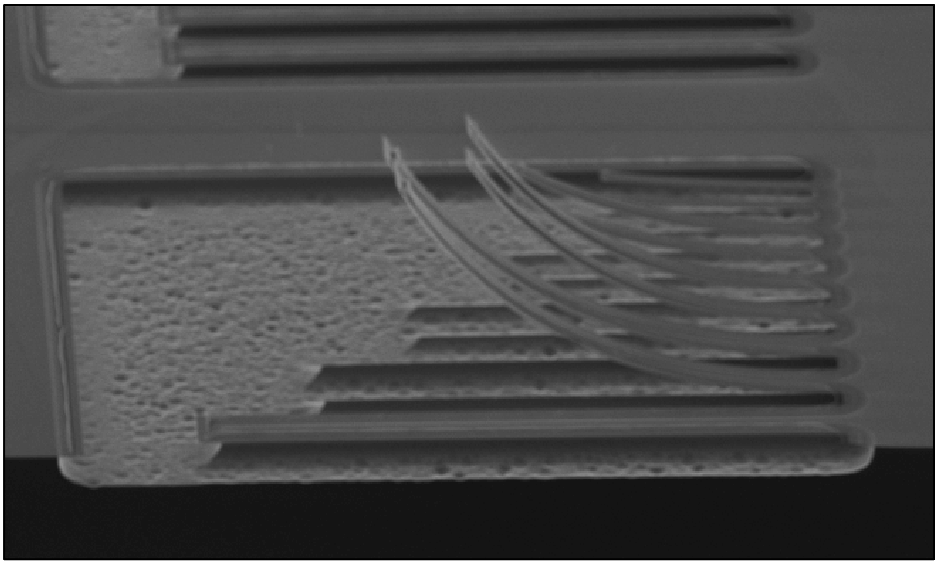

Figure 62. Array of Curled Beams

The most logical conclusion for such a result would normally be a large residual stress in the layers of the wafer: however, the fact that the radius of curvature is so different between the beams (particularly even between the beams on the same array) is not consistent with this explanation. The results caused suspicion that there may be problems with the nature of the thin films deposited on the wafer to this point, or that the partial removal across the oxide layers was causing an unbalance in the residual stress in the beams. The curling also presented some potential problems for future processing, since it would be difficult (or impossible) to deposit additional layers evenly across the highly-curled beams, and thus the opportunity to do additional layer depositions (ZrO_2, PZT, electrode) on top of non-released structures was considered to be another desirable characteristic for future processing plans. In terms of future processing, it was hoped that depositing as many of the device layers as possible prior to the structural release would help to eliminate potential causes of the curling and allow for the best homogeneity of the film

5.3.1.3 Coating of ZrO2 and PZT Films

In order to get an idea of whether or not spin-coating the ZrO_2 and PZT layers on top of the already patterned devices was possible, despite the current limitations in the prior processing, the KOH and XeF_2 etched samples were used for initial spin-coating tests. The Scanning Electron Microscope (SEM) was used to view these results to obtain the best insight into the success of the fabrication, and the pictures of these structures are shown in Figures 63 through 68.

On KOH Etched Samples

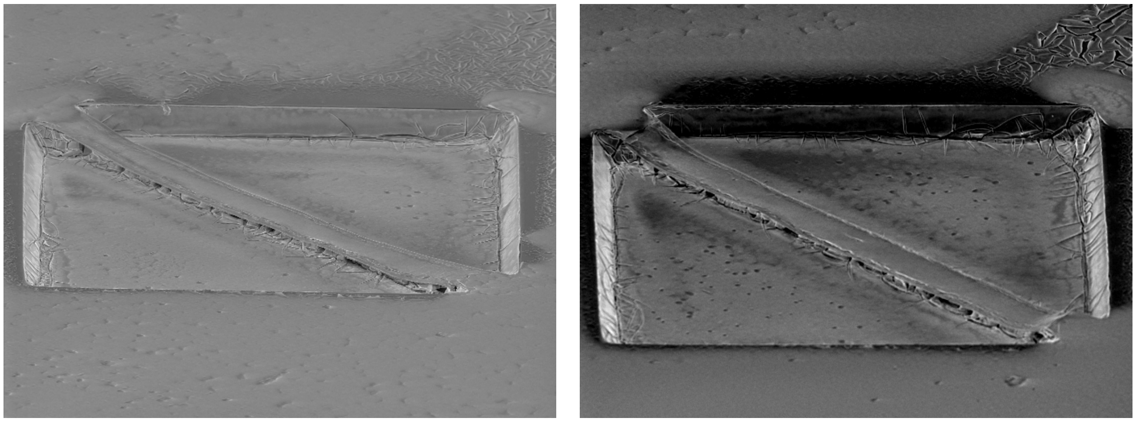

Figure 63. SEM Pictures of PZT Coated Structures

The first round of trials were done on the KOH samples (due to their availability). As the first pictures show (Figure 63), the bulk of the PZT coverage looks good across the length of the beams. The majority of the cracking and large variation in depth are found at the corners of the cavities, and thus should not be a problem for future device fabrication. A new sticking problem was shown to exist, however, where even the clamped-clamped beams were stuck to the bottom of the cavities (likely from the PZT getting underneath the beams). It was hoped that etching a deeper cavity (which is easier to do with the XeF_2 etching) would help to eliminate this new development.

At closer views, the PZT coverage of the beams still appeared to be of good quality (Figure 64). Some cracking was occuring at the end of the beams, and at this stage, it was hypothesized that this was also due to the sticking problem and would also be eliminated with the XeF_2 etch.

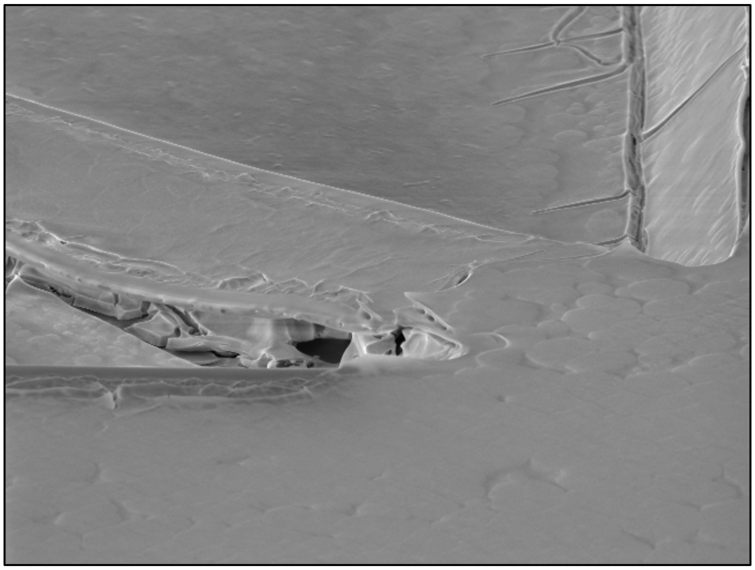

Figure 64. SEM Images of PZT Coated Beam: Close-Up View: Cracking

SEM images verified earlier hypotheses that the clamped-free beams were sticking to the bottom of the cavities after the wet-etch procedures. In Figure 65, it is clear that the beam was stuck prior to the sol-gel deposition, and that ZrO_2 and PZT layers are coated over the pre-stuck beam.

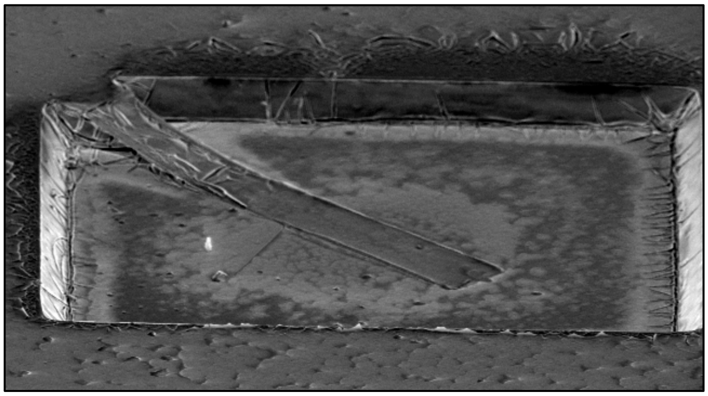

Figure 65. SEM Images of PZT Coating Over Pre-Stuck Beam

Figure 66 shows the results of the PZT coating over the horizontal, not-fully-released beams. It can be seen that the majority of covereage is good, but that there is some depth variation between the outer edge and the inside of the beam, as well as at the beam tips. It is possible that this is a result of the delamination problem: however, since SEM pictures were not taken prior to this deposition, it is impossible to say conclusively. Regardless, it was thought at this point that the covereage should be good enough to deposit the additional electrode layers on top, thus enabling the continuation of device fabrication.

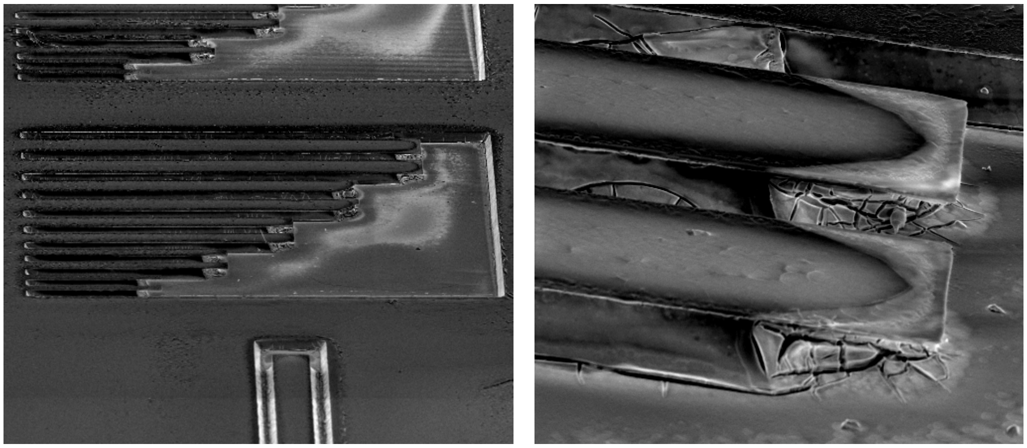

Figure 66. PZT Coating on Horizontal Beams

Finally, a depth measurement was taken in order to get a best judgement of the size of the cavities in the KOH etching case (Figure 67). The SEM indicated that the cavities were approximately 13.8 microns deep, a result that coincided well with similarly fabricated devices measured by the Wyco optical profiler (here, cavities were measured to be 13.3, but films had not undergone the additional spin coating and annealing steps of the ZrO_2 and PZT films). As previously mentioned, future cavities would be made much larger, both to help with the aforementioned sticking and cracking problems in the diagonal beams, as well as to allow for fully released structures in the horizontal and vertical beams using the dry, isotropic XeF_2 etch.

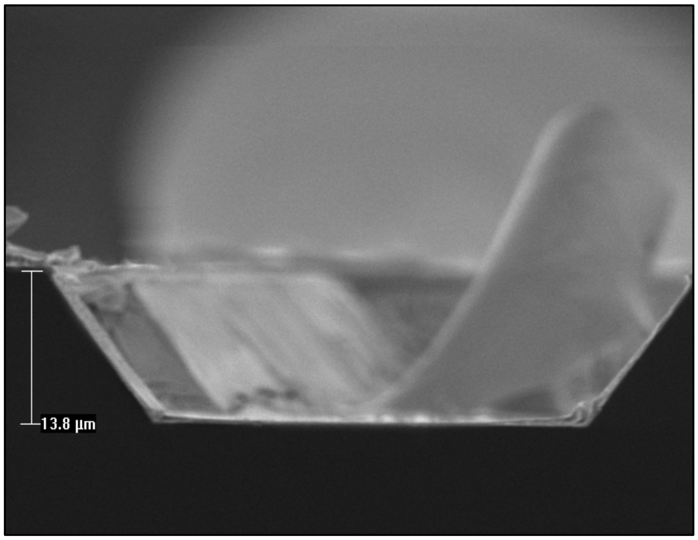

Figure 67. Depth Measurements of Silicon-Etched Cavity

On XeF2 Etched Samples

Despite the negative findings of the XeF_2 etch (delamination, non-isotropic etching, unpredictable etch rates), the processing was continued to test the effectiveness of patterning these devices with ZrO_2 and PZT, specifically to see if the additional sticking problem remained with the deeper cavities and dry etching used. Primarily the clamped-clamped beams were examined, since, as noted, it was assumed that it would be difficult to achieve uniform coating on the already-curled beams. Figure 68 shows the best and the worst of the results from these trials, both taken from a piece of sample 2 coated with a layer of ZrO_2 and two layers of PZT.

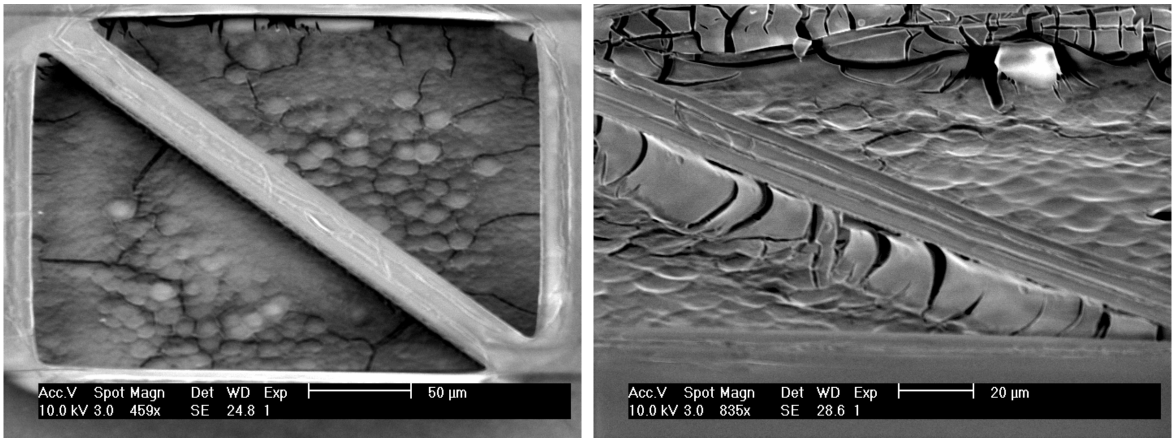

Figure 68. Best and Worst Case for Spin Coating on Already Released Clamped-Clamped beams

It can be seen that, in some cases, the PZT was able to effectively coat the top without causing accumulation under the beam. Although the coating was not consistent across the entire beam, the photos taken before the PZT deposition revealed this to be a problem of the aforementioned delamination of the SiO_2 layer rather than a problem with the actual PZT processing. In other cases, however, (the majority of the samples) the PZT was found to stick to the sides of the beam and connect the device to the cavity. This presented a problem for the future oscillation purposes of the cantilevers.

5.3.2 Process Plan 2: With RIE BCl_3:Cl_2 Step after Electrode Patterning

Considering the implications of all of these results, a new process plan was developed for fabrication, given in Figure 69.

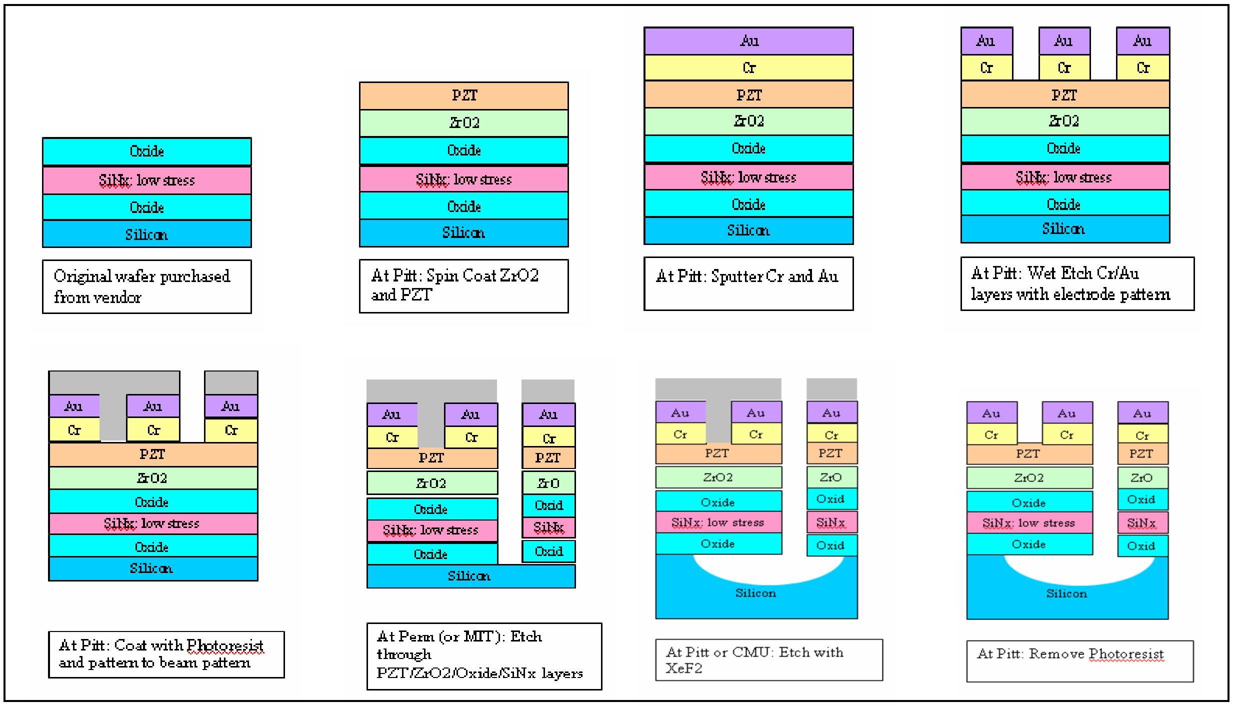

Figure 69. Proposed Process Plan 2: RIE BCl_3:Cl_2 Step after Electrode Patterning

Implementing this process, it would be necessary to have one step done outside of Pittsburgh (the dry etching of the SiO_2/SiNx/SiO_2/ZrO_2 and PZT layers); however, considering the problems encountered with the previous methods of processing, the cons of other, alternative processing routes, and the potential benefits this technique offers, it was decided that the benefits outweighed the costs. Potential benefits include:

- Only one step of RIE etching required to pattern five structural layers
- No wet etch processing steps after structural release (eliminates sticking problem)

- Best quality of PZT (can spin coat on plane wafer surface, thus eliminating problem of coating on curled beams and accumulation of material under the beam)
- Elimination of delamination of SiO_2 problem (several layers on top of SiO_2 during photoresist patterning, RIE, and XeF_2 etch steps)
- Best chance for stress balance (no delamination and full coverage of all materials should allow for best stress balance before structural release)

5.3.2.1 Electrode Deposition/Patterning

For the proposed process plan, once the ZrO2 and PZT films had been processed, the next step was the sputtering of the Au and Cr films. The ISE-OE-PVD-3000 DC and RF Magnetron Sputtering System were used for these depositions.

A 300Å/minute sputtering rate was approximated for both materials with the wafer set at 80 cm away from the target. Since the Chromium was present only to aid in adhesion, only a very thin layer was needed. Chromium sputtering was performed for approximately 30 seconds with the power set at 50W. For the Gold layer, a 7 minute sputtering time was used at a power of 100W, estimated to provide an electrode of approximately 2100 Angstroms.

To pattern these layers, AZ4110 photoresist was used with an intermediate layer of spin coated HMDS, used to promote adhesion. A spin coat recipe of 10 seconds at 500 rpm followed by 30 seconds at 3000 rpm was used for both the HMDS and the photoresist. An exposure time of 1.3 seconds with hard contact was employed in the lithography.

After the photoresist had been developed, the Au and Cr layers were etched using a recipe of $HCl:HNO_3:H_20$ at a ratio of (3:1:4). Using this solution, an etch time of about a minute was needed to fully pattern the electrodes. Figure 70 shows microscope images of the Cr/Au electrodes patterned on top of the PZT films.

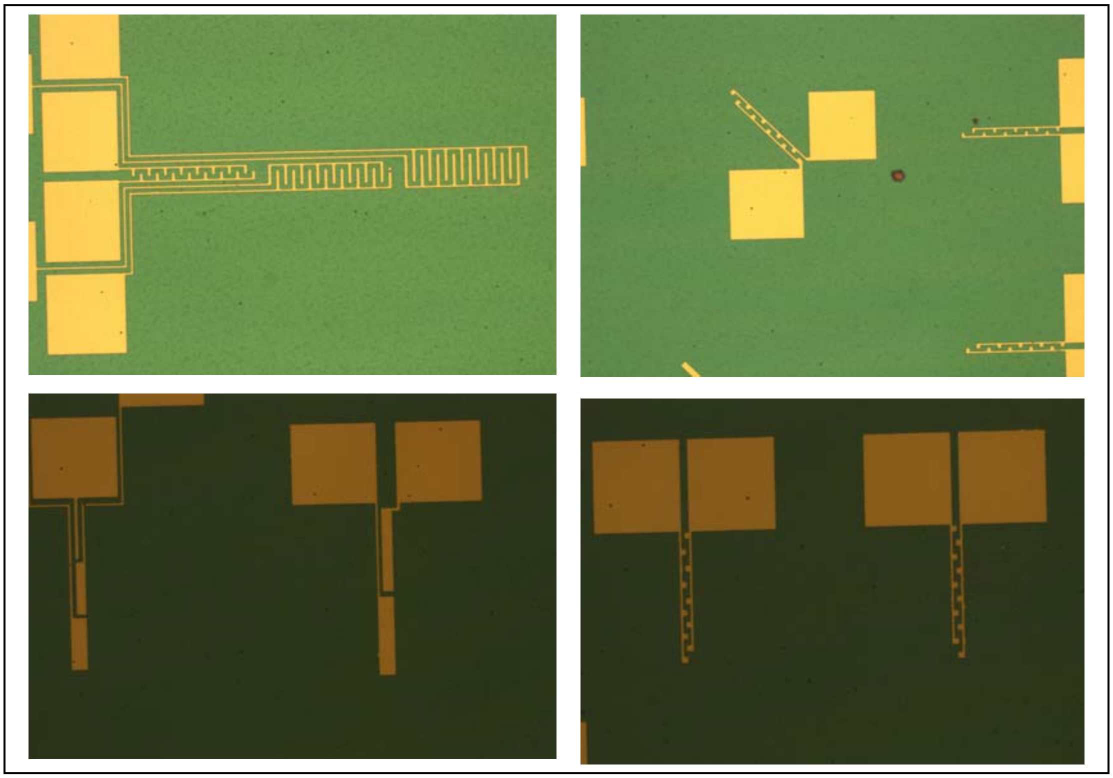

Figure 70. Electrodes Patterned on PZT Surface

5.3.2.2 Beam Lithography/Patterning

The final step in this process plan before the wafers were to be sent to MIT was the patterning of photoresist for the lithography of the beams. It was necessary to use a thick photoresist for the masking layer in this process since the selectivity between the photoresist and the device layers in the BCl_3:Cl_2 dry etch is not extremely high. Thus AZ4620 was employed as the resist which, when used with the same 500 rpm: 10 seconds, 3000 rpm: 30 seconds spin recipe, estimates a resist thickness of approximately 10 microns.

A longer exposure time was needed in order to pattern the thicker photoresist, but it was important that the exposure not be overdone, less the patterns loose their well-defined features. A time of 18 seconds was found to give satisfactory results for the patterning, and about 1 minute was needed to fully develop the resist. Microscope images following the development of the beam pattern on top of the electrodes are given in Figures 71 and 72.

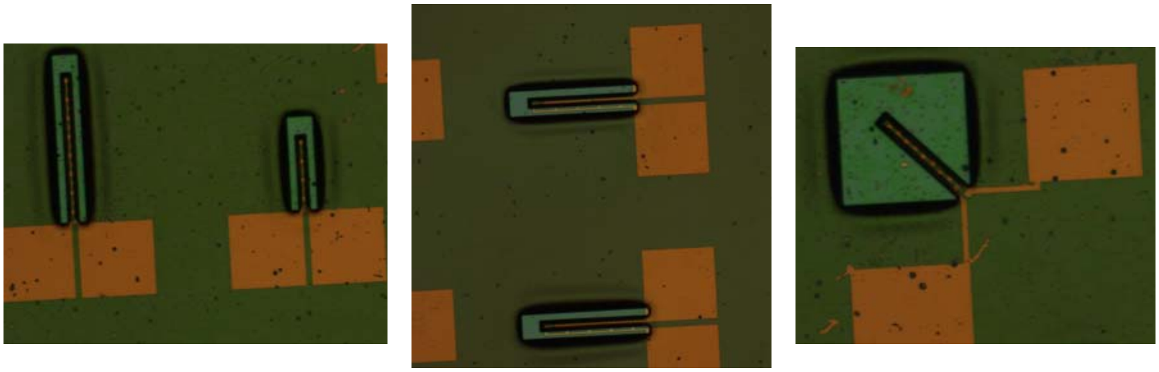

Figure 71. Beam-Patterned Photoresist on Electrode-Patterned Wafers

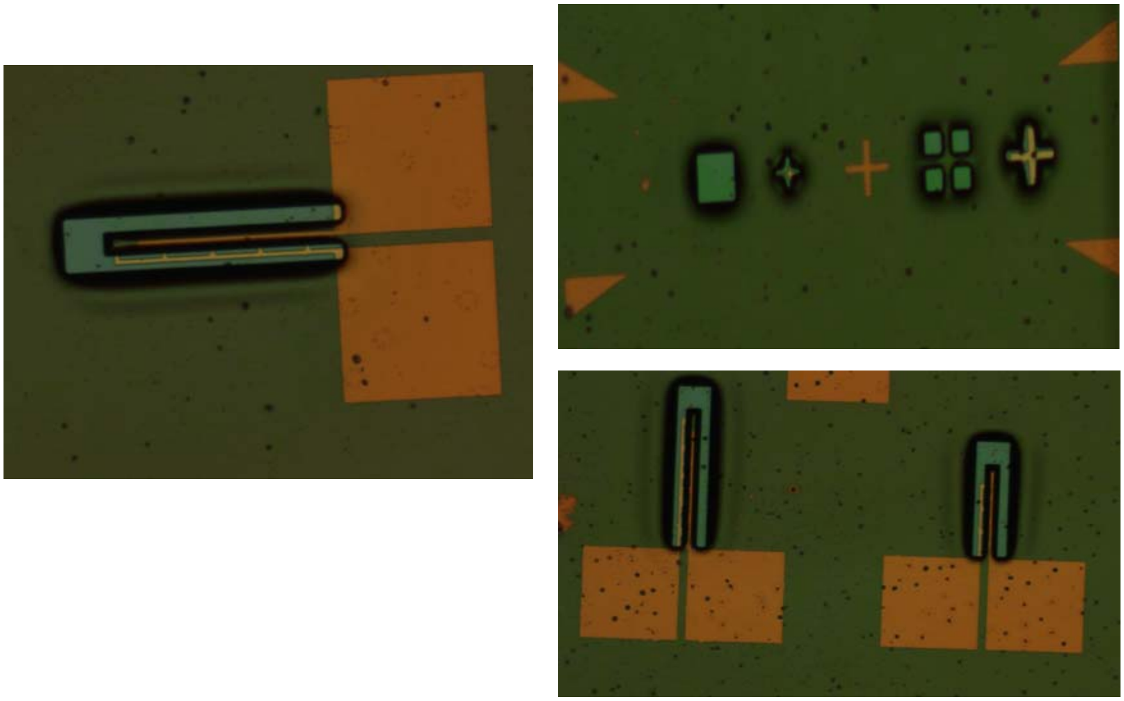

Figure 72. Misalignment in Beam-Patterned Photoresist on Electrode-Patterned Wafers

In the first set of images, the patterns appear fairly well-aligned. These are the beams which are located closest to the wafer edge. However, as one looks at beams closer to the wafer center, it can easily be seen that the beams are not perfectly aligned and that it is likely that many of the electrodes would be lost in future patterning. The misalignment is due to difficulty involved in using the alignment key. Micron-scale alignment can be fairly difficult in general, and since the alignment keys were designed originally to have the beam layer patterned prior to the electrode layer, further difficulties were encountered. In addition, an alignment key which had a wider open area to center on would have aided in aligning the beam patterns and electrodes. Despite the misalignment, this wafer was sent to MIT for the dry etch processing in hopes that some of the better-aligned devices would still be usable.

5.3.3 Process Plan 3: With RIE BCl_3:Cl_2 Step before Electrode Patterning

To provide a possible aid to this problem, the process plan proposed in Figure 64 was slightly altered to move the RIE of the structural layers before the deposition and etching of the electrodes: the corresponding updated process plan in shown in Figure 73.

With this process plan, the beams would be patterned before the electrodes, as originally planned, hopefully improving the alignment between layers by utilizing the alignment keys in the way they were originally designed. All of the advantages set forth by the process plan in Figure 69 would also remain true.

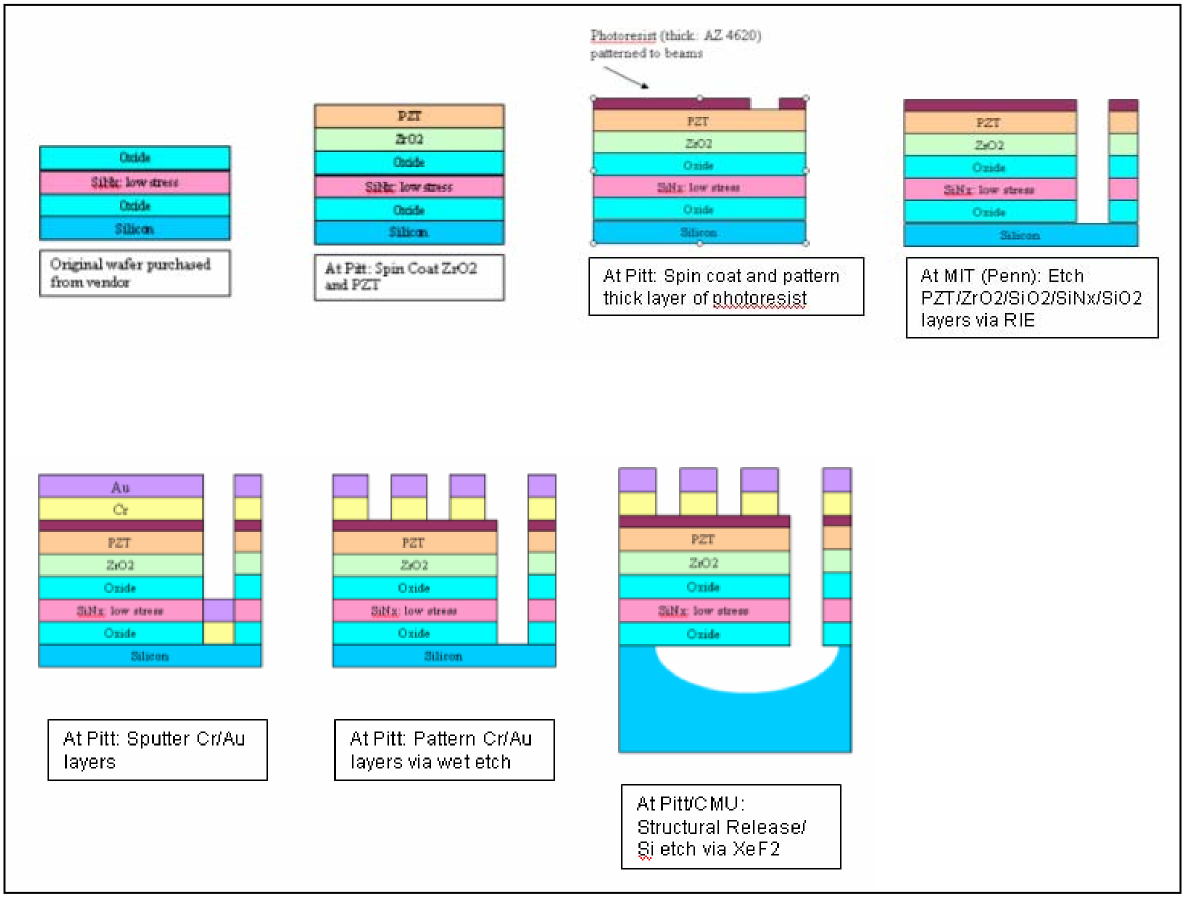

Figure 73. Proposed Process Plan 3: RIE BCl_3:Cl_2 Step before Electrode Patterning

Again, the thick photoresist (AZ 4620) was used to pattern the photoresist mask for the beam layers and the same 18 second exposure time and 1 minute development time were employed. Microscope images following this processing are shown in Figures 74 and 75, corresponding to trial 8 of PZT (later repetitions having some degree of hillocks, as is visible in the images).

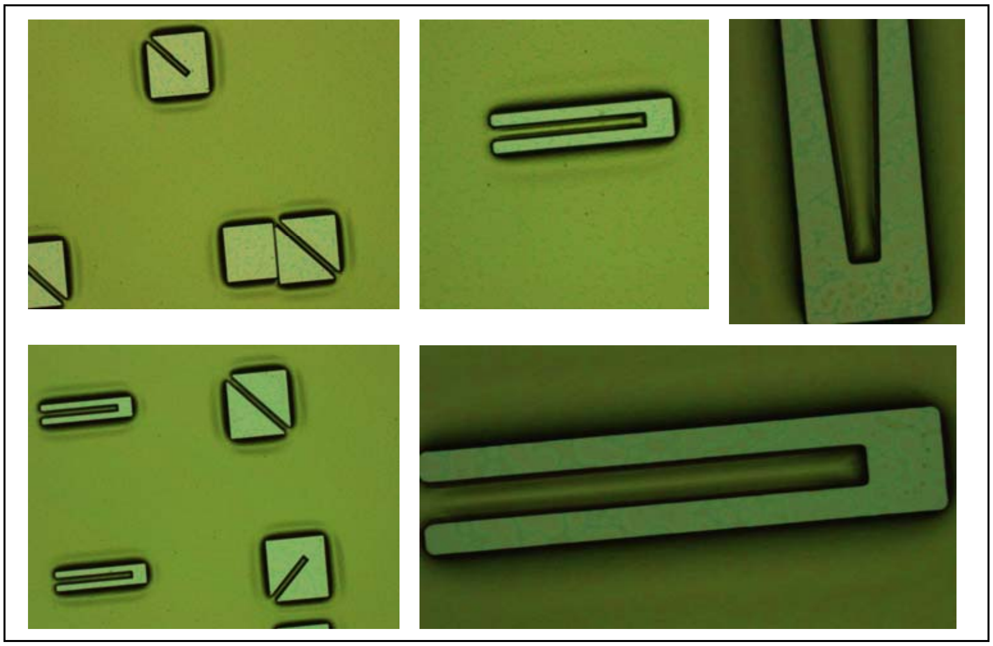

Figure 74. Photoresist Beam Pattern on PZT Surface

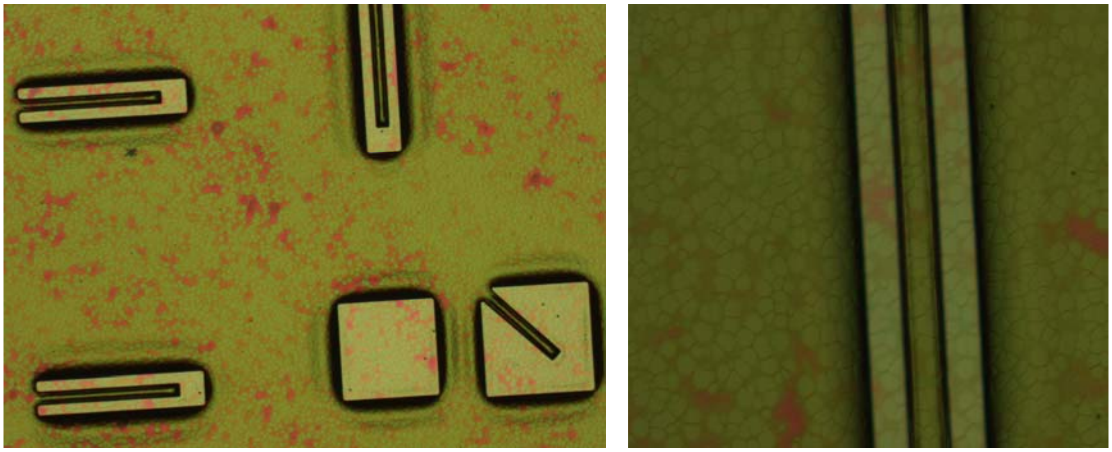

Figure 75. Photoresist Beam Pattern on PZT Surface with Some Hillocks

Three of these wafers, as well as the first wafer with the pre-patterned electrodes, were sent to MIT for RIE etching. This processing has not yet been completed.

6.0 CONCLUSIONS

This work discussed the design and fabrication of tunable MEMS piezoelectric resonators. To begin, previous background in MEMS resonators was discussed, particularly with respect to tuning, actuation, and available piezoelectric modes. A background on piezoelectric materials was also provided, specifically focusing on their applications in MEMS fabrication. The benefits of PZT in MEMS tunable resonator designs were discussed, and the most commonly utilized MEMS processing techniques were mentioned.

From this point, theoretical models were developed for bending beam, SAW, and FBAR resonators and discussion of how different variables of their designs affected the resonant frequencies and available tuning were explained. For the bending beam model, it was found that PZT, interdigitated electrodes with minimum electrode length and spacing concentrated on the clamped end of the beam offered the best results for changing the stiffness of the system. In the cases of the SAW and FBAR devices, the relative thicknesses were shown to be unimportant in determining the relative tunability, but were influential in calculations of the nominal resonant frequency of the device (the thicker the layers, the lower the resonant frequencies). PZT layers used as the tuning portion of the resonators were found to give the most achievable stiffness change, and different materials could be used in the structural and tuning layers in order to maximize the benefits of various material properties with respect to resonant frequencies, quality factors, manufacturing concerns etc.

For the fabrication portion of this work, the necessary steps for processing MEMS PZT tunable bending beam resonators were developed. Most of this investigation focused on research into the best processes for depositing and annealing of ZrO_2 and PZT films and the most effective etching techniques for all of the device layers (Si, SiO_2, SiNx, ZrO_2, PZT, Cr and Au). In the end, a process which produced the most repeatable results of minimized cracks and hillocks, while maximizing the quality of the PZT film's piezoelectric properties (as gauged by XRD testing) was selected to be the best technique for deposition and annealing of ZrO_2 and PZT films (Figure 35). Also, a process flow for the fabrication of the entire device which had the most potential for quality films, elimination of sticking, high-quality, uniform PZT, good alignment and the best stress balance across the wafer was determined (Figure 73). Further work must be done to complete the fabrication of testable devices using this technique.

7.0 FUTURE WORK

Additional work is necessary to complete the fabrication of the MEMS bending beam resonators. While all the required processing steps have been performed and tested individually, successful devices must still be fabricated utilizing this entire process flow in order to validate the results determined in the theoretical models.

In the devices already made and sent to MIT with the pre-patterned electrodes, XeF_2 release must be performed, and the photoresist masking layer should be removed. At this point, poling of the PZT films must be done in order to be able to utilize the piezoelectric properties of the film. Upon completion of this step, these devices will be ready to be actuated and tested for their resonant properties and available tuning.

In the devices already made and sent to MIT without the pre-patterned electrodes, the electrode layers must first be sputtered and patterned, after which the XeF_2 release, photoresist removal and poling can take place. These devices can then also be tested and compared with the theoretical results.

In addition, some further concerns drawn out by the results of the theoretical modeling should be addressed. For the bending model, this would primarily be the determination of the correlation between the applied voltage and the penetration of the electric field within the piezoelectric. In the SAW model, establishing the correct method (or the availability of an equation) for determining the particle velocity at the surface of the substrate would help in pinpointing design limitations. For all of the resonators, additional design parameters, particularly those important to resonator design (such as the quality factor), which are not addressed in this study could be investigated to make further judgments about the pros and cons of respective piezoelectric materials.

Finally, upon successful fabrication and testing of the piezoelectric bending beam devices, designs could be drawn up for the fabrication of SAW and FBAR tuning devices. Since much of the fabrication steps (deposition of piezoelectric and electrode layers, mask making, etching of the designs etc.) would be the same between these designs and the bending devices, it should be relatively straightforward to process these additional resonators. If all three resonator types (bending, SAW and FBAR) could be successfully manufactured, this would enable the application of the shunt capacitor tuning concept across a significantly large portion of the established frequency spectrum, maximizing its usability and versatility in the MEMS resonator market.

BIBLIOGRAPHY

Abe, T. (1995). *Fabrication Technologies for a Microelectromechanical Volumetric Flow Sensor*. dissertation, Carnegie Mellon University, Pittsburgh, PA.

Abe, T. & Reed, M.L. RF-Magnetron Sputtering of Piezoelectric Lead-Zirconate-Titanate Actuator Films Using Composite Targets. (1994). *IEEE Micro Electro Mechanical Systems An Invesitgation of Micro Structures, Sensors, Actuators, Machines and Robotic Systems, 1994, Oiso, Japan*. New York, NY, USA: IEEE.

Adams, S.G., Bertsch, F.M., Shaw, K.A., Hartwell, P.G., Moon, F.C., & MacDonald, N.C. (1998). Capacitance Based Tunable Resonators, *Journal of Micromechanics and Microengineering*, v 8 (1), p 15-23.

Adams, S.G., Bertsch, F.M., Shaw, K.A. & MacDonald, N.C. (1998). Independent Tuning of Linear and Nonlinear Stiffness Coefficients, *Journal of Microelectromechanical Systems,* v 7 (2), p 172-180.

Beeby, S.P. & White, N.M. (2000). Thick-Film PZT-Silicon Microemechanical Resonator. *Electronics Letters*, v 36 (19), p 1661-1662.

Chen, Q. & Wang, W. (2006). The Effects of a Passive Layer and External Electric Impedance on the Frequency Characteristics of Thin Film Bulk Acoustic Resonators (FBAR). *To appear in IEEE.*

Clark, W.W. (2000). Vibration Control with State-Switched Piezoelectric Materials. *Journal of Intelligent Material Systems and Structures*. v 11 (4), p 263-71.

Cost Effective Equiptment (2006). *Spin Coat Theory*. Retrieved April 20, 2006, from http://www.cise.columbia.edu/clean/process/spintheory.pdf.

Cross, E. (2004). Material's Science: Lead-Free at Last. *Nature*. v. 432, p 24-25.

Dai, C-L., Xiao, F-Y., Lee, C-Y., Cheng, Y-C., Chang, P-Z., & Chang, S-H. (2004). Thermal Effects in PZT: Diffusion of Titanium and Recrystalization of Platinum. *Materials Science & Engineering A (Structural Materials: Properties, Microstructure and Processing)*, v A384 (1-2), p 57-63.

Department of Defense. (1996). *Special Technology Area Review on Frequency Control Devices*. Washington, D.C.: Office of the Under Secretary of Defense Acquisition and Technology.

Dewan, N., Tomar, M., Gupta, V. & Sreenivas, K. (2005). Temperature stable $LiNbO_3$ Surface Acoustic Wave Device With Diode Sputtered Amorphous TeO_2 Over-Layer, *Applied Physics Letters,* v 86 (22), p 223508.

Du, J. & Harding, G.L. (1997). A Multilayer Structure for Love-Mode Acoustic Sensors, *Sensors and Actuators*, v 65 (2-3), p 152-59.

ERO Frequency Information System. (2006). *ERO Frequency Information System*. Retrieved April 20, 2006, from http://www.efis.dk/search/general;jsessionid=6E971041EB718F7261A1AD4897C80789.

Francombe, M.H. & Krishnaswamy, S.V. (1990) Growth and Properties of Piezoelectric and Ferroelectric Films. *Journal of Vacuum Science & Technology A (Vacuum, Surfaces, and Films)*, v 8 (3), p 1382-90.

Harvey, E.C. (1997). Laser Micromachining. *IEEE Colloquium on Microengineering Technologies and How to Exploit Them, 1997,Birmingham, UK*. London, UK: IEEE.

Hendrickson, M., Su, T., Trolier-McKinstry, S., Rod, B.J., & Zeto, R.J. (1996). Processing of PZT Piezoelectric Thin Films for Microelectromechanical Systems. *Proceedings of the 10th IEEE International Symposium on Applications of Ferroelectrics, 1996, East Brunswick, NJ.* New York, NY, USA: IEEE.

IEEE. (1987). *IEEE Standard on Piezoelectricity,* The Institute of Electrical and Electronics Engineers, 1987.

Ippolito, S.J., Kalantar-Zadeh, K., Trinchi, A., Wlodarski, W. & Tobar, M. (2003). Layered SAW Nitrogen Dioxide Sensor Based on a ZnO/36 YX $LITaO_3$ Structure With Selective Layer. *Proceedings of SPIE - The International Society for Optical Engineering*, v 5116 (2), 904-11.

Ishak, W.S., Chang, K-W, Kunz, W.E and Miccoli, G. (1998). Tunable Microwave Resonators and Oscillators Using Magnetostatic Waves, IEEE Transactions on Ultrasonics, Ferroelectrics, and Frequency Control, v 35 (3), p 396-405.

Jeon, K., & Lee, L.P. (2003). A Novel Fabrication Method of a Vertical Comb Drive Using a Single SOI Wafer for Optical MEMS Applications. *12th International Conference on Solid State Sensors, Actuators and Microsystems, 2003, Boston, MA.* Piscataway, NJ, USA: IEEE.

Joachim, D. (2003). Characterization of Selective Polysilicon Deposition for MEMS Resonator Tuning. *Journal of Microelectromechanical Systems,* v 12 (2), p 193-200.

Jeon, Y.B., Sood, R., Jeong, J.-h, and Kim, S.-G. (2005). MEMS Power Generator with Transverse Mode Thin Film PZT. *Sensors and Actuators, A: Physical*, v 122 (1), p 16-22.

Johnson, R.A. (1983). *Mechanical Filters in Electronics.* USA: John Wiley & Sons.

Kielczynski, P.J., Pajewski, W. & Szalewski, M. (1989) Shear-Horizontal Surface Waves on Piezoelectric Ceramics with Depolarized Surface Layer, *IEEE Transactions on Ultrasonics, Ferroelectrics, and Frequency Control*, v 36 (2), p 287-93.

Kim, S.G. (2004). *Piezoelectricity*. Retrieved April 20, 2006, from http://ocw.mit.edu/NR/rdonlyres/Mechanical-Engineering/2-76Fall-2004/972E0CFB-827D-4CAD-85E6-99EEBD74AFF1/0/lecture_7prt2.pdf.

Kinoshita, Y., Kubota, S., Takeda, S. & Nakagoshi, A. (1990). Planar Resonator and Integrated Oscillator Using Magnetostatic Waves, *IEEE Transactions on Ultrasonics, Ferroelectrics, and Frequency Control*, v 37 (5), p 457-463.

Kolesar, E.S., Allen, P.B., Howard, J.T., Wilken, J.M., & Boydston, N. (1999) Thermally-Actuated Cantilever Beam for Achieving Large In-Plane Mechanical Deflections. *Thin Solid Films*, v 355-356, p 295-302.

Lakdawala, H. & Kim, E.S. (1998). Simple Post-Processing Technique to Tune Resonant Frequency of Film Bulk Acoustic Resonators and Stacked Crystal Filters. *IEEE International Frequency Control Symposium, 1998, Pasadena, CA:* IEEE.

Lee, K.B., Lin, L., and Cho, Y-H. (2004). A Frequency-Tunable Microactuator with a Varied Comb-Width Profile. *17th IEEE International Conference on Micro Electro Mechanical Systems (MEMS), 2004, Maastricht, Netherlands.* Institute of Electrical and Electronics Engineers Inc.

Lee, K.B. & Cho, Y-H. (1996). Electrostatic Control of Mechanical Quality Factors for Surface-Micromachined Lateral Resonators. *Journal of Micromechanics and Microengineering*, v 6 (4), p 426-30.

Lee, S.S. & White, R.M. (1995). Self-Excited Piezoelectric Cantilever Oscillators. *The 8th International Conference on Solid-State Sensors and Actuators, and Eurosensors IX, 1995, Stockholm, Sweden*: Elsevier Science S.A.

Marshall, B. (2006). *How the Radio Spectrum Works.* Retrieved April 20, 2006, from http://electronics.howstuffworks.com/radio-spectrum1.htm.

MEMS and Nanotechnology Clearinghouse. (2006). *Materials Database*. Retrieved April 26, 2006, from http://www.memsnet.org/material/.

Moser, D., Brand, O. & Baltes, H. (1991). A CMOS Compatible Thermally Excited Silicon Oxide Beam Resonator with Aluminum Mirror. *1991 International Conference on Solid-State Sensors and Actuators, 1991, San Francisco, CA.*: IEEE.

Murata Manufacturing Co. (2006) *Ceramic Resonators*. Retrieved April 20, 2006, from http://www.murata.com/ceralock/base03.html.

Muriuki, M. (2004). *An Investigation into the Design and Control of Tunable Resonators*. thesis, University of Pittsburgh, Pittsburgh, PA.

Nguyen, C. T.-C. (2004). Vibrating RF MEMS for Next Generation Wireless Applications. *IEEE Custom Integrated Circuits Conference, 2004, Orlando, FL.* Piscataway, NJ: IEEE.

Norton, M. & Karczub. (1989). *Fundamentals of Noise and Vibration Analysis for Engineers*. Cambridge, United Kingdom: University Press.

Pang, W., Yu, H., Zhang, H., & Kim, E.S. (2005) Temperature Compensated Film Bulk Acoustic Resonator Above 2 GHz, *IEEE Device Letters,* v 26 (6), p 369-371.

Park, J.Y., Lee, H.C., Lee, K.H., Lee, H.M., & Ko, Y.J. (2003). Micromachined FBAR RF Filters for Advanced Handset Applications. *12th International Conference on Solid State Sensors, Actuators and Microsystems, 2003, Boston, MA.* Piscataway, NJ: IEEE.

Piezo Systems Inc. (2006) *History of Piezoelectricity*. Retrieved April 20, 2006, from http://www.piezo.com/tech4history.html.

Remtema, T. & Lin, L. (2001). Active Frequency Tuning for Micro Resonators by Localized Thermal Stressing Effects. *Sensors and Actuators,* v v A91 (3), p 326-32.

Ristic, L. (Ed.). (1994). *Sensor Technology and Devices*. Norwood, MA: Artech House.

Rouvaen, J.M., Ait-Ahsene, M., Menhaj-Rivenq, A., Logette, P. & Goutin, P. (2002). Generation of Surface Acoustic Waves in Non-Piezoelectric Solids Using Edge Bonded Rotated Y-cut Lithium Niobate Transducers. Journal of Applied Physics D: Applied Physics, v 35 (4), p 378-85.

Royer, D. & Dieulesaint, E. (2000). *Elastic Waves in Solids*. New York: Springer.

Ruby, R. & Merchant, P. (1994). Micromachined Thin Film Bulk Acoustic Resonators, *IEEE International Frequency Control Symposium, 1994, Boston, MA.* New York, NY, USA: IEEE.

Sakata, M., Wakabayashi, S., Goto, H., Totani, H., Takeuchi, M., and Yada, T. (1996). Sputtered High d31 Coefficient PZT Thin Film For Micro Actuators. *Proceedings of 9th International Workshop on Micro Electromechanical Systems, 1996, San Diego, CA.* New York, NY, USA: IEEE.

Salgar, S., Kim, G., Han, D-H, & Kim, B. (2002). Modeling and Simulation of the Thin-Film Bulk Acoustic Resonator. *IEEE International Frequency Control Symposium and PDA Exhibition, 2002, New Orleans, LA*: IEEE

Selvakumar, A., Najafi, K., Juan, W.H, & Pang, S. (1995). Vertical Comb Array Microactuators. *Proceedings of the IEEE Micro Electro Mechanical Systems (MEMS), 1995, Amsterdam, Neth.:* IEEE

Senturia, S.D. (2001). *Microsystem Design*. USA: Kluwer Academic Publishers.

Soderkvist, J. & Hjort, K. (1994). The Piezoelectric Effect of GaAs used for Resonators and Resonant Sensors. *Journal of Micromechanics and Microengineering,* v 4 (1), p 28-34.

Sreenivas, K., Sayer, M., & Garrett, P. (1989). Properties of DC-Magnetron Sputtered Lead Zirconate Titanate Films. *Thin Solid Films*, v 172, p 251-67.

Su, Q-X, Kirby, P., Komuro, E., Imura, M., Zhang, Q., and Whatmore, R. (2001) Thin-Film Bulk Acoustic Resonators and Filters Using ZnO and Lead-Zirconium-Titanate Thin Films. *IEEE Transactions on Microwave Theory and Techniques*, v 49 (4), 769-78.

Sze, S.M. (Ed.). (1994). *Semiconductor Sensors*. New York: John Wiley & Songs, Inc.

Tang, W.C., Nguyen, T.H., Judy, M.W., & Howe, R.T. (1990). Electrostatic-Comb Drive of Lateral Polysilicon Resonators. *Sensors and Actuators (Physical)*, v A21 (n 1-3), p 328-31.

Tang, W.C., Nguyen, T.-C.H., & Howe, R.T. (1989). Laterally Driven Polysilicon Resonant Microstructures, *Sensors and Actuators*, v 20 (1-2), p 25-32.

Trolier-McKinstry, S. & Muralt, P. (2004). Thin Film Piezoelectric for MEMS. *Journal of Electroceramics,* v 12 (1-2), p 7-17.

Velu, G., Remiens, D., Tronc, P., Cattan, E. & Thierry, B. (1996). Influence of Annealing Treatment on the Ferroelectric and Piezoelectric Properties of PZT Thin Films Grown on Silicon Substrates by Sputtering. *Proceedings of the Tenth IEEE International Symposium on Applications of Ferroelectrics, 1996, East Brunswich, NJ.* New York, NY, USA: IEEE.

Wang, K., Wong, A-C., Hsu, W-T, & Nguyen, C. T.-C. (1997). Frequency Trimming and Q-Factor Enhancement of Micromechanical Resonators Via Localized Filament Annealing, *International Conference on Solid-State Sensors and Actuators, 1997, Chicago, IL.* New York, NY, USA: IEEE.

Xie, H. & Fedder, G.K. (2002). Vertical Comb-Finger Capacitive Actuation and Sensing for CMOS-MEMS. *Sensors and Actuators A: Physical*, v 95 (2-3), p. 212-221.

Xie, Y., Li, S-S, Lin, Y-W, Ren, Z., & Nguyen, C.T-C. (2003) UHF Micromechanical Extensional Wine-Glass Mode Ring Resonators. IEEE International Electron Devices Meeting, 2003, Washington, D.C: Institute of Electrical and Electronics Engineers Inc.

Yu, H., Pang, W., Zhang, H., & Kim, E.S. (2005) Film Bulk Acoustic Resonator At 4.4 GHz with Ultra Low Temperature Coefficient of Resonant Frequency. *18th IEEE International Conference on Micro Electro Mechanical Systems, 2005, Miami Beach, FL.* Piscataway, NJ: IEEE.

Zhang, Q.Q., Gross, S.J., Tadigadapa, S., Jackson, T.N., Diuth, F.T., and Trolier-McKinstry, S. (2003). Lead Zirconate Titanate Films for d33 Mode Cantilever Actuators. *Sensors and Actuators A: Physical*, v 105 (1), p 91-7.

Zhang, Y., Wang, Z. & Cheeke, J.D.N. (2003). Resonant Spectrum Method to Characterize Piezoelectric Films in Composite Resonators. *IEEE Transactions on Ultrasonics, Ferroelectics, and Frequency Control*, v 50 (3), p 321-33.